

Measurement of the spin structure function g_1^d of the deuteron and its moments at low Q^2

Krishna P. ADHIKARI¹, Sebastian E. KUHN, Gail E. DODGE

Old Dominion University, Norfolk, Virginia 23529, USA

Alexander DEUR

Thomas Jefferson National Accelerator Facility, Newport News

Virginia 23606, USA

Lamiaa EL FASSI

Mississippi State University, Mississippi State,

Mississippi 39762, USA

Hyekoo KANG

Seoul National University, Seoul, Korea

Marco RIPANI, Raffaella DE VITA

INFN, Sezione di Genova, I-16146 Genova, Italy

Karl SLIFER, Elena LONG, Sarah K. PHILLIPS

University of New Hampshire, Durham, New Hampshire 03824, USA

Xiaochao ZHENG

University of Virginia, Charlottesville, Virginia 22901, USA

March 21, 2017

¹Current address: *Mississippi State University, Mississippi State, Mississippi 39762*

Contents

1	Introduction	4
1.1	Inclusive Electron Scattering	6
1.1.1	Kinematic Variables	6
1.1.2	Differential Cross Section and Structure Functions	8
1.2	Moments of g_1 and Sum Rules	9
1.2.1	First moment Γ_1 of g_1	10
1.2.2	Generalized GDH Integral	11
1.2.3	Generalized Forward Spin Polarizability γ_0	13
2	EG4 run	15
2.1	New CC in the 6 th Sector	17
3	Data Analysis Procedure	21
3.1	Raw Data Processing - Calibration and Reconstruction	22
3.2	Helicity States	23
3.3	Electron Identification	24
3.3.1	Electromagnetic Calorimeter Cuts	25
3.3.2	Cerenkov Counter Cuts	32
3.3.3	Minimum/Maximum Momentum cuts	38
3.3.4	Vertex-Z cuts	39
3.3.5	Fiducial Cuts	41
3.4	Data Quality and Stability Checks	48
3.5	Kinematic Corrections	51
3.5.1	Incoming Energy Loss Correction	51
3.5.2	Tracking Corrections	52
3.5.3	Momentum Correction	58
3.5.4	Outgoing Ionization Loss Correction	61
3.6	Cerenkov Counter (CC) Efficiency	62
3.6.1	Procedure	64
3.7	Pion Contamination Corrections	68

3.7.1	Method	68
3.8	e^+e^- -Pair Symmetric Contamination Corrections	70
3.9	Study of NH_3 Contamination of EG4 ND_3 Target	72
3.9.1	Procedure	72
3.9.2	Event Selection	73
3.9.3	Extracting the Contamination	75
3.9.4	Results and Conclusion	76
4	Monte Carlo Simulations and Extraction of g_1 and $A_1 F_1$	78
4.1	Simulation and Approach to Analysis	78
4.1.1	Outline of the method	81
4.2	Radiative Corrections	82
4.3	“Standard” simulation	82
4.3.1	RCSLACPOL	83
4.3.2	Event Generator	83
4.3.3	GSIM - CLAS Detector Simulation	84
4.3.4	GSIM POST PROCESSOR (GPP)	86
4.4	Comparison of Data and Simulation	88
4.5	Method to Extract g_1 and $A_1 F_1$	97
4.5.1	‘Variation’ of the standard simulation	97
5	Systematic Uncertainties	102
5.1	Evaluation of Experimental Systematics	103
5.2	Model uncertainties	105
5.3	Combining uncertainties	106
5.3.1	Combining data from the two beam energies	107
6	Results	118
6.1	Extracted g_1 and $A_1 F_1$	118
6.2	Moments of Deuteron Spin Structure functions	127
6.2.1	First moment of g_1 (Γ_1)	129
6.2.2	The extended GDH integral \bar{I}_{TT}	131
6.2.3	The Generalized Forward Spin Polarizability γ_0	133
7	Conclusions	136
A	FFREAD cards used by GSIM	142

¹ Chapter 1

² Introduction

³

⁴ A large amount of data on the spin dependent structure of the nucleon has been
⁵ accumulated since the late 1970s from both fixed target and colliding beam exper-
⁶ iments with polarized photons, (anti)electrons, and muons as well as protons on a
⁷ variety of polarized targets from hydrogen through 3He .

⁸ In a simple non-relativistic model one would expect the quarks to carry the entire
⁹ spin of the nucleon, but one of the first experiments carried out at SLAC, in a lim-
¹⁰ ited kinematic region, seemed to confirm the predictions of the Naive Parton Model
¹¹ (NPM) - one of the early more realistic theories - which predicted that 60% of the
¹² nucleon spin is carried by the quarks [1]. However, a subsequent, more precise mea-
¹³ surement over a larger kinematic region performed by the EMC experiment at CERN
¹⁴ reported, contrary to the NPM predictions, that only $12 \pm 17\%$ of the spin is carried
¹⁵ by the quarks [2]. This discovery of the so-called “spin crisis” sparked a large inter-
¹⁶ est in measuring the spin content of the nucleon, giving birth to several experiments
¹⁷ (completed, underway and proposed) around the globe. The theoretical developments
¹⁸ of Quantum Chromodynamics (QCD) - the quantum field theory that describes the
¹⁹ nuclear interaction between the quarks and gluons - have clarified our picture of the
²⁰ nucleon spin structure in great details. With the discovery of a unique QCD prop-
²¹ erty known as “asymptotic freedom”, quarks are known to be essentially free at high
²² energies (typically several GeV) allowing perturbative QCD (PQCD) calculations of
²³ testable predictions for processes involving high energy or high momentum transfers
²⁴ [3]. Verifying Bjorken sum rule [4], which relates results from inclusive, polarized deep
²⁵ inelastic scattering (DIS) to the axial coupling constant g_A of neutron beta decay, is
²⁶ a precise test of QCD in its spin sector. The DIS results have verified the Bjorken
²⁷ sum rule at the level of 10% accuracy and has shown that only about $30 \pm 10\%$ of the
²⁸ nucleon spin is carried by the quarks; the rest of the spin must reside either in gluons
²⁹ or orbital angular momentum of its constituents. Experiments to measure the gluon

contribution are underway at Brookhaven National Laboratory (BNL) and CERN.
Probing nucleon structure on the other end of the energy scale (i.e. probing with low momentum transfers) provides information about long distance structure, which is also associated with static properties of the nucleon. In this low energy regime, however, QCD calculations with the established perturbative methods become difficult or even impossible because the strong coupling (α_s) becomes large. Thus perturbative expansions do not converge. In this energy regime, the partons become very strongly coupled to the point of being confined into hadrons which now emerge as the effective degrees of freedom for the interaction. Therefore, other methods must be relied on to make predictions in these non-perturbative energy scales. For example, effective theories such as chiral perturbation theory (χ PT) are used. There is also an intermediate region where neither of these approaches (PQCD or χ PT) is expected to work. In this region, it is expected that lattice QCD methods will provide testable predictions in the near future. There are also some phenomenological models aimed at describing the entire kinematic range. The description of the low energy regime in terms of these theories and models is challenging and theories used here still face difficulties (see below). There are several predictions (for both nucleons as well as some light nuclei such as the deuteron and Helium-3) from these low energy theories and models on various observables which can be tested experimentally. Therefore, having high precision data at the lowest possible momentum transfer is necessary to test these predictions. In addition, new results will also help constrain future calculations and provide input for detailed corrections to higher energy data.

With that perspective and motivation, the “EG4” experiment (E06-017) for a precision double polarization measurement at low momentum transfer using both proton and deuteron targets and the Hall B CLAS detector was performed at Jefferson Lab. In addition to the usefulness of the measured deuteron data for testing theoretical predictions calculated for the deuteron itself, the data are also necessary for extracting neutron data in combination with similar data from the proton target. An experiment with the similar goal of probing the neutron at low momentum transfers but using ^3He was performed in Hall A [5]. However, to be able to control nuclear medium effects, neutron information must be extracted from both ^3He and ^2D . The data on the deuteron (and eventually on the neutron) will not only be useful to test the theoretical predictions at low but non-zero momentum transfers but they can also be extrapolated to the real photon limit, thus testing some long standing predictions such as the Gerasimov-Drell-Hearn (GDH) sum rule [6, 7] derived from general principles. The analysis of the deuteron data is the subject of this note.

In the future, we will extract information from the deuteron and proton data from the EG4 experiment to provide a self-consistent determination of the Bjorken sum, helping us to understand the transition from the partonic to hadronic descriptions of the strong interaction. The data will also be useful in studying the validity of quark-

⁷⁰ hadron duality in the spin sector, thus helping further to understand the transition
⁷¹ from the partonic to hadronic pictures.

⁷² 1.1 Inclusive Electron Scattering

⁷³ High energy particle scattering processes provide very powerful microscopes to ex-
⁷⁴ amine objects such as nuclei and nucleons. Scattering of leptons (most commonly
⁷⁵ electrons) is one of the most extensively used processes. For example, the scattering
⁷⁶ of high energy leptons off nucleons has played a key role in determining the partonic
⁷⁷ structure of the nucleons. Following are some of the advantages of lepton (and in
⁷⁸ particular electron) scattering:

- ⁷⁹ • Leptons interact through the electroweak interaction which is very well under-
⁸⁰ stood.
- ⁸¹ • The interaction is relatively weak, thus allowing the use of perturbative QED.
- ⁸² • In electron scattering, one can, moreover, control and vary the polarization of
⁸³ the virtual photon (exchanged during the interaction) by changing the electron
⁸⁴ kinematics. This allows the separation of the charge and current interaction.
⁸⁵ Data from the scattering of polarized electrons by polarized targets allows one
⁸⁶ to examine the target's strong-interaction spin structure.
- ⁸⁷ • A great advantage of electrons is that they can be copiously produced in the
⁸⁸ laboratory relatively easily and at low costs, and since they are charged, they
⁸⁹ can readily be accelerated and detected. (It is not as easy and cheap to produce
⁹⁰ and handle the other lepton types.

⁹¹ In this section, we discuss the process of inclusive electron scattering (in which
⁹² only the scattered electron is detected ignoring the rest of the components of the final
⁹³ state after the interaction). In doing so, the relevant kinematic variables and related
⁹⁴ physical quantities to be measured or calculated from the process will be introduced
⁹⁵ and some of their relations with one another will be deduced and discussed.

⁹⁶ 1.1.1 Kinematic Variables

⁹⁷ A lepton scattering process, in which an incoming lepton represented by $l(p)$ of four
⁹⁸ momentum $p = p^\mu = (E, \vec{k})$ scatters off a target $N(P)$ which is usually a nucleon or a
⁹⁹ nucleus at rest and with four momentum $P = P^\mu = (M, \vec{0})$, can simply be represented
¹⁰⁰ by

$$l(p) + N(P) \rightarrow l(p') + X(P') \quad (1.1)$$

101 where $l(p')$ and $X(P')$ represent the scattered lepton and the rest of the final state
 102 (which can have any number of particles) with four momenta $p'^\mu = (E', \vec{k}')$ and $P'^\mu =$
 103 (E_X, \vec{k}_X) respectively. The scattering angle which is the angle between the incident
 104 and outgoing path/direction of the electron is denoted by θ . The final (hadronic)
 105 state denoted by x is not measured, with only the scattered electron detected and
 106 measured by the detector(s). In the first order (Born) approximation of the process,
 107 a virtual photon is exchanged (as depicted in Fig (1.1)) whose four momentum is
 108 equal to the difference between that of the incident and the scattered electron and
 109 is given by $(p - p')^\mu = (\nu, \vec{q})$, where $\nu = (P \cdot q)/M$ and \vec{q} represent the energy and
 110 3-momentum transferred by the incident electron to the target $N(P)$.

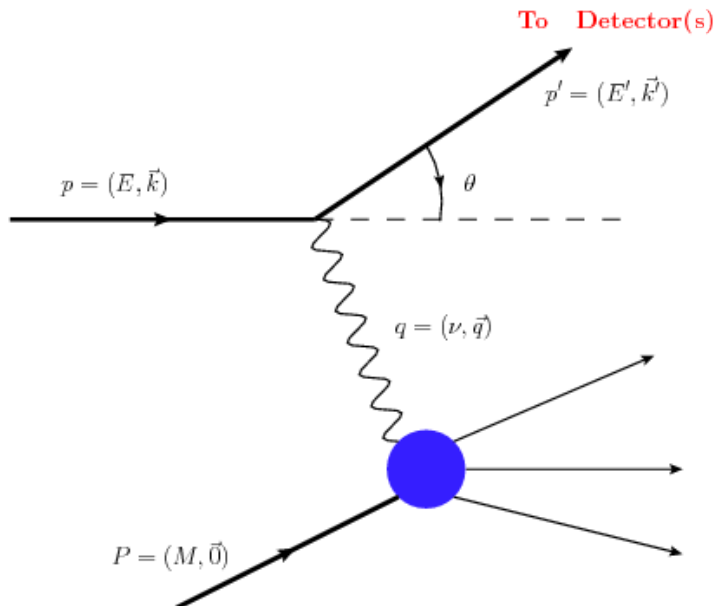


FIG. 1.1. Lowest order (Born approximation) Feynmann diagram representing the process of inclusive lepton scattering

111 The kinematics of the scattering process, for a given beam energy E , can be

¹¹² completely described in terms of two of the following Lorentz invariant variables.

$$\nu = E - E' \quad (1.2)$$

$$Q^2 = -q^2 \simeq 4EE' \sin^2 \frac{\theta}{2} \quad (1.3)$$

$$W = \sqrt{(P+q)^2} = \sqrt{M^2 + 2M\nu - Q^2} \quad (1.4)$$

$$x = \frac{Q^2}{2P \cdot q} = \frac{Q^2}{2M\nu} \quad (1.5)$$

$$y = \frac{q \cdot P}{p \cdot P} = \frac{\nu}{E} \quad (1.6)$$

¹¹³ where $Q^2 = -q^2$ is the negative of the squared four-momentum transferred (with
¹¹⁴ electron mass neglected in the expression for Q^2), which defines the resolution of
¹¹⁵ the electron probe; W is the invariant mass of the unmeasured final state (x); x is
¹¹⁶ known as the Bjorken scaling variable, which is also interpreted as the momentum
¹¹⁷ fraction carried by the struck quark (parton) in the infinite momentum frame; M is
¹¹⁸ the nucleon mass ≈ 0.939 GeV, and lastly, y is the fraction of the energy that is lost
¹¹⁹ by the lepton during the process.

¹²⁰ 1.1.2 Differential Cross Section and Structure Functions

¹²¹ The differential cross section for the process of inclusive (polarized) electron scattering
¹²² on (polarized) targets can be expressed, in the Born approximation, in terms of
¹²³ four dimensionless structure functions $F_1(x, Q^2)$, $F_2(x, Q^2)$, $g_1(x, Q^2)$, and $g_2(x, Q^2)$,
¹²⁴ effectively parameterizing the internal hadronic structure information into four re-
¹²⁵ sponse functions. For example, in the case of the anti-parallel or parallel beam and
¹²⁶ target polarizations, the spin-dependent (polarized) inclusive cross sections can be
¹²⁷ expressed as follows:

$$\frac{d^2\sigma}{d\Omega dE'} = \left(\frac{d\sigma}{d\Omega} \right)_{Point} \left[\frac{2}{M} F_1(x, Q^2) \tan^2 \frac{\theta}{2} + \frac{1}{\nu} F_2(x, Q^2) \right. \\ \left. \pm 2 \tan^2 \frac{\theta}{2} \left[(E + E' \cos \theta) \frac{M^2}{\nu} g_1(Q^2, \nu) - \gamma^2 M^2 g_2(Q^2, \nu) \right] \right]^{(1.7)}$$

¹²⁸ where “+” refers to anti-parallel beam helicity and target polarization, while “-”
¹²⁹ refers to the parallel case. And the Point cross section (for the lepton scattering from
¹³⁰ a Dirac particle - a spin-1/2 point particle of charge +e) given by

$$\left(\frac{d\sigma}{d\Omega} \right)_{Point} = \frac{\alpha^2 \cos^2 \frac{\theta}{2}}{4E^2 \sin^4 \frac{\theta}{2}} \frac{E'}{E} \quad (1.8)$$

131 with $\frac{E'}{E}$ being the recoil factor.

132 These kind of relationships allow the measurement of structure functions by mea-
133 suring cross-sections corresponding to different combinations of beam and target po-
134 larizations. For example, one can extract the first two structure functions F_1 and F_2
135 from the unpolarized scattering experiments, whereas, the spin structure functions
136 g_1 and g_2 can be measured in experiments with polarized electron beam and polarized
137 targets and by measuring the cross section difference between the anti-parallel and
138 parallel beam-target polarizations.

139 1.2 Moments of g_1 and Sum Rules

140 Moments of structure functions are their integrals (over the complete x range) weighted
141 by various powers of the variable x. The n^{th} moment of g_1 , for example, is given by

$$\Gamma_n(Q^2) = \int_0^1 g_1(x, Q^2) x^{(n-1)} dx \quad (1.9)$$

142 The moments allow the studies of the (Q^2 dependence of) fundamental properties
143 of nucleon structure. For example, the first moment of xF_1 of a nucleon gives the
144 total momentum or mass fraction carried by quarks and the first moment of g_1 gives
145 the fraction of the nucleon spin contributed by the quark helicities. These integrals
146 get their particular significance from the fact that they can be predicted from rigorous
147 theoretical methods, such as in the sum rules derived from general assumptions or
148 from the method of Operator Product Expansion, lattice QCD calculations and χ PT
149 calculations¹. Their importance can be highlighted from the fact that it was the
150 experimental tests of the sum rules involving the first moments of nucleon that led
151 to the discovery of the original “spin crisis” and provided a significant test of QCD
152 in the spin sector [8].

153 In this section, three integrals are considered which have been calculated from the
154 EG4 data on the deuteron - the first moment of g_1 (Γ_1), the generalized GDH integral
155 (\bar{I}_{TT}), and the generalized forward spin polarizability (γ_0).

¹In contrast, the same is not true about the structure functions because presently their complete description based on QCD first principles has not been possible yet (especially in the low to intermediate momentum transfer regions due to the strong coupling property of QCD).

₁₅₆ **1.2.1 First moment Γ_1 of g_1**

₁₅₇ The first moment of g_1 is the integral of g_1 over the complete range of the Bjorken
₁₅₈ scaling variable x .

$$\Gamma_1(Q^2) = \int_0^1 g_1(x, Q^2) dx \quad (1.10)$$

₁₅₉ This moment gives, in the quark-parton model, the fraction of the nucleon spin
₁₆₀ contributed by the quark helicities and enters directly into two historically important
₁₆₁ sum rules - Ellis-Jaffe sum rule and Bjorken sum rule. Measurements of the moment
₁₆₂ on the proton by the European Muon Collaboration (EMC) in 1988 showed that the
₁₆₃ Ellis-Jaffe sum rule is violated, which meant that the long held belief that all the
₁₆₄ proton spin is carried by quarks is not true, thus, sparking the well known “spin
₁₆₅ crisis”. On the other hand, measurements from SLAC, CERN, Fermilab, DESY, and
₁₆₆ more recently, from JLab, have confirmed the Bjorken sum rule (which relates the
₁₆₇ difference of the first moments of the proton and the neutron to the fundamental
₁₆₈ axial coupling constant (g_A) of neutron beta decay) at the level of 10% accuracy,
₁₆₉ thus helping establish the QCD as the correct theory of the strong interactions. The
₁₇₀ moment also enters into the virtual photon extension of another famous sum rule -
₁₇₁ the GDH sum rule (see below).

₁₇₂ In addition, the moment is studied on its own right because it provides a powerful
₁₇₃ tool to test the validity of various theories and models in which it is calculable. In the
₁₇₄ past, it has been measured on proton, deuteron and neutron (${}^3\text{He}$) at SLAC, CERN
₁₇₅ and DESY in the DIS region in order to understand the quark spin contribution
₁₇₆ as well as to test the validity of the Bjorken sum rule and hence QCD as a result
₁₇₇ [8]. Recently, it has also been measured at JLab from DIS down to a fairly low Q^2
₁₇₈ region. In the intermediate and low momentum transfers, some phenomenological
₁₇₉ model predictions are available, whereas in the very low Q^2 region, several chiral
₁₈₀ perturbation theory (χPT) calculations are available.

181 **1.2.2 Generalized GDH Integral**

182 **GDH Sum Rule**

183 The Gerasimov-Drell-Hearn (GDH) sum rule [6, 7] relates the energy weighted sum
184 of a particle’s photo-absorption cross sections to its anomalous magnetic moment κ .
185 For a target of arbitrary spin S , the sum rule is:

$$\int_{\nu_{th}}^{\infty} \frac{\sigma_P(\nu) - \sigma_A(\nu)}{\nu} = -4\pi^2 \alpha S \left(\frac{\kappa}{M} \right)^2 \quad (1.11)$$

186 where σ_P and σ_A are the photoabsorption cross sections with photon helicity parallel
187 and anti-parallel to the target spin respectively. M and κ represent the target mass
188 and anomalous magnetic moment respectively and S represents the target spin. The
189 integration extends from the onset ν_{th} of the inelastic region ² through the entire
190 kinematic range and is weighted by the inverse of the photon energy ν .

191 The sum rule for the proton has been measured (at various places such as Mainz,
192 Bonn, BNL and others) and verified to within 10% [9–12] and some deuteron results
193 exist from Mainz and Bonn, but there is very little or no data available on neutron
194 and other targets;

195 **Implications of the sum rule** The sum rule relates the static property κ of a
196 particle’s ground state with the sum of the dynamic properties of all the excited
197 states. One deeper significance of this sum rule is that if a particle has a non-
198 zero anomalous magnetic moment, then it must have some internal structure, and,
199 therefore, a finite size and the excited states (a point-like particle cannot have excited
200 states). Because of the same reason, the discovery of nucleon anomalous magnetic
201 moments provided one of the first strong indications that the nucleons had some
202 intrinsic internal structure.

203 In addition to the benefit of that implication, the sum rule and its extension to
204 $Q^2 > 0$ provides an important testing ground for various theoretical predictions based
205 on QCD and its effective theories/models.

206 **Generalization of the GDH Sum (Rule)**

207 In order to investigate the “spin crisis” of the 1980’s, Anselmino *et al.* [13] proposed
208 that the real photon ($Q^2=0$) GDH integral could be extended to electroproduction
209 cross sections (finite Q^2) and that the experimental determination of the extended

²The pion photo-production threshold given by $\nu_{th} = m_\pi(1 + m_\pi/2M) \approx 150\text{MeV}$ marks the onset of the inelastic region for the nucleons, but for nuclei, the summation starts from the first nuclear excitation level

integral would shed light on the transition from the perturbative to non-perturbative QCD. The idea was to use the virtual photoabsorption cross sections in place of the real photoabsorption cross sections and proceed in exactly the same way as when deriving the real photon GDH sum rule. This extension depends somewhat on the choice of the virtual photon flux and on how the spin structure function g_2 is considered [14]. In one extension the virtual photon flux given by $K = \nu$ is chosen and the real photoabsorption cross section difference in Eq. 1.11 are replaced by the corresponding virtual photoabsorption cross section difference $2\sigma_{TT}$. As a result, we get the following extended GDH integral (considering only the inelastic contribution starting from the pion production threshold) [8]

$$\bar{I}_{TT} = \frac{2M^2}{Q^2} \int_0^{x_0(Q^2)} dx [g_1(x, Q^2) - \frac{4M^2 x^2}{Q^2} g_2(x, Q^2)] \quad (1.12)$$

where $x_0(Q^2) = Q^2/(Q^2 + m_\pi(2M + m_\pi))$ is the pion production threshold that defines the onset of the inelastic region.

The integral can also be expressed in terms of the first moment of the product $A_1 F_1$ as follows:

$$\bar{I}_{TT} = \frac{2M^2}{Q^2} \int_0^{x_0(Q^2)} dx A_1(x, Q^2) F_1(x, Q^2) \quad (1.13)$$

where A_1 is the virtual photon asymmetry as given by:

$$A_1(x, Q^2) = \frac{\sigma_{\frac{1}{2}}^T - \sigma_{\frac{3}{2}}^T}{\sigma_{\frac{1}{2}}^T + \sigma_{\frac{3}{2}}^T} = \frac{g_1(x, Q^2) - \gamma^2 g_2(x, Q^2)}{F_1(x, Q^2)} \quad (1.14)$$

$$(1.15)$$

225 1.2.3 Generalized Forward Spin Polarizability γ_0

226 Polarizabilities are fundamental observables (quantities) that characterize the struc-
 227 ture of composite objects such as nucleons or deuteron. They reflect the response to
 228 external perturbations such as external electromagnetic fields. Like the GDH sum,
 229 they are also integrals over the excitation spectrum of the target and their derivations
 230 rely on the same basic assumptions. At the real photon point, for example, the elec-
 231 tric and magnetic polarizabilities α and β represent the target's response to external
 232 electric and magnetic fields respectively. The generalized polarizabilities represent
 233 the extensions of these quantities to the case of virtual photon Compton scattering.
 234 Because the integrals defining the polarizabilities involve weighting by some powers of
 235 $1/\nu$ or x , they converge faster than the first moments and thus are more easily deter-
 236 mined from low energy measurements. In other words, they have reduced dependence
 237 on the extrapolations to the unmeasured regions at large ν , and higher sensitivity to
 238 the low energy behavior of the cross sections (particularly the threshold behavior),
 239 thus providing better testing grounds for theoretical predictions such as from χ PT
 240 and phenomenological models [14].

241 The GDH sum rule comes from the first term of the low energy expansion of the
 242 forward Compton amplitude [15]. Likewise, we get another sum rule from the second,
 243 i.e., the next-to-leading term (which is in the third power of ν). The second coefficient
 244 of the expansion is known as the forward spin polarizability γ_0 and by comparing the
 245 coefficients of the ν^2 terms on both sides (coming from the dispersion relations on the
 246 left side and from the low energy expansion on the right side) gives us the following
 247 expression for the polarizability [16]:

$$248 \quad \gamma_0 = -\frac{1}{4\pi^2} \int_{thr}^{\infty} \frac{\sigma_{\frac{1}{2}} - \sigma_{\frac{3}{2}}}{\nu^3} d\nu \quad (1.16)$$

249 Now, by considering the case of forward scattering of a virtual photon and using
 250 the same general approach as for getting the generalized GDH sum rule, the $\mathcal{O}(\nu^3)$
 251 (NLO) term in the low energy expansion of VVCS (doubly virtual Compton scat-
 252 tering) amplitude $g_{TT}(x, Q^2)$ gives the following generalization of the forward spin
 253 polarizability [17] [8]:

$$\gamma_0(Q^2) \equiv \gamma_{TT}(Q^2) = \frac{16\alpha M^2}{Q^6} \int_0^{x_0} \left[g_1(x, Q^2) - \frac{4M^2 x^2}{Q^2} g_2(x, Q^2) \right] x^2 dx \quad (1.17)$$

$$= \frac{16\alpha M^2}{Q^6} \int_0^{x_0} A_1(x, Q^2) F_1(x, Q^2) x^2 dx \quad (1.18)$$

253 where $\alpha = \frac{e^2}{4\pi}$ is the fine structure constant. At large Q^2 , the g_2 dependent term in
 254 the integrand becomes negligible and γ_0 reduces to the third moment of g_1 [17].

255 In exactly the same manner, from the $\mathcal{O}(\nu^2)$ term of the low energy expansion
 256 of the VVCS amplitude $g_{LT}(x, Q^2)$ one gets another polarizability - the generalized
 257 longitudinal-transverse polarizability as follows:

$$\delta_0(Q^2) \equiv \delta_{LT}(Q^2) = \frac{16\alpha M^2}{Q^6} \int_0^{x_0} [g_1(x, Q^2) + g_2(x, Q^2)] x^2 dx \quad (1.19)$$

258 This latter polarizability is not considered here because we did not measure the trans-
 259 verse target configuration.

260 Because the generalized polarizabilities can be expressed with the moments of the
 261 structure functions, it is possible to measure them using measurements of the struc-
 262 ture functions. As stated earlier, because of the weighting by some powers of ν or x ,
 263 these integrals converges more rapidly in energy than the GDH integral and therefore
 264 can more easily be determined by low beam energy measurements. These integrals are
 265 valuable because they shed light on the long distance (soft), non-perturbative aspects
 266 of the target structure. The integrals are possible to be calculated using effective or
 267 approximate theories such as χ PT and lattice methods. Thus the measurements of
 268 these quantities provide benchmark tests of such theories.

269 The first measurement of γ_0 for a proton target at the real photon point was done
 270 by the GDH experiment at Mainz [16]. Recently the JLab EG1b experiment has
 271 provided some finite Q^2 results for both deuteron as well as nucleon targets [18].

₂₇₂ **Chapter 2**

₂₇₃ **EG4 run**

₂₇₄ The deuteron target part of the EG4 experiment ran for about a month in 2006,
₂₇₅ mostly with longitudinally polarized frozen $^{15}\text{ND}_3$ as the target. In between these
₂₇₆ deuteron runs, some small amount of data was also collected on carbon-12 and empty
₂₇₇ cell targets, which are important in various auxiliary studies during the data analysis
₂₇₈ (such as their use in estimating nuclear background while developing momentum
₂₇₉ corrections, estimating the length of the target material or estimating unpolarized
₂₈₀ background). A total of 113 data runs (from run ID 51896 to 52040) were collected
₂₈₁ for the lower beam energy (1.3 GeV) and 221 runs (from 51593 to 51867) for the 2.0
₂₈₂ GeV case (with each run consisting of about 3.0×10^7 event triggers) [19]. Each run
₂₈₃ took about 2 hours and collected about 2 GB of data in raw format and saved as
₂₈₄ about 20-30 BOS files (see next section). With the combination of low beam energies
₂₈₅ and low scattering angles, low momentum transfers can be measured down to about
₂₈₆ 0.02 GeV² within the kinematic coverage of the resonance region ($1.08 < W < 2.0$
₂₈₇ GeV.)

₂₈₈ In addition to the use of low beam energies and low θ measurements, in order
₂₈₉ to maximize the statistics in the low momentum transfers, following measures were
₂₉₀ taken that were unique to the experiment:

- ₂₉₁ • Use of the electron outbending torus field configuration to enhance the low angle
₂₉₂ acceptance (so that more of very forward going electrons would be bent towards
₂₉₃ and detected by the CLAS detector).
- ₂₉₄ • Use of a a newly built Cerenkov Counter (CC) in the 6th sector¹ (see Figs. 2.4
₂₉₅ and 2.5) that was designed to optimize electron detection in the outbending
₂₉₆ torus configuration. This led to a better and more uniform detection efficiency

¹For reasons of limited resources, only one new CC was built and the 6th sector alone was used to detect the scattered electrons

297 would be better and more uniform than with the existing counters² which were
 298 optimized for electron inbending configuration.

- 299 • To further enhance the low angle coverage, the polarized target was placed in a
 300 more retracted position along the beam line i.e. at about -101.0 cm upstream
 301 of the CLAS center.

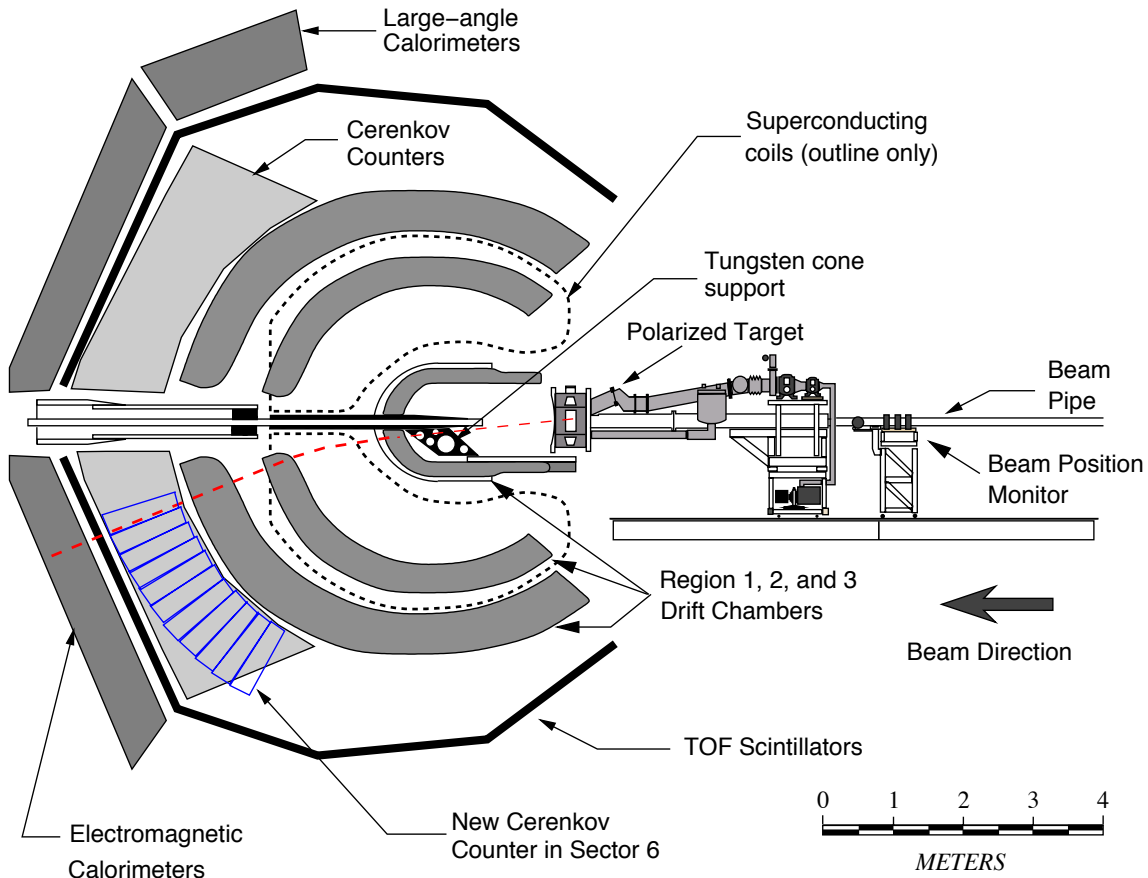


FIG. 2.1. The schematic diagram of the EG4 experimental setup showing the CLAS detector, polarized target system and some beam line elements.

302 Other than that the CLAS detector in the EG4 setup (see Fig. 2.1) was used
 303 in the standard configuration like in any other polarized target experiments using

²The standard CLAS Cherenkov detectors were designed such that their optics, geometry, module position and mirror orientation were optimized for low rate high Q^2 experiments that mostly use(d) electron in-bending torus fields. The design was a compromise between the desired kinematic coverage and the complexities of the CLAS detector system including the effect of the torus field.

304 CLAS. The following list summarizes various specifications of the experimental setup
305 (for more details see [20]):

- 306 • **Beam energies:** 1.3 and 2.0 GeVs for ND₃ target runs and 1.0, 1.3, 2.0, 2.3
307 and 3.0 GeVs for NH₃ target runs.
 - 308 – **Beam polarization:** Longitudinally polarized ($\approx 85\%$) electron beam
309 from CEBAF accelerator. Moeller scattering used for the polarization
310 measurement.
- 311 • **Polarized targets:** Solid ND₃, and NH₃ targets polarized using the technique
312 of Dynamic Nuclear Polarization (DNP).
 - 313 – **Average polarizations:** Between (75 - 90)% and (30 - 45)% respectively.
 - 314 – **Lengths:** 1cm for ND₃ and 1 cm and 0.5 cm for NH₃.
 - 315 – **Densities:** 1.056 and 0.917 respectively.
 - 316 – **Packing fractions:** (0.624, 0.764) for (1.3, 2.0) GeV ND₃ runs respec-
317 tively and (0.625, 0.624/0.717³, 0.716, 0.682, 0782) for (1.0, 1.3/1.3, 2.0,
318 2.3, 3.0) GeV NH₃ runs.
- 319 • **Other targets:** Carbon-12 (1 cm and 0.5 cm long), Empty target cup, Target
320 cup filled only with liquid helium (LHe), LHe bath and various foils due to
321 different target chamber windows.
- 322 • **Torus currents:** 1500 Amps for 1.0 and 1.3 GeV runs and 2250 A for 2.0,
323 2.3, and 3.0 GeV runs.

324 2.1 New CC in the 6th Sector

325 The Cherenkov Counters (CC) serve the dual function of triggering on electrons and
326 separating electrons from pions (or identifying charged particles). These detectors use
327 the light emitted by Cherenkov radiation (emission of light when the charged particle
328 travels faster than light in that medium) to measure the particle velocity (or rather
329 $\beta = v/c$). The knowledge of β combined with the particle momentum (from the
330 tracking detectors) determines the particle's mass, thus giving us information on the
331 particle identification. The index of refraction (n) is carefully optimized for the parti-
332 cle masses and momentum range of the experiments in question. Threshold counters

3The two numbers 0.624/0.717 for the 1.3 GeV NH₃ runs are due to the fact that two different NH₃ targets were used in case of 1.3 GeV runs. One target was in the top cell and the other was in the bottom cell of the target stick.

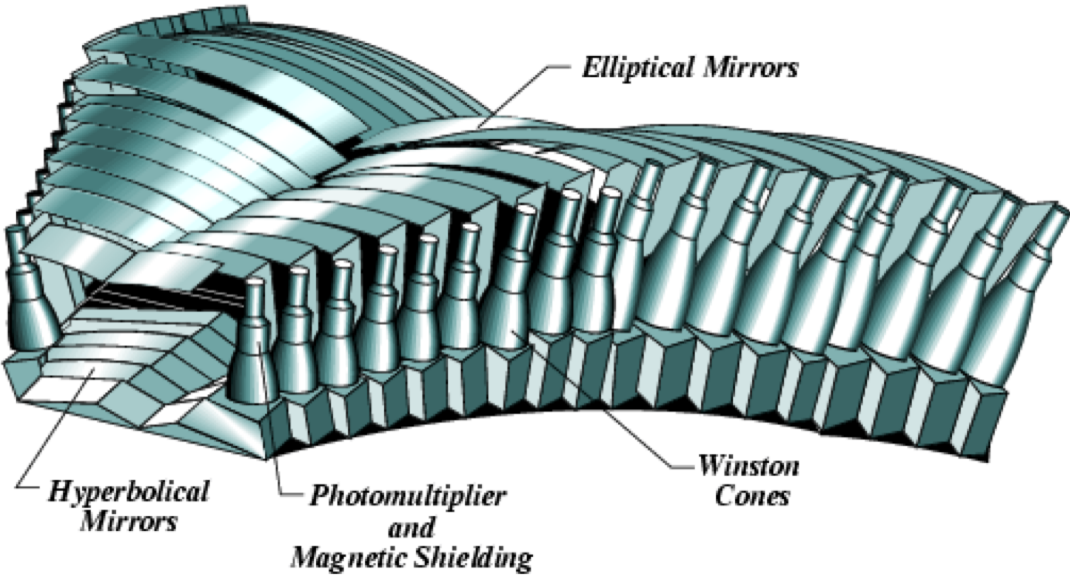


FIG. 2.2. The computer rendered image of the Standard CLAS Cherenkov Counter

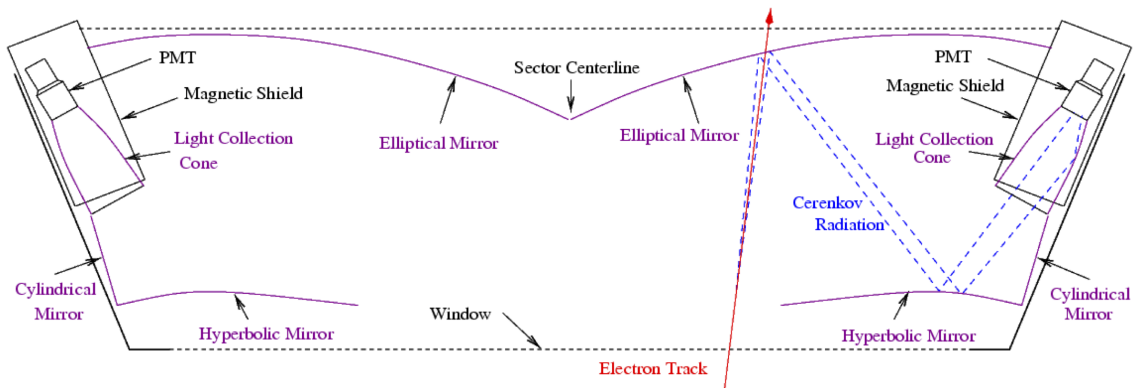


FIG. 2.3. The schematic diagram of a CLAS Cherenkov Counter (CC) module showing mirrors, PMTs and the light reflections.

333 record all light produced, thus providing a signal whenever β is above the threshold β_t
 334 = $1/n$. In the standard configuration, CLAS uses one Cherenkov threshold detector
 335 in each of the six sectors in the forward region from 8° to 45° .

336 A new gas threshold cherenkov counter (designed and built by INFN - Genova,
 337 Italy) was installed in the sixth sector. This new CC detector (see Fig. 2.4 for its
 338 CAD rendition) is specifically optimized for the out-bending field configuration, which

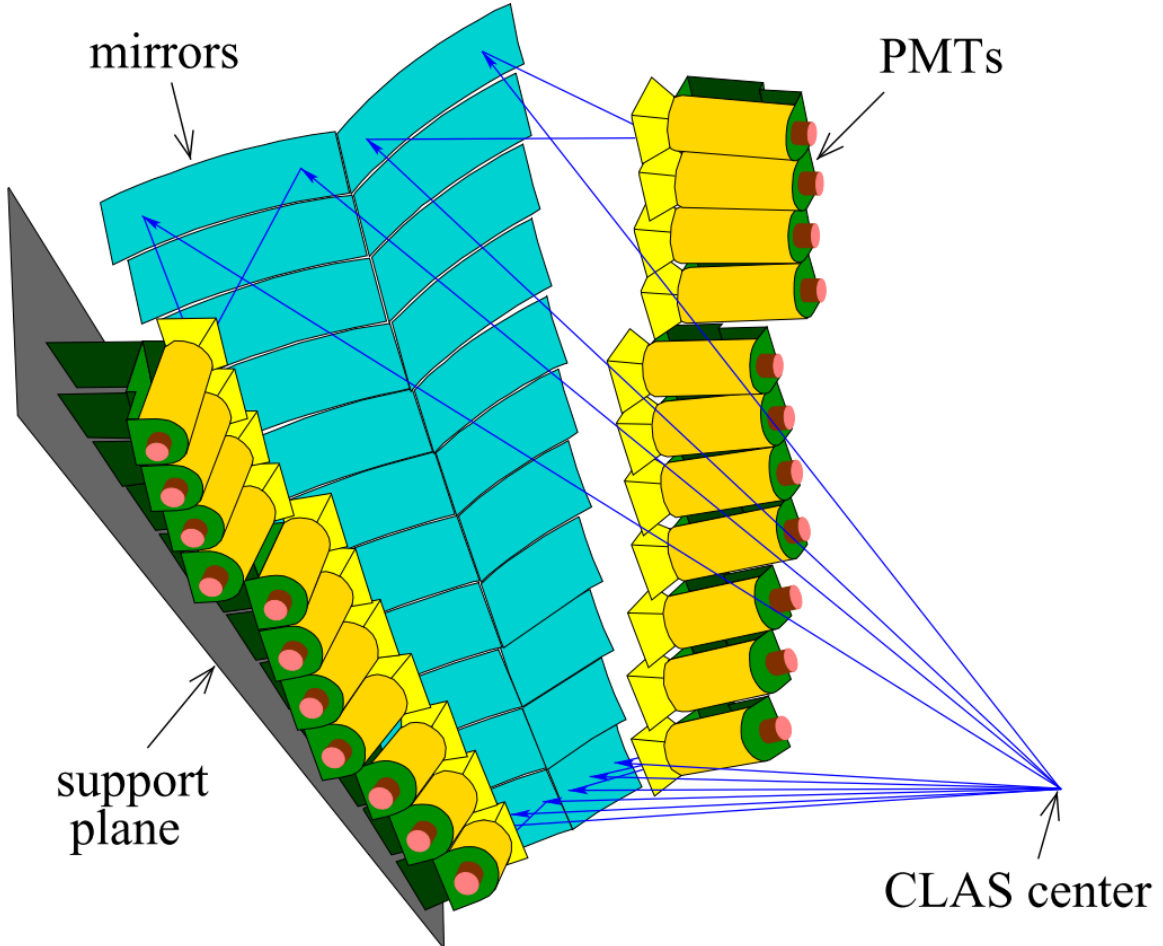


FIG. 2.4. The new Cherenkov counter designed and built by INFN, Genova. (Figure used from [21].)

is necessary to reach the desired low momentum transfer (measurements down to 6 degrees). The detector uses the same radiator gas (C_4F_{10} - perfluorobutane) and the same gas flow control system as the standard one, but it uses a different design. In the new CC, the number of CC-modules is now 11 instead of the 18 in the standard ones. In order to maximize the light collection, a single reflection design (see Fig. 2.5(b)) using spherical mirrors is used (the standard CC used double relections from elliptical and hyperbolic mirrors). The geometry, the size, the mirror size, position, and orientation, the dimensions as well as the assembly of the modules were optimized for the experiment and the performance study was done using a complete GEANT simulation [16]. Additionally, for the purpose of efficiency and performance studies (see Sec. 3.6), a few special trigger data runs were taken during the experiment. These

³⁵⁰ special runs had the trigger that mainly involved EC-signals (and no CC-signal at
³⁵¹ all) to decide whether the detected particle was a good scattered electron candidate.

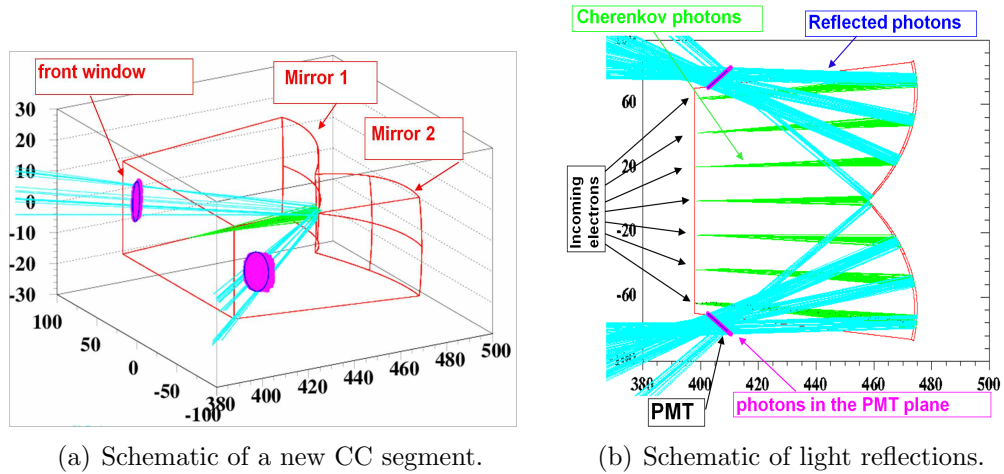


FIG. 2.5. Schematic of a new CC segment showing the arrangements of the mirrors, PMTs and the light reflections (courtesy of INFN, Genova).

³⁵² **Chapter 3**

³⁵³ **Data Analysis Procedure**

³⁵⁴ The goal of this data analysis is to extract the spin structure function g_1 for the
³⁵⁵ deuteron and evaluate its moments. Since the product A_1F_1 , which is proportional
³⁵⁶ to σ_{TT} , directly enters sum rules for the real photon point, which leads to the gener-
³⁵⁷ alized GDH integral (\bar{I}_{TT}) and the generalized forward spin polarizability (γ_0) being
³⁵⁸ expressed in terms of the first and third moments of the product A_1F_1 , we decided
³⁵⁹ also to extract the product A_1F_1 using exactly the same procedure as for g_1 .

³⁶⁰ The extraction of both g_1 and A_1F_1 depend directly on the measurement of the
³⁶¹ following polarized cross-section difference:

$$\Delta\sigma_{||} = \frac{d^2\sigma^{\downarrow\uparrow}}{d\Omega dE'} - \frac{d^2\sigma^{\uparrow\uparrow}}{d\Omega dE'} = \frac{1}{N_t} \cdot \left[\frac{N^+}{N_{e^-}^+} - \frac{N^-}{N_{e^-}^-} \right] \cdot \frac{1}{P_b P_t} \cdot \frac{1}{\Delta\Omega} \cdot \frac{1}{\eta_{detector}} \quad (3.1)$$

³⁶² where,

- ³⁶³ • N_t = Number density of deuteron nuclei in the target
- ³⁶⁴ • $N^{+/-}$: Number of scattered electrons (off deuteron only) for each helicity state
³⁶⁵ $(+/-)$.
- ³⁶⁶ • $N_{e^-}^{+/-}$: Number of incident electrons for $+/-$ helicity states
- ³⁶⁷ • $P_b P_t$ = Product of the beam and target polarizations
- ³⁶⁸ • $\Delta\Omega = \sin\theta \cdot \Delta\theta \cdot \Delta\phi$: The solid angle for the given kinematic bin. This term
³⁶⁹ includes the “detector acceptance”.
- ³⁷⁰ • $\eta_{detector}$ accounts for the detector efficiencies

371 The data analysis to extract the physics quantities involves accurately measuring
372 each of these quantities, either separately or in some combined form. To do so,
373 the data must be properly reconstructed, calibrated and corrected to build all the
374 scattering events during the experiment. Since the reconstructed events include a
375 wide range of physical processes in addition to the electron-deuteron scattering process
376 that we are interested in, proper event selection cuts must be applied. In this chapter,
377 all these steps from the data reconstruction and calibration through the extraction of
378 g_1 are described.

379

380 **3.1 Raw Data Processing - Calibration and Recon-** 381 **struction**

382 The raw data recorded by the CLAS DAQ system, which consists of ADC and TDC
383 values registered by various detector components as well as the beam related infor-
384 mation such as beam helicity and Faraday Cup readings, are organized into banks
385 (with each bank carrying data belonging to a particular detector component or some
386 part of it) and saved in special format (BOS) files. These raw data are next pro-
387 cessed with a standard CLAS software package called RECSIS, which analyzes and
388 combines the matching bits and pieces of the raw information to reconstruct parti-
389 cles and events that produced them. Such reconstruction produces output data that
390 consist of event and particle IDs, particle positions and energies and momenta (in the
391 lab frame CLAS coordinate system), and also some static particle properties such as
392 charge and mass. The reconstruction program uses geometric parameters and cali-
393 bration constants (from the CLAS Calibration Database) for the detector in order to
394 properly process and transform the raw data into the reconstructed tracks.

395 The first part of the data processing is the detector calibration. In this phase, a
396 small sample (about 10%) of raw data (uniformly selected over the entire run period
397 to ensure time stability verification) is chosen and the energy and time calibration
398 constants are adjusted to give the correct behavior while constantly monitoring related
399 variables. This is done separately for each run period to consider the different running
400 conditions, the possibility of unwanted changes in hardware that may have occurred,
401 as well as drift of detector response over time. This process of adjusting the calibration
402 constants and reconstructing the data is repeated until a desired level of accuracy is
403 reached. Once that level is reached, the calibration constants are “frozen” and the
404 final reconstruction is done. The resulting output is saved in especial formats¹. These
405 saved data provided the starting point for our higher level data analysis as described

¹Two especial data formats - BOS and ntuple (h10) - were used

406 in this document.

407 The iterative work of data reconstruction and detector calibration, which was
408 a very computing intensive and time consuming, was done by R. De Vita (in 2006-
409 2007) soon after the data collection was completed, which has been summarized in the
410 analysis note [20] by X. Zheng which has been approved by the hadron spectroscopy
411 working group. This analysis, meanwhile, has been published [21]. The data from
412 this “Pass1” reconstruction was first analyzed as part of the Ph. D. dissertations by
413 three graduate students, but during these analyses, a few anomalies² in reconstruction
414 were observed which were later tracked down to a mixing up of codes from two EG4
415 sub-packages for the reconstruction software. After the mix-up was sorted out, a new
416 pass (Pass2) of reconstruction was performed by L. El Fassi in 2014/15 (still using
417 the same calibration constants as used by the Pass1 reconstruction). The data from
418 this latest pass of reconstruction was used for the analysis reported in this note

419 **3.2 Helicity States**

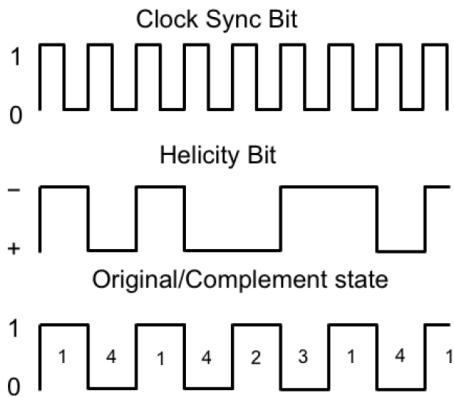


FIG. 3.1. Different data signals sent from the injector that monitor the helicity states of beam electrons. (Fig. courtesy of N. Guler [22]).

²The anomalies observed in the pass1 analysis were the discretized reconstruction of vertex and wrong reconstruction of track positions in DC1.

⁴²⁰ As we saw from Eq. 3.1, the physics extraction depends on measurements of the
⁴²¹ number of events in the two (+/-) electron helicity states. The CEBAF accelerator
⁴²² provides the polarized electrons in closely and equally spaced bunches. These bunches
⁴²³ are further grouped into “buckets” according to their helicity states, which are alter-
⁴²⁴ nated pseudo-randomly at the injector with a frequency of 30 Hz. The information
⁴²⁵ on the helicity state of each of the buckets and the total integrated charge contained
⁴²⁶ in it is injected into the DAQ data stream immediately after the helicity flip. Using a
⁴²⁷ combination of different types of sequence control signals sent from the injector (see
⁴²⁸ Fig. 3.1), it is possible to determine which helicity state a particular event belonged
⁴²⁹ to, which then can be used to label the helicity state of the event in the data stream,
⁴³⁰ together with the total beam charge of the state.

⁴³¹ 3.3 Electron Identification

⁴³² In CLAS electron-scattering experiments, the scattered electron defines the timing of
⁴³³ each event. In addition, in inclusive measurements, the scattered electron is the only
⁴³⁴ particle to be detected and measured. So, it is particularly important to make sure
⁴³⁵ that electrons are well measured and properly identified and are not contaminated
⁴³⁶ with misidentified particles such as negative pions (π^-) or lost by being misidentified.

⁴³⁷ The process of identifying the primary scattered electrons starts by first rejecting
⁴³⁸ all those particle candidates which are not the first entries (i.e., the trigger particles)
⁴³⁹ in the event bank. The remaining sample of the candidates is refined further by
⁴⁴⁰ rejecting those with positive charges. Then, the sample is further refined by applying
⁴⁴¹ a set of cuts that are listed and described below. An electron candidate is considered
⁴⁴² good if it passes all of these cuts.

⁴⁴³ 1. Good Electron Cuts

⁴⁴⁴ (a) **Cut on particle charge:** $q=-1$

⁴⁴⁵ (b) **Detector status cuts:**

⁴⁴⁶ i. **DC status:** $dc>0$; $dc_part>0$

⁴⁴⁷ ii. **SC status:** $sc>0$; $sc_part>0$

⁴⁴⁸ iii. **EC status:** $ec>0$; $ec_part>0$

⁴⁴⁹ iv. **CC status:** $cc>0$; $cc_part>0$

⁴⁵⁰ (For simulated data, all of the above except those on CC variables are
⁴⁵¹ used.)

⁴⁵² (c) **Electromagnetic Calorimeter Cuts** (see Sec. 3.3.1)

453 (d) **Osipenko cuts** Cuts on CC angle θ , ϕ and time matching between CC
454 and other detectors. (see Sec. 3.3.2)

455 (e) **Cut on minimum number of photoelectrons** (see Sec. 3.3.2)

456 2. Good Event Cuts

457 (a) **Cut on minimum number of particles detected and reconstructed**
458 **in the event:** gpart>0

459 (b) **Minimum/maximum momentum cuts** (see Sec. 3.3.3)

460 (c) **Sector cut** dc_sect = 6; cc_sect = 6 (to select electrons from the sector
461 where the low momentum Cherenkov detector was installed)

462 (d) **Scattering vertex-z cuts** (see Sec. 3.3.4)

463 (e) **Fiducial cuts** (see Sec. 3.3.5)

464 This data analysis relied on comparing the experimental data with a Monte-Carlo
465 simulated data set that was as realistic as practically possible. Thus, we also have
466 to analyze the simulated data in the same way as the experimental data. In the
467 ideal situation, all cuts would be the same for both experimental and simulated data.
468 However, we could not make our simulation match perfectly with our experimental
469 data. Therefore, some of the data selection cuts are defined separately for the two
470 cases and sometimes separately even for different Q^2 bins (to make sure we have the
471 same fractions of events in corresponding kinematic bins for both type of data).

472 3.3.1 Electromagnetic Calorimeter Cuts

473 The EC cuts consist of two different cuts applied together. One of these is on the
474 sampling fraction i.e. the fraction of the energy deposited in the calorimeter, and the
475 other is on the energy fraction deposited in the inner part of the calorimeter.

476 Cuts on EC sampling fraction

477 While moving through the EC, charged pions are minimum ionizing particles in the
478 momentum range detectable by CLAS. On the other hand, each electron deposits its
479 total energy E_{tot} in the EC³ by producing electromagnetic showers. Therefore, the
480 sampling fraction E_{tot}/p should be independent of the momentum for electrons (in
481 reality there is a slight dependence).

³Because some of the deposited energy is in the lead part of the EC rather than the scintillator, only a fraction of the electron energy is detected in the EC.

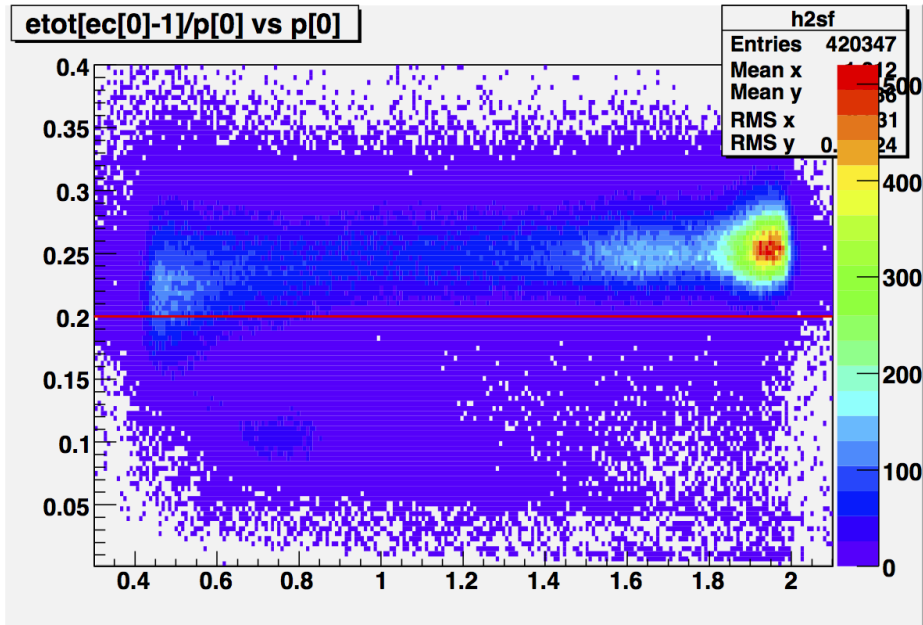


FIG. 3.2. An example of the cut on the EC sampling fraction (2.0 GeV data). The plots shows the distribution of the sampling fraction (in Y-axis) plotted against the particle momentum (in X-axis). The brighter stripe above about 0.2 in the energy fraction are due to the electrons whereas those below are the pions.

For the EC in CLAS, the electron sampling fraction ($etot/p$) is about 0.25 and pions give signals that are mostly below 0.2 (see Fig. 3.2 or others that follow). Therefore, a lower cut of $etot/p > 0.2$ is usually chosen to reject most of the pions without significantly losing good electrons. However, in our low beam energy experiment, few pions are produced and the electron peaks are cleaner in lower kinematic bins as can be seen in the low Q^2 bins of Fig. 3.3. Therefore, a Q^2 bin dependent cut of $etot/p > (\mu - 3\sigma)$ was chosen, where μ and σ are the Gaussian fit parameters representing the mean and standard deviation of the distribution in the corresponding Q^2 bin. The choice of 3σ was decided by looking at the sampling fraction distributions in each of the Q^2 bins and making sure that no pion signal was observed in any of the bins.

On simulated data also, a corresponding 3σ cut was applied by first repeating the exact same procedure to get the corresponding values of μ and σ from the simulated data. Using same- σ cuts in corresponding Q^2 bins of both experimental and simulated data ensures that we had the same fraction of data in corresponding bins from both experimental and simulated sides.

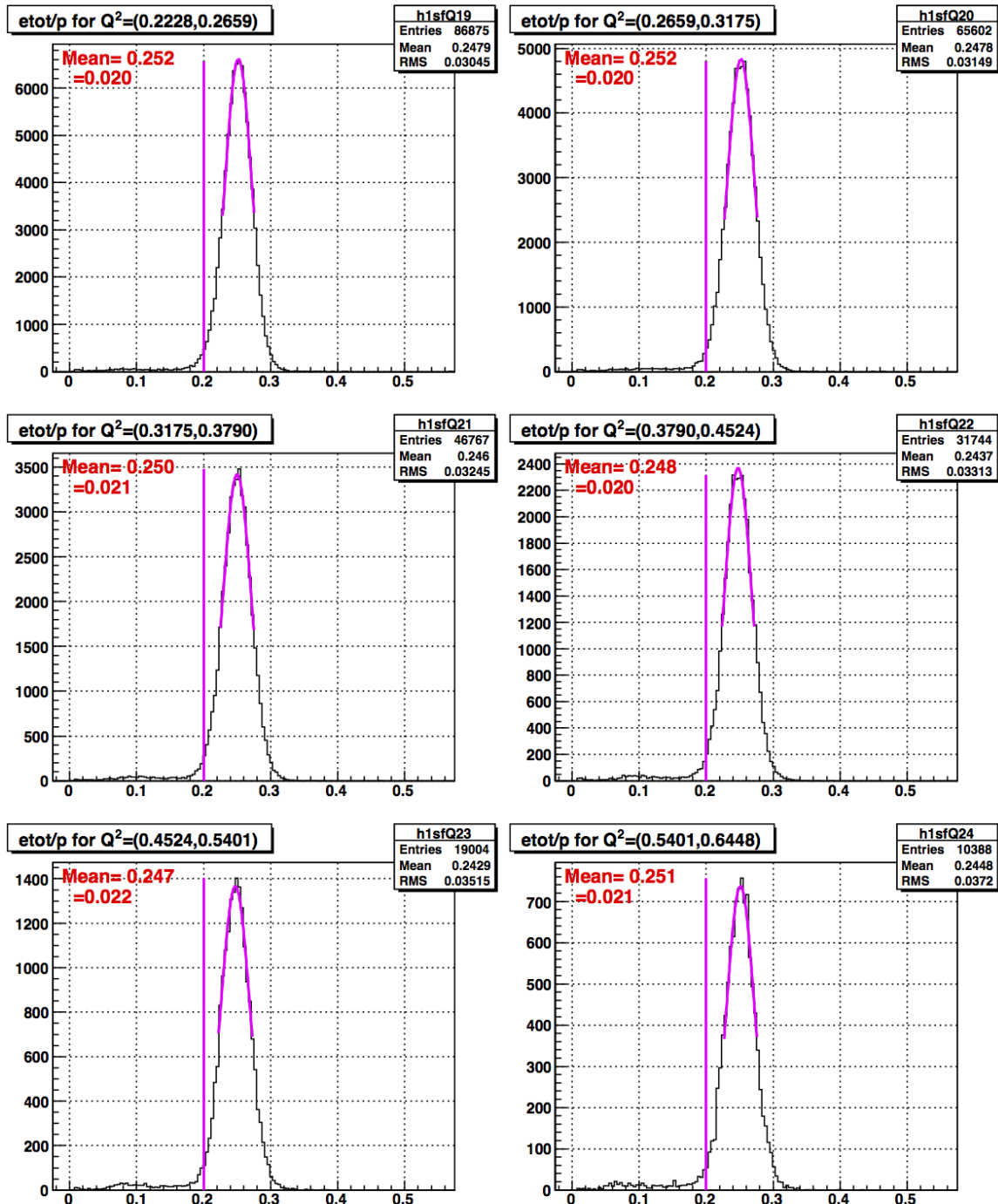


FIG. 3.3. The Q^2 dependent cuts on the EC sampling fraction for 2.0 GeV experimental data. Events below the red lines are rejected.

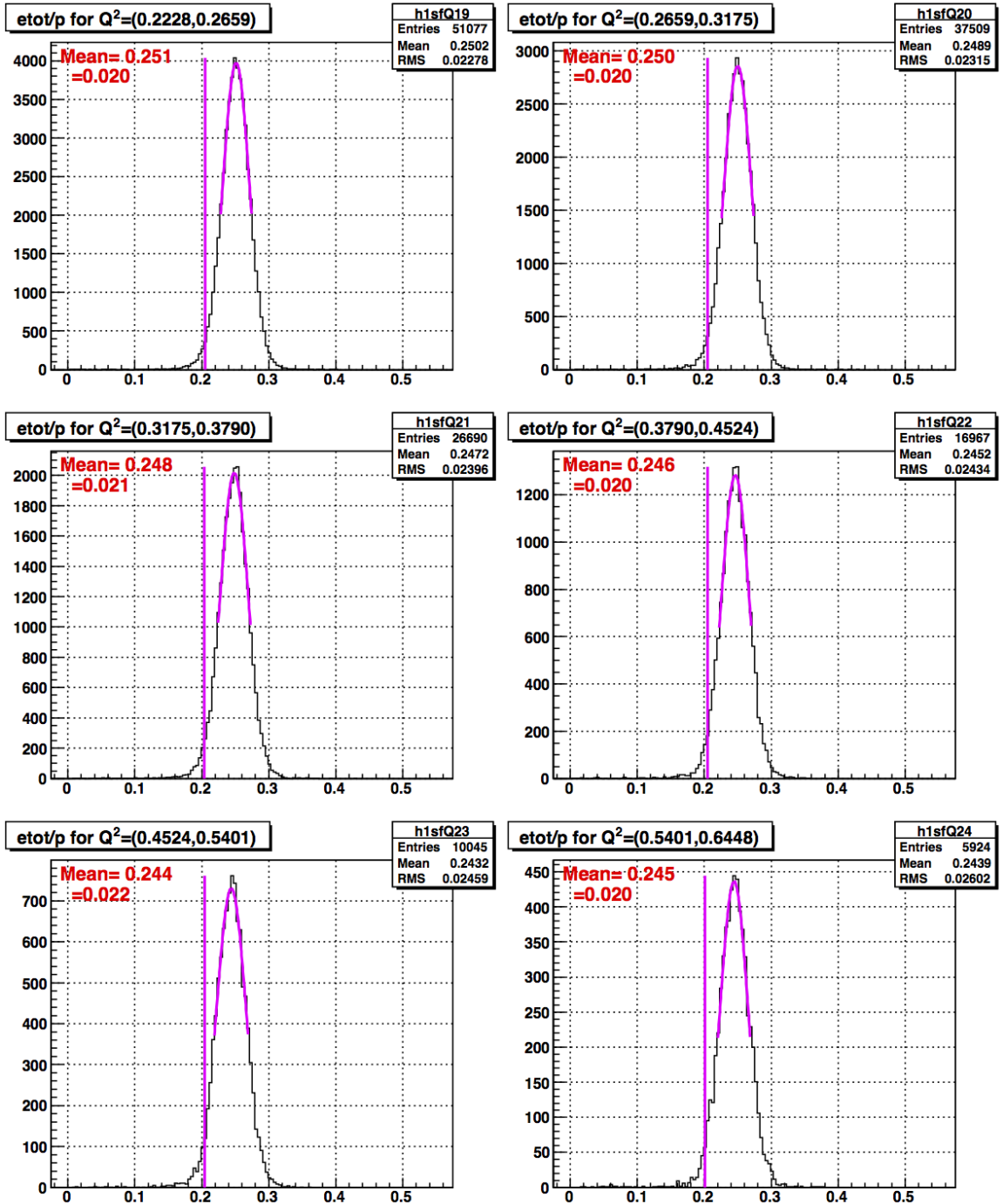


FIG. 3.4. The Q^2 dependent cuts on the EC sampling fraction for 2.0 GeV simulation data. Events below the red lines are rejected.

498 **Cuts on E_{in}**

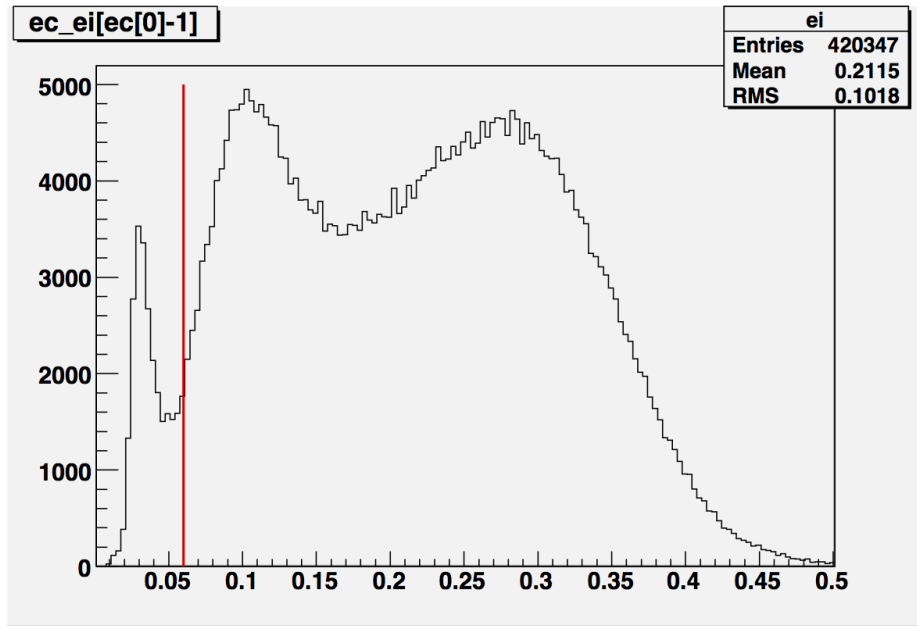


FIG. 3.5. Energy deposited (GeV) in the inner EC and the cut (red line) used to reject pions (seen as a peak at about 0.03 GeV) from a sample of electron candidates of 2.0 GeV data.

499 Pions, which do not shower and are minimum ionizing particles in the momentum
 500 range detected in CLAS, deposit only a small amount of energy in the inner part of
 501 the EC, independent of their momentum. When E_{in} is histogrammed, the small pion
 502 signal peak at about 0.03 clearly stands out from the large electron sample, with little
 503 overlap in between. So, a universal cut of $E_{in}=0.05$ on both data and simulation (as
 504 shown in Figs. 3.5, 3.6 and 3.7) safely rejects most of the pions from the electron
 505 candidate sample.

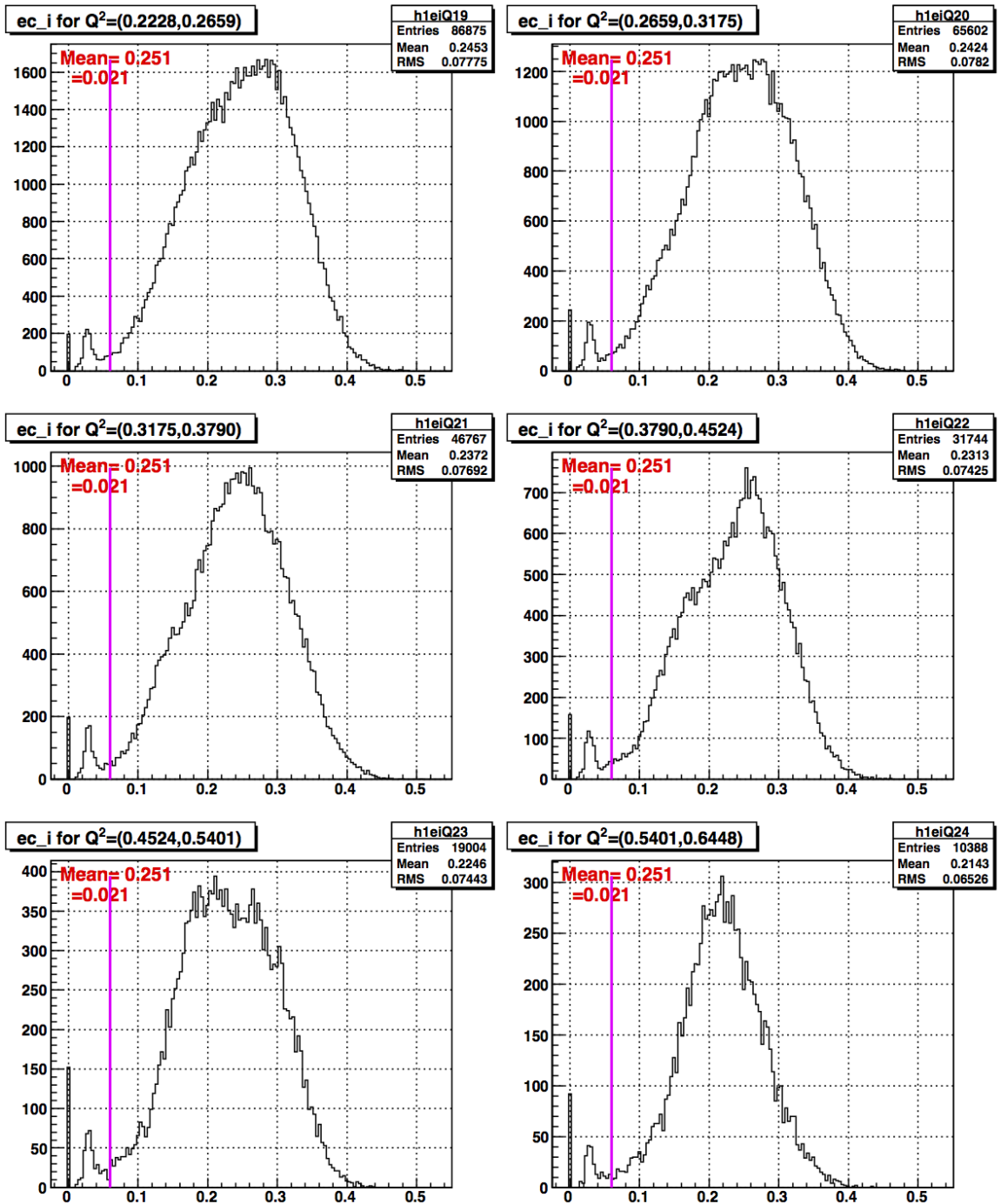


FIG. 3.6. The EC-inner cut on a sample of 2.0 GeV experimental data in various Q^2 bins.

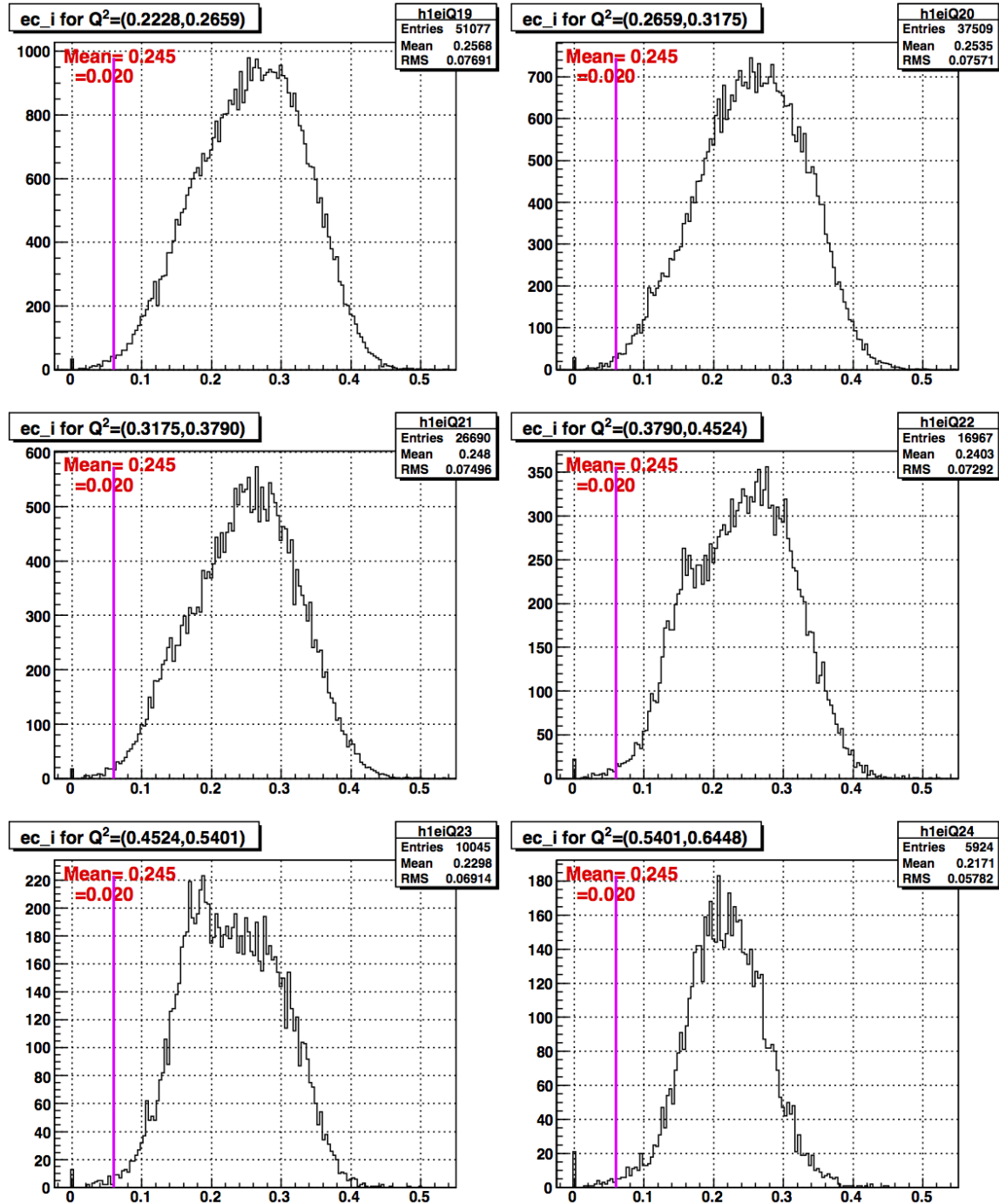


FIG. 3.7. The EC-inner cut on a sample of 2.0 GeV simulation data in various Q^2 bins.

506 **3.3.2 Cerenkov Counter Cuts**

507 **Osipenko (CC Geometry and Time Matching) Cuts**

508 As discussed in Sec. 2 the new EG4-dedicated CC consists of 11 modules each con-
509 sisting of a pair of mirrors and PMTs. The segments are placed along the CLAS
510 polar angle covering 15 to 45 degrees, i.e., the segments are at different polar angular
511 positions. During normal operation, the PMTs of these segments may produce ther-
512 mal noise that is equivalent to that produced by one photo-electron passing through
513 it. As a result, when a noise pulse in the CC and a pion track measured by DC
514 coincides within the trigger window of the CLAS detector, the track gets registered
515 as an electron candidate by the event reconstruction program, thus contributing to
516 the contamination of electron candidates with the misidentified pion tracks. In fact,
517 this turns out to be the biggest source of pion contamination. In order to minimize
518 such contamination and help better identify electrons from pions, CC geometric and
519 time-matching cuts are applied.

520 This category of cuts for this experiment is mostly based on a similar analysis
521 done for another CLAS experiment by M. Osipenko [20, 23].

522 The first requirement in the CC-matching is for the electron candidate track (as
523 reconstructed by DC) to have a corresponding signal in CC. In addition, the track
524 needs to meet several matching conditions to be acceptable as described in the next
525 sections.

526 **CC θ Matching** As said above, the CC segments are at different average polar
527 angle positions (between 15 and 45 degrees), so in principle, one can expect a one-to-
528 one correspondence between the polar angle of the track (as measured at the vertex)
529 and the CC-segment. However, the torus magnetic field bends the particles towards
530 or away from the beamline, so it's more convenient to use the CC projected polar
531 angle θ_{proj} rather than the vertex angle θ , where θ_{proj} is defined as the polar angle
532 of the position vector defined by the point of intersection of the track with the plane
533 at which the CC PMTs reside as reflected by the CC mirrors (another projected
534 angle ϕ_{proj} is the azimuthal angle of the same vector). These projected angles can
535 be uniquely calculated for each track based on the DC signals of the track as well as
536 the CC geometry information. To simplify the later analysis process, these projected
537 angles for each track were calculated during the final data reconstruction process and
538 then saved in the output files just like all the other information for the events and
539 particles. Finally, for the actual electrons a one-to-one correspondence between θ_{proj}
540 and the segment number can be established, which discriminates against background
541 noise and the accidental pions (or any other negative charge candidates). For each
542 segment, the θ_{proj} distribution (see Fig. 3.8) is fitted with a gaussian to determine its

543 mean (μ) and width (σ) and then saved for future use in cuts. These fit parameters
 544 are then used during the data analysis to define these CC- θ -matching cuts. The
 545 events that have $\mu - 3\sigma < \theta_{proj} < \mu + 3\sigma$ pass this cut, and the others are rejected as
 546 not genuinely being electrons.

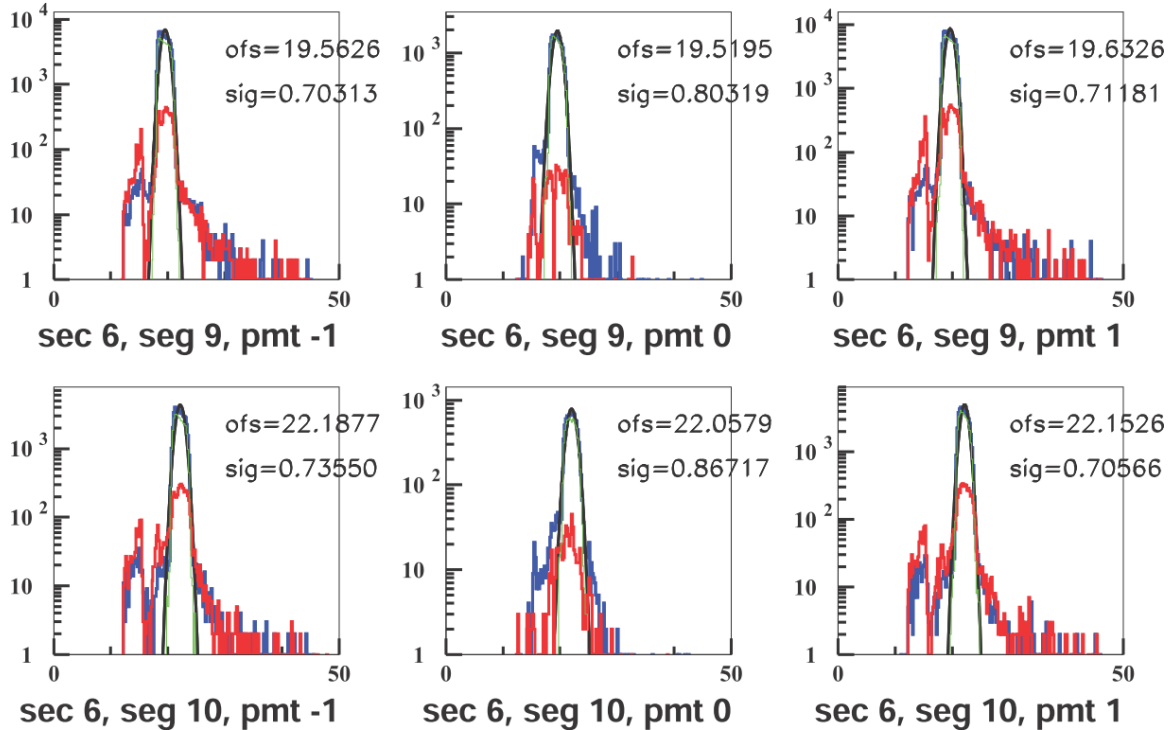


FIG. 3.8. The θ_{proj} distributions in two (9th and 10th) of the CC-segments (figures used from [20]). Here, the first, second and third columns correspond to events that fired the left, both and the right PMTs respectively. The blue lines are for good electron candidates that pass the EC cuts as well as $Nphe > 2.5$. The red ones are for those that pass the EC cuts but with $Nphe < 2.5$ (thus likely pions), and the green lines (not visible due to being nearly identical to the blue ones) are for those which pass both EC cuts and all Osipenko cuts. The Gaussian fits which are used to define the θ matching cuts are shown in black ("ofs" and "sig" in the panel refer to μ and σ , respectively). If the candidate falls outside $\pm 3\sigma$ limits given by the fit, θ_{proj} is taken as not matching with the corresponding segment and, therefore, the event is rejected.

547 **CC ϕ Matching** One can also have a one to one correspondence between the other
 548 CC-projected angle ϕ_{proj} and the left or right PMT in the corresponding CC-segment,
 549 because when the track is on the right side of the CC, the right PMT should fire and
 550 vice versa. However, there are some exceptional cases of events which fire both PMTs.
 551 That happens when ϕ_{proj} of the track is less than 4 degrees (when measured relative

552 to the sector mid-plane), in which case the Cherenkov light hits both PMTs but with
 553 less efficiency (because the Cherenkov photons are shared between the two). Fig. 3.9
 554 shows for two of the segments the ϕ_{proj} distributions and the Gaussian fits that are
 555 used to define these cuts.

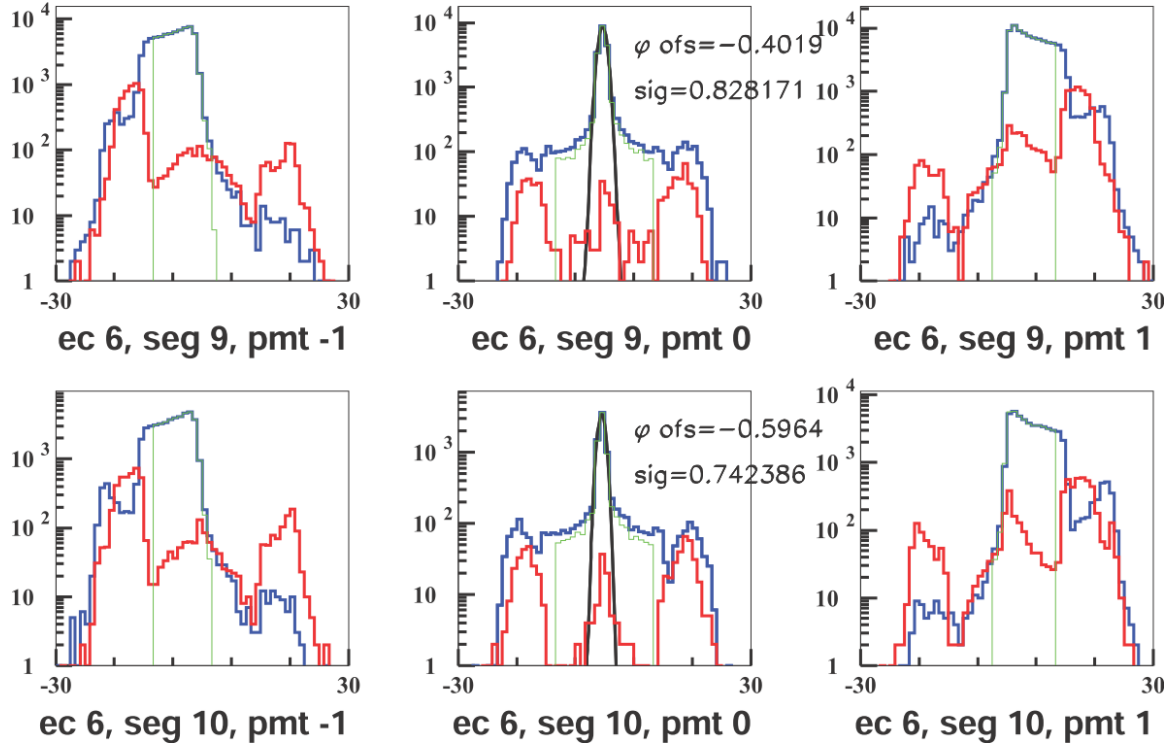


FIG. 3.9. The ϕ_{proj} distributions in two (9th and 10th) of the CC-segments (figure used from [20]). Here, the first, second and third columns correspond to events that fired the left, both and the right PMTs respectively. The blue lines are for good electron candidates that pass the EC cuts as well as $Nphe > 2.5$. The red ones are for those that pass the EC cuts but with $Nphe < 2.5$ (thus likely pions), and the green are for those which pass both EC cuts and all Osipenko cuts. The Gaussian fits to the distributions that fired both left and right PMTs are shown in black ("ofs" and "sig" in the panel refer to μ and σ , respectively). If the candidate falls outside 3σ on the positive (negative) side but the left (right) PMT is fired, we take it as having left-right inconsistency and, therefore, the event is rejected. In other words, if $\theta < \mu - 3\sigma$ but $PMT = 1$, or if $\theta > \mu + 3\sigma$ but $PMT = -1$, the event is rejected.

556 **CC Time Matching** The difference ΔT between the track time recorded on a CC
 557 segment and the corresponding time recorded on the TOF (or SC), corrected for the
 558 path length from the CC to the TOF, is used to define one of the time-matching cuts

559 $\Delta t_{SC-CC} > -6.0\text{ns}$ which was chosen to reduce pion contamination without losing
 560 too many electron candidates (see Fig 3.10). Likewise, the time between CC and EC
 561 is also used to define another cut $\Delta t_{EC-CC} > -6.0\text{ns}$ (see Fig 3.11) to further reduce
 562 the pion contamination.

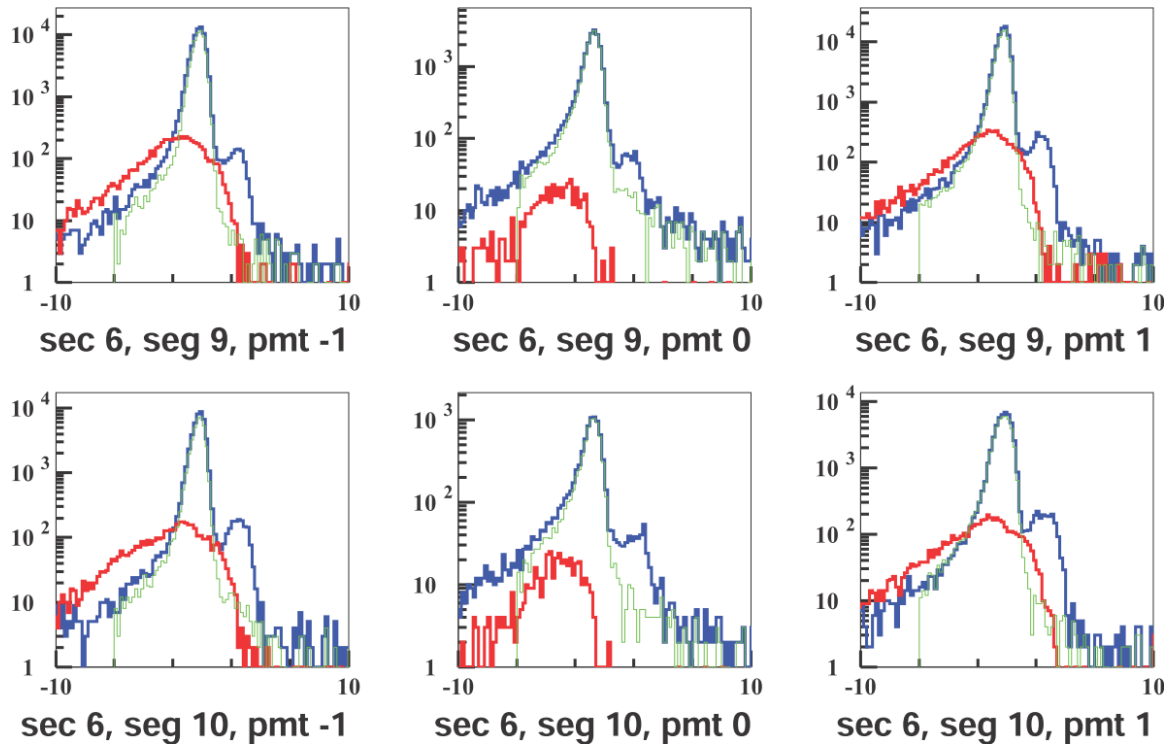


FIG. 3.10. The Δt_{SC-CC} distributions for two of the CC-segments (figure used from [20]). Here, the first, second and third columns correspond to events that fired the left, both and the right PMTs respectively. The blue lines are for good electron candidates that pass the EC cuts as well as $N_{phe} > 2.5$. The red ones are for those that pass the EC cuts but with $N_{phe} < 2.5$ (thus likely pions), and the green are for those which pass both EC cuts and all Osipenko cuts. The $\Delta t_{SC-CC} > -6.0\text{ns}$ cut was chosen to reduce pion contamination without losing too many electron candidates. (The small peaks at about +3 ns are due to particles hitting PMTs directly.)

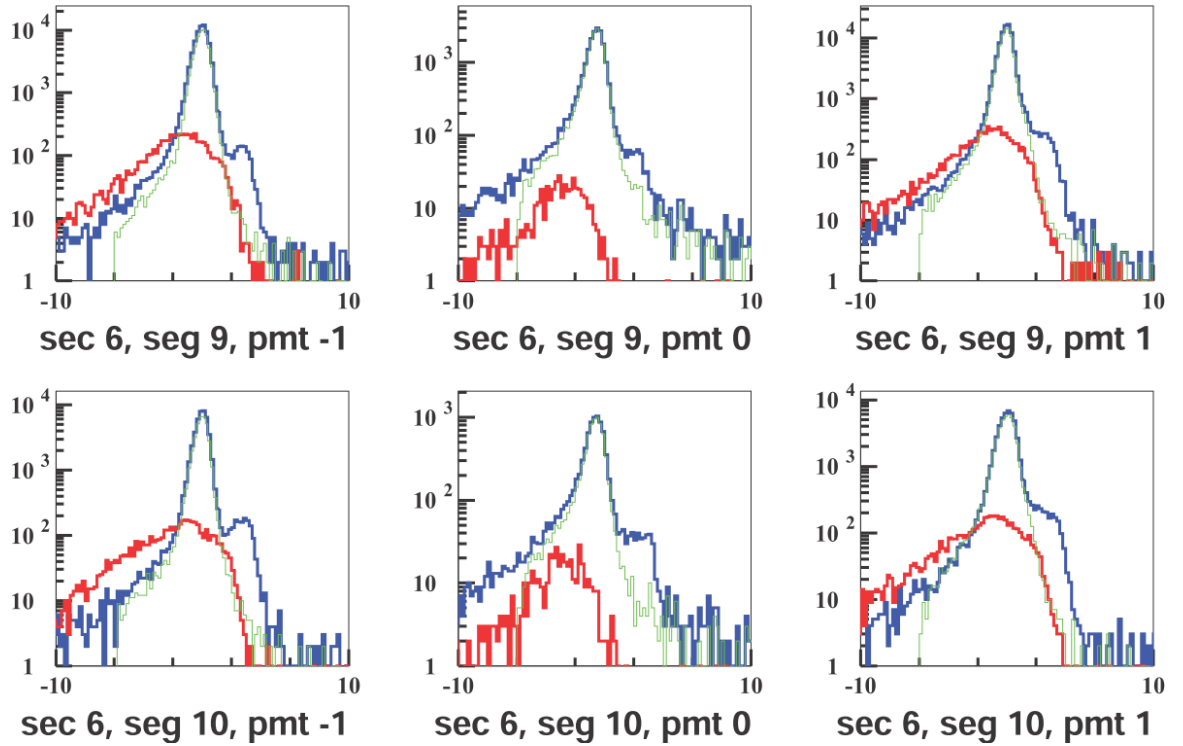


FIG. 3.11. The Δt_{EC-CC} distributions for two of the CC-segments (figure used from [20]). Here, the first, second and third columns correspond to events that fired the left, both and the right PMTs respectively. The blue lines are for good electron candidates that pass the EC cuts as well as $Nphe > 2.5$. The red ones are for those that pass the EC cuts but with $Nphe < 2.5$ (thus likely pions), and the green are for those which pass both EC cuts and all Osipenko cuts. The $\Delta t_{EC-CC} > -6.0\text{ns}$ cut was chosen to reduce pion contamination without losing too many electron candidates. (The small peaks at about +3 ns are due to particles hitting PMTs directly.)

563 Cut on Minimum Number of Photoelectrons

564 The “nphe” variable in the data ntuple which represents the ADC signal from the
 565 CC converted to “number of photoelectrons” and multiplied by 10 is also used to
 566 discriminate electrons from pions and the background. The number of photoelectrons
 567 produced in CC by an electron is typically between 5 and 25 or between 50 and 250 in
 568 the units of nphe, where the electronic background and negative pions produce signals
 569 equivalent to one photo-electron (or 10 in nphe units) and so a cut is determined
 570 somewhere between these two regions based on the shapes and sizes of the electron
 571 and pion peaks. In our case, we chose to have the cut $Nphe > 25$ as depicted by the
 572 straight line in Fig. 3.12.

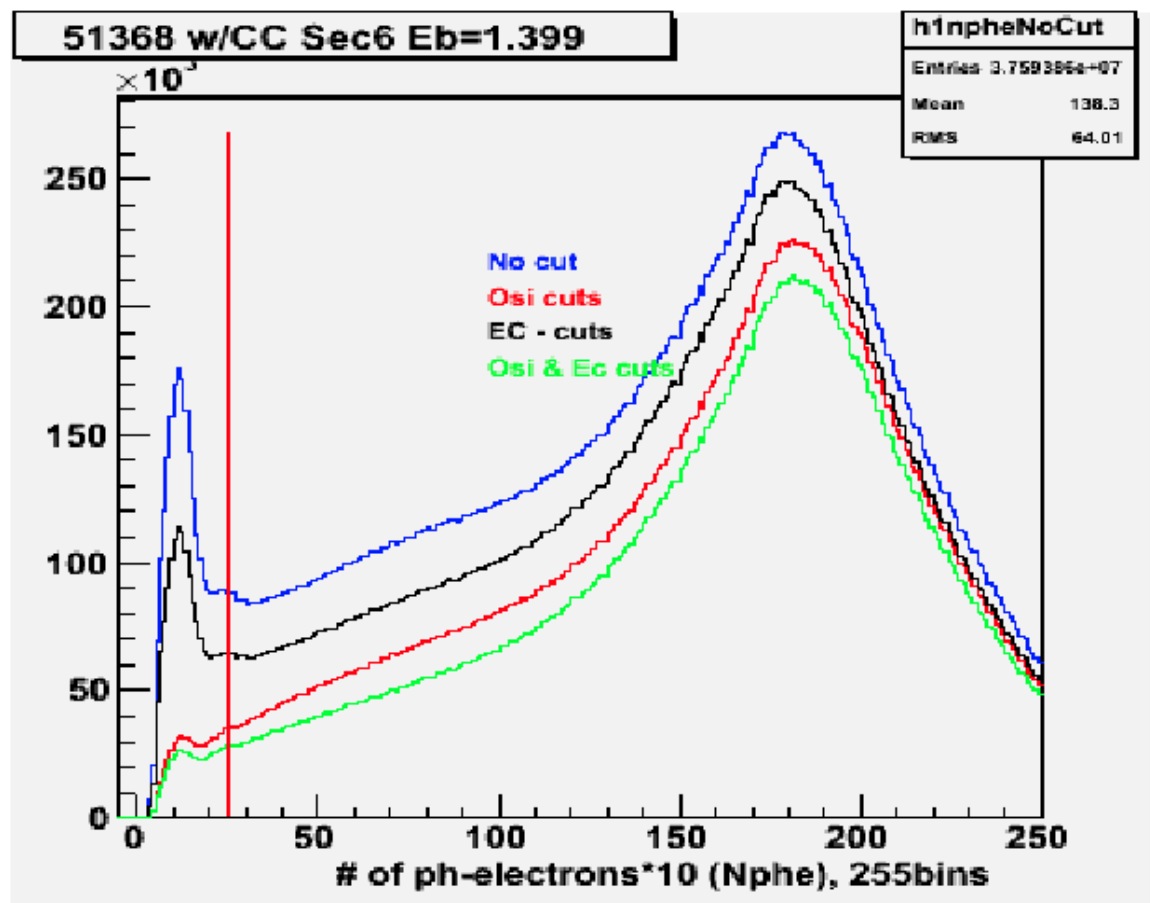


FIG. 3.12. The cut (the red straight line at 25) on the number of photo-electrons produced in CC times 10 (from 1.3 GeV data). The signals below the red line are mostly pions and noise and above the line are mostly electrons. We also see the effects of overall EC cuts, overall Osipenko cuts and the effect of both when applied together.

573 3.3.3 Minimum/Maximum Momentum cuts

574 A study [24] of the inclusive cross section at various beam energies in CLAS developed
 575 a parametrization of the low momentum cut p_{min} as a function of the calorimeter low
 576 trigger threshold (in milli-Volts)

$$p_{min} \text{ (MeV)} = 214 + 2.47 \times EC_{threshold} \text{ (mV)} \quad (3.2)$$

577 The low threshold for EC-total energy for EG4 was 65 mV [25], so, the minimum
 578 momentum cut was determined to be at: $p_{min} = 0.37 \approx 0.4 \text{ GeV}$. In addition, another
 579 minimum cut of $p_{min} = 0.2 * E_{beam}$ was added, so the actual minimum cut amounted
 580 to the larger of those two. Likewise, the momentum cannot be more than that of
 581 the beam energy (in natural units), therefore, the upper cut on the momentum is:
 582 $p_{max} = E_{beam}$.

583 Figure 3.13 shows the momentum distribution of the electron candidates for the
 584 2 GeV data and the minimum and maximum cuts.

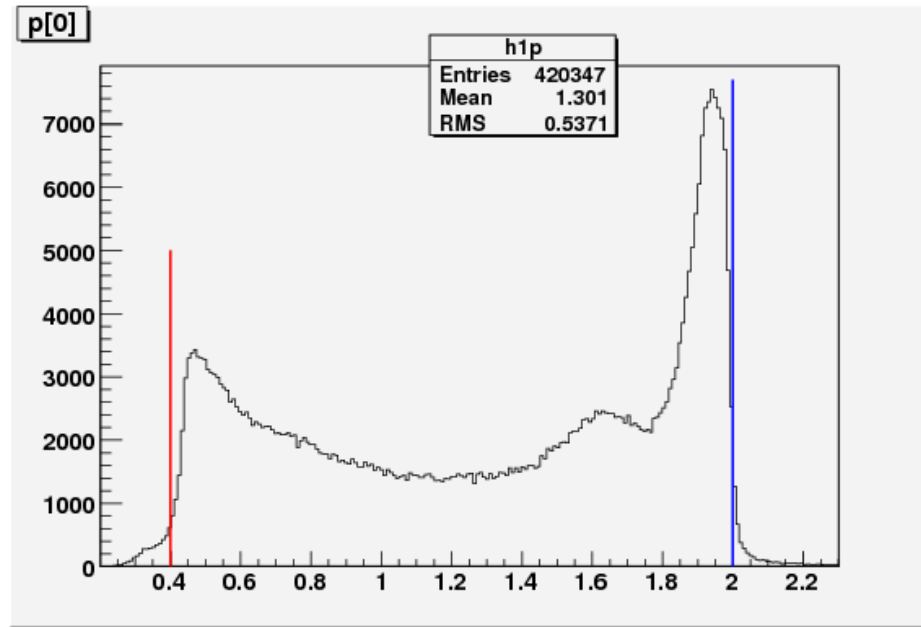


FIG. 3.13. The maximum and minimum momentum cuts (on 2.0 GeV ND₃ data).

585 3.3.4 Vertex-Z cuts

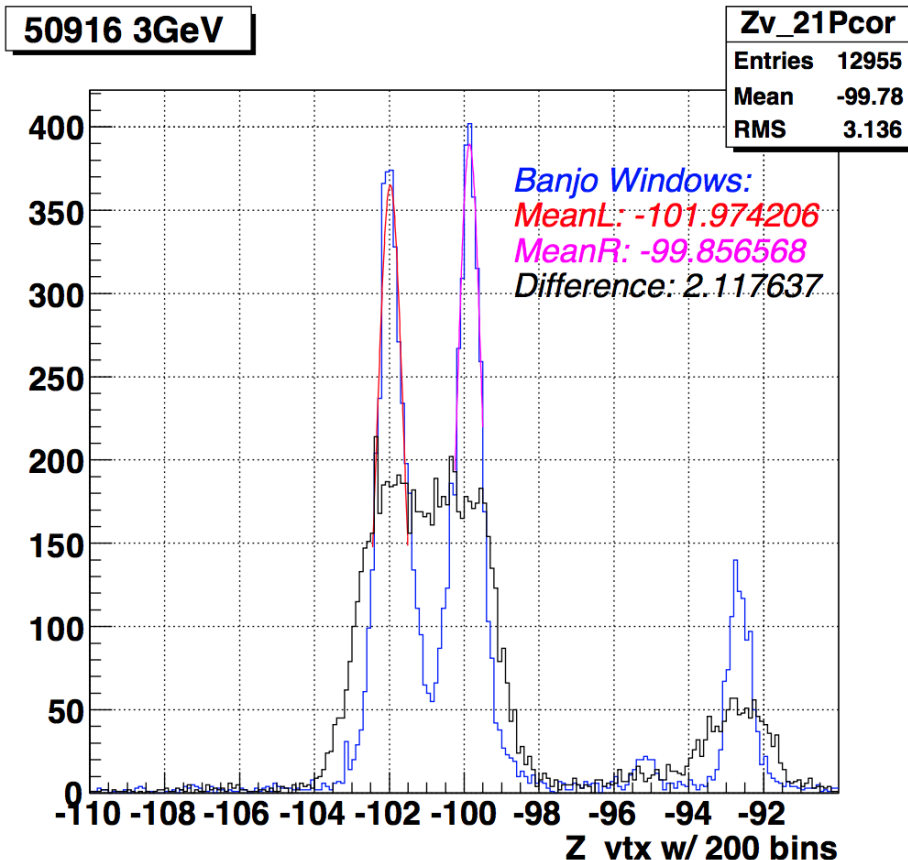


FIG. 3.14. Z-distribution of electron vertices which scattered off an empty cell target (with no Helium) from a 3.0 GeV run (50916) before (black) and after (blue) the vertex corrections. The two big peaks at about $z = -102$ and -100 cm arise from the scattering of electrons off the Al windows of the target chamber (also known sometimes as Banjo) and the other small peaks are from insulation aluminized mylar foils along the beam path downstream of the target. From the mean values of the Gaussian fits to the bigger two peaks, it was determined that the banjo length was $2.13 \pm 0.2\text{cm}$ and the actual polarized target position was -100.93cm (by averaging over similar estimates from all beam energy cases).

586 In the EG4 experiment, the ND₃ polarized target was of 1 cm long and was placed
 587 at ($x = 0$, $y = 0$, $z = -100.93$ cm)⁴ in the CLAS coordinate system. Since the beam
 588 electrons have to go through a few foils before reaching the target as well as the

⁴Although, the nominal value of the z-coordinate of the target position was -101.0 cm, the actual value was determined by doing the Gaussian fits of the double peaks in the vz-distribution of

589 detector, we want to reject electron tracks with vertices outside the target volume.
 590 For this purpose, use a cut on the reconstructed vertex co-ordinate “ v_z ”. However the
 591 vertex resolution demands reasonably wide “ v_z ” cuts so as not to lose too many good
 592 events. That is why the distribution of “ v_z ” was studied and based on the position
 593 and width of the distribution as well as our knowledge of the location of various foils
 594 and target materials, the cuts on “ v_z ” were decided. It was seen (see Figs. 3.15 and
 595 3.16) that the resolutions get worse and the distributions get wider as we go to lower
 596 Q^2 values, so again Q^2 dependent cuts were chosen for both data and simulation with
 597 the cuts tightening as Q^2 increases.

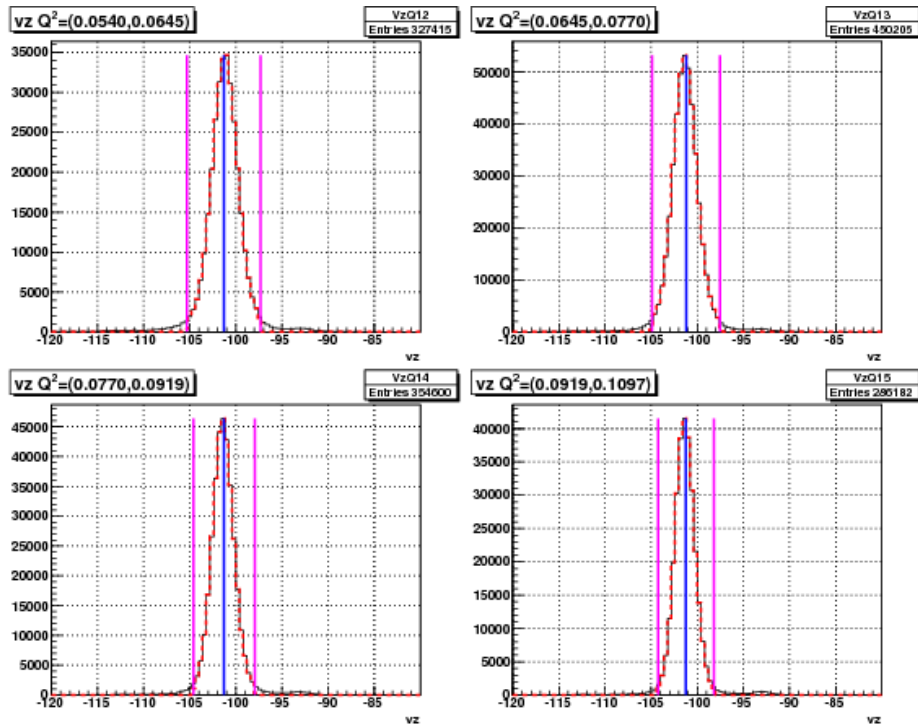


FIG. 3.15. 2.0 GeV data showing the Q^2 dependent v_z -cuts (the magenta lines on the left and right of the peaks) in some of the Q^2 bins. The continuous black line represents events before applying all the other event selection cuts (except on v_z) and the thicker dotted red line are the events after the cuts. The blue lines are the centers of the distributions, from which the cuts are 3 times σ away on each side, where σ is the standard deviation for the distribution in the given Q^2 bin (both the central value and the σ are determined during the cut development studies).

electrons from the empty-cell data runs as shown in Fig. 3.14. The average position of the target was calculated to be the average of the mean positions of these two double peaks which represent the two Al windows of the target chamber.

598 As in the case of EC variables, the reconstructed “ v_z ” distribution in the simu-
 599 lation does not come out quite the same as in the experimental data . To have the
 600 same fraction of events in the corresponding Q^2 bins as in the experimental data, a
 601 separate set of cuts (determined based on the distributions of both types of data)
 602 had to be used for simulation. For this purpose, the Gaussian fit parameters μ and
 603 σ (representing the mean and standard deviation) for all the Q^2 bins were tabulated
 604 separately for both data and simulation and separate sets of $\pm 3\sigma$ cuts were deter-
 605 mined for all bins. For example, if μ_q and σ_q were the two Gaussian fit parameters
 606 for the q^{th} Q^2 bin of either data or simulation, then the lower and upper cuts for “ v_z ”
 607 for that data set in the given Q^2 bin would be $\mu_q - 3\sigma_q$ and $\mu_q + 3\sigma_q$ respectively (as
 608 shown by the magenta vertical lines in Figs. 3.15 and 3.16).

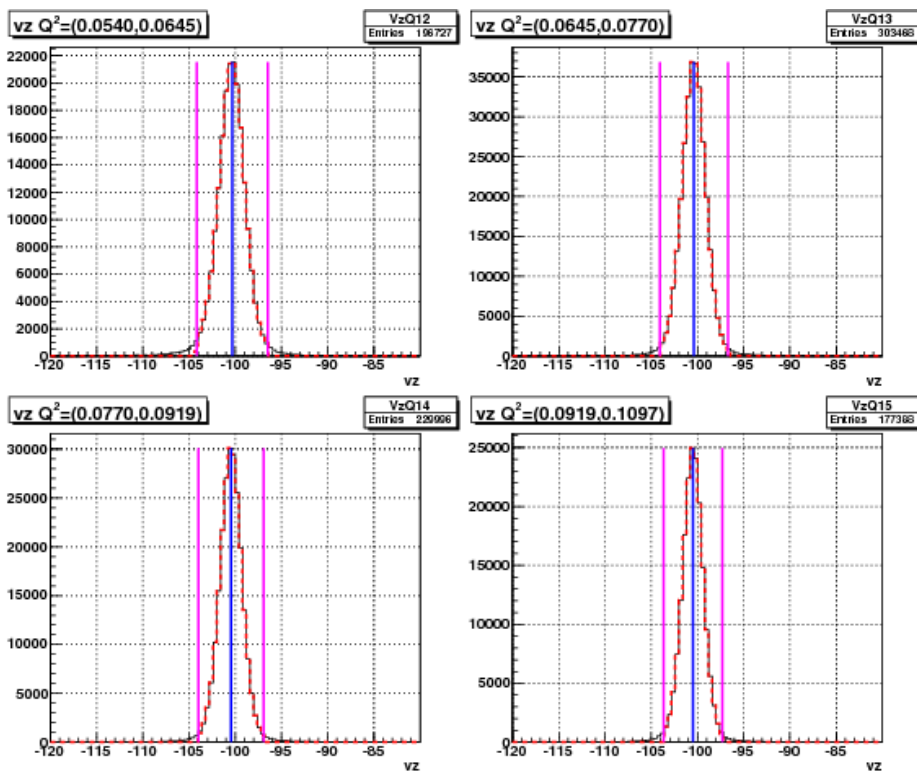


FIG. 3.16. Q^2 dependent v_z -cuts on simulation data (similar to Fig. 3.15).

609 3.3.5 Fiducial Cuts

610 Similar to the cuts discussed so far, we also had to match the region of good efficiency
 611 of the physical detector with the corresponding region from the simulation. For the
 612 experimental and simulation data to be comparable, they must have the same detector

613 acceptance. Two event variables polar angle (θ_{vtx}) measured at the vertex and the
 614 azimuthal angle ϕ_{DC1} measured at the drift chamber layer 1 are chosen to define
 615 the good efficiency regions of the detector. The reason for the choice of the variable
 616 θ_{vtx} should be obvious because it is directly related with the kinematic variables Q^2
 617 and W used in the analysis. However, due to the momentum dependent rotational
 618 effect of the magnetic field on the reconstructed azimuthal angle (ϕ_{vtx}) at the vertex,
 619 the angle ϕ_{DC1} is preferred over ϕ_{vtx} to define the fiducial region because that allows
 620 the easy selection (rejection) of the events which passed through and got detected by
 621 the more (less) reliable central (marginal) regions of the Cerenkov Counters. After a
 622 careful and extensive study of the event distributions on both data and simulation,
 623 we arrived at four sets of fiducial cuts in terms of the variables θ_{vtx} , ϕ_{DC1} and the
 624 torus current normalized inverse momentum i.e., $I_{torus}/(2250p)$.

625 The first set (see Fig. 3.17) of fiducial cuts were determined by comparing regular
 626 and EC-only data (which were taken using triggers that didn't involve CC) and
 627 selecting cuts such that regions with relatively darker spots (reflecting very low CC-
 628 efficiency) were rejected.

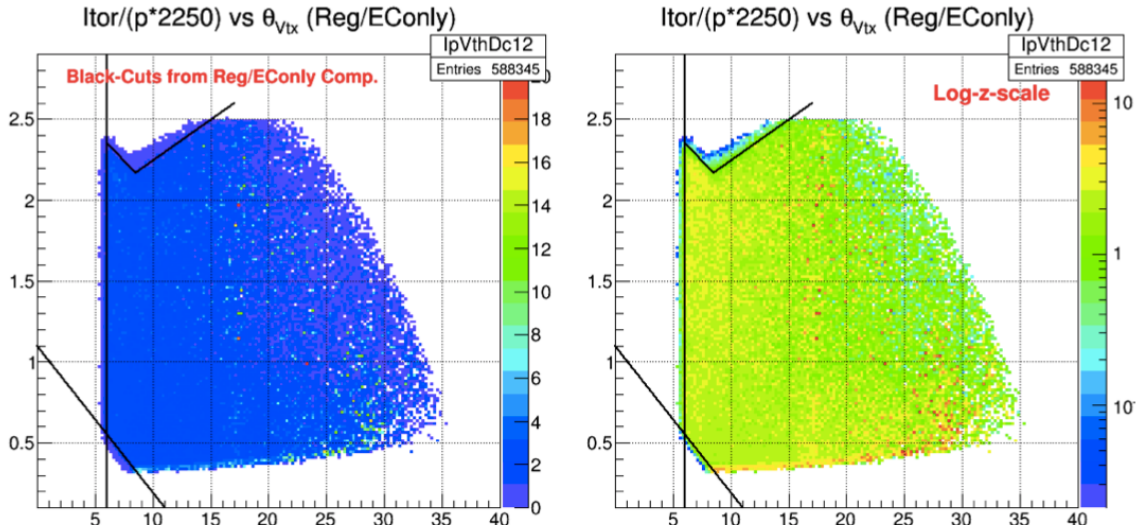


FIG. 3.17. Fiducial cuts determined by comparing the distributions of regular and EC-only **experimental data** as a function of $I_{torus}/(2250p)$ and θ_{vtx} . Here in the top panels, we see distributions of ratios of the regular and EC-only data respectively in linear and log scales in the color axis respectively. Inefficient regions of the CC are excluded using the indicated cuts.

629 The second set of cuts came from a similar comparison between the regular and
 630 EC-only data in the $I_{torus}/(2250p)$ vs θ_{vtx} (instead of θ_{DC1}) space (see Fig. 3.18) .

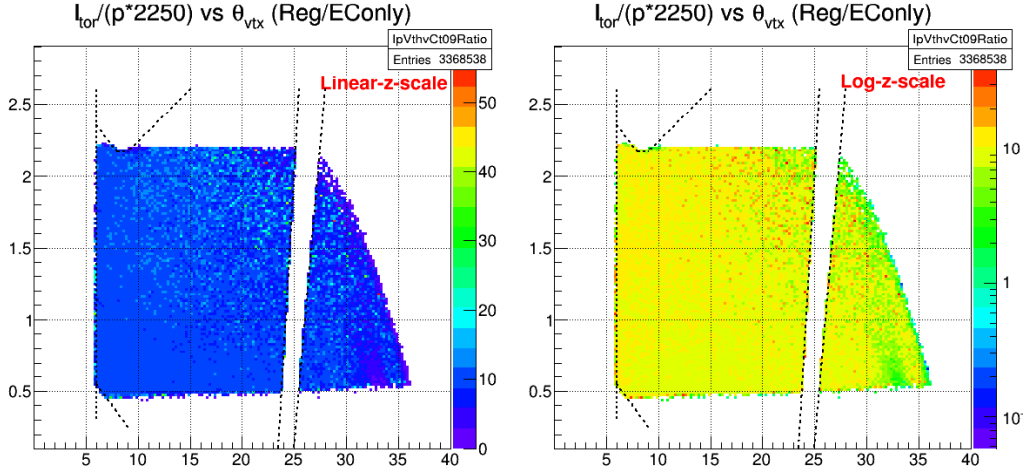


FIG. 3.18. Fiducial cuts determined by comparing the distributions of regular and EC-only **experimental data** as a function of $I_{torus}/(2250p)$ and vertex angle θ_{vtx} . Here, the vertical cut near $\theta_{vtx}=25$ degrees is to avoid the region of low efficiency possibly due to dead wires in DC.

631 The third set of cuts came from a comparison between the experimental and the
 632 corresponding simulated data as shown in the Fig. 3.19. as indicated by various
 633 straight lines in the two plots.

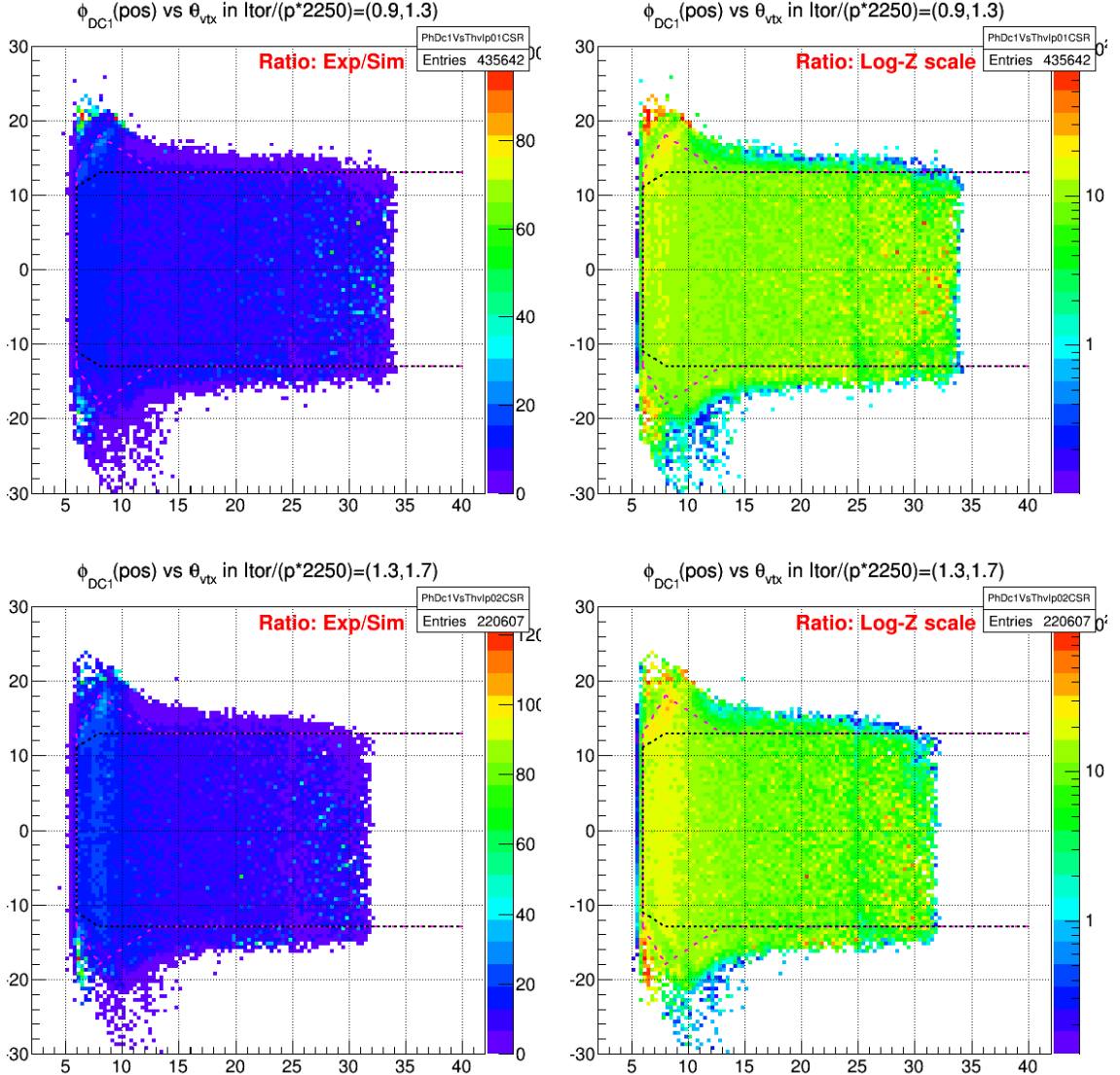


FIG. 3.19. Distribution (in two of six bins of $I_{torus}/(2250p)$) of ratios of **experimental** and **simulated** data (for 2.0 GeV) (both in linear and log-z scales) as a function of vertex angle θ_{vtx} and azimuthal angle ϕ_{DC1} as measured by the track position at the first drift chamber layer (angles in degrees). The dotted lines indicate the fiducial cuts for accepting good electrons.

634 Lastly, further sets of cuts were developed based on the distribution of the average
 635 number of photo electrons (nphe) as recorded by the Cerenkov Counter (CC) (see Fig.
 636 3.22).

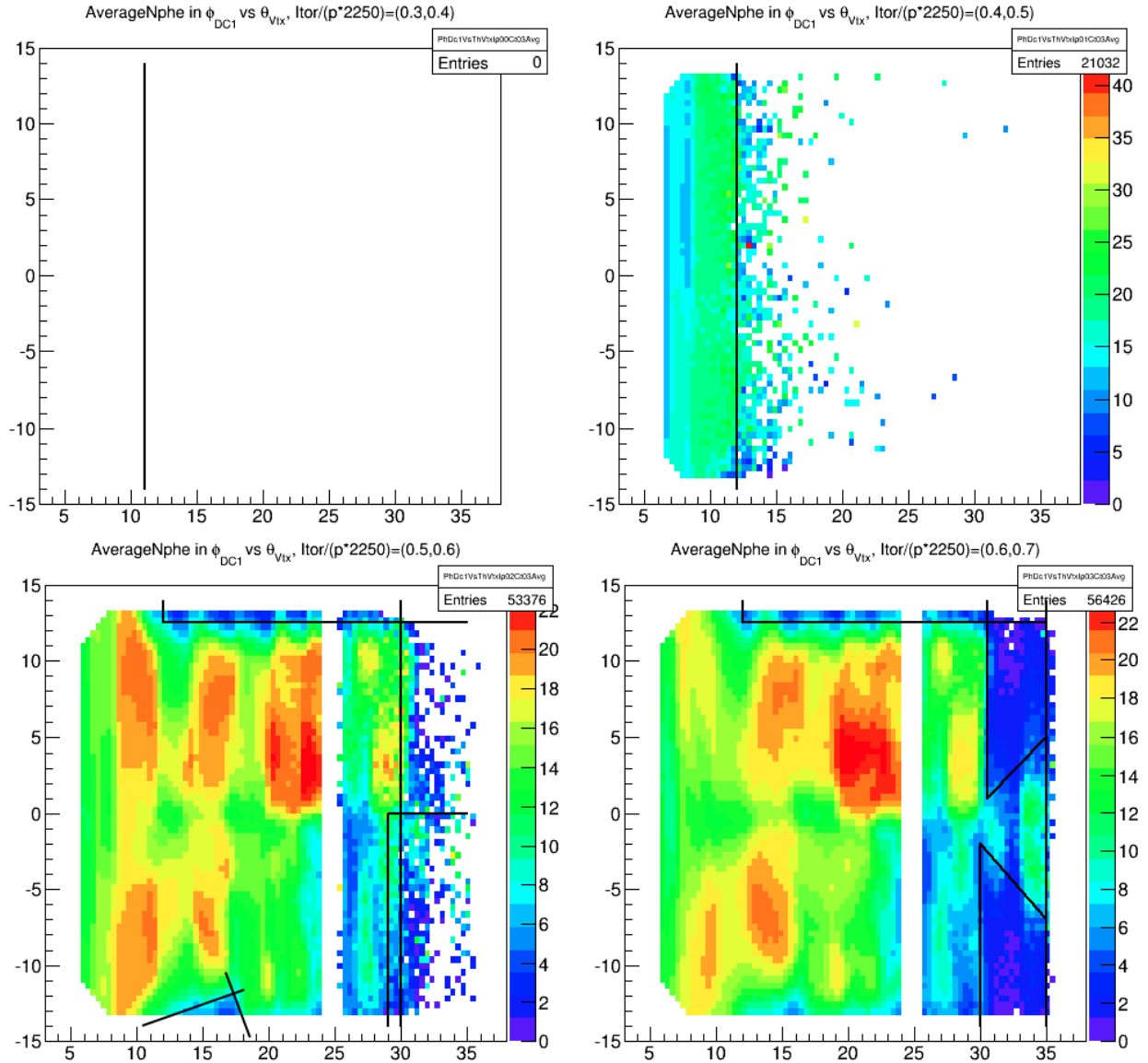


FIG. 3.20. Average Nphe distributions as a function of ϕ_{DC1} (along Y-axis) and θ_{vtx} (along X-axis) in first four bins of $\frac{I_{tor}}{p \cdot 2250}$. The black lines show the cuts that reject the very low CC-inefficiency regions.

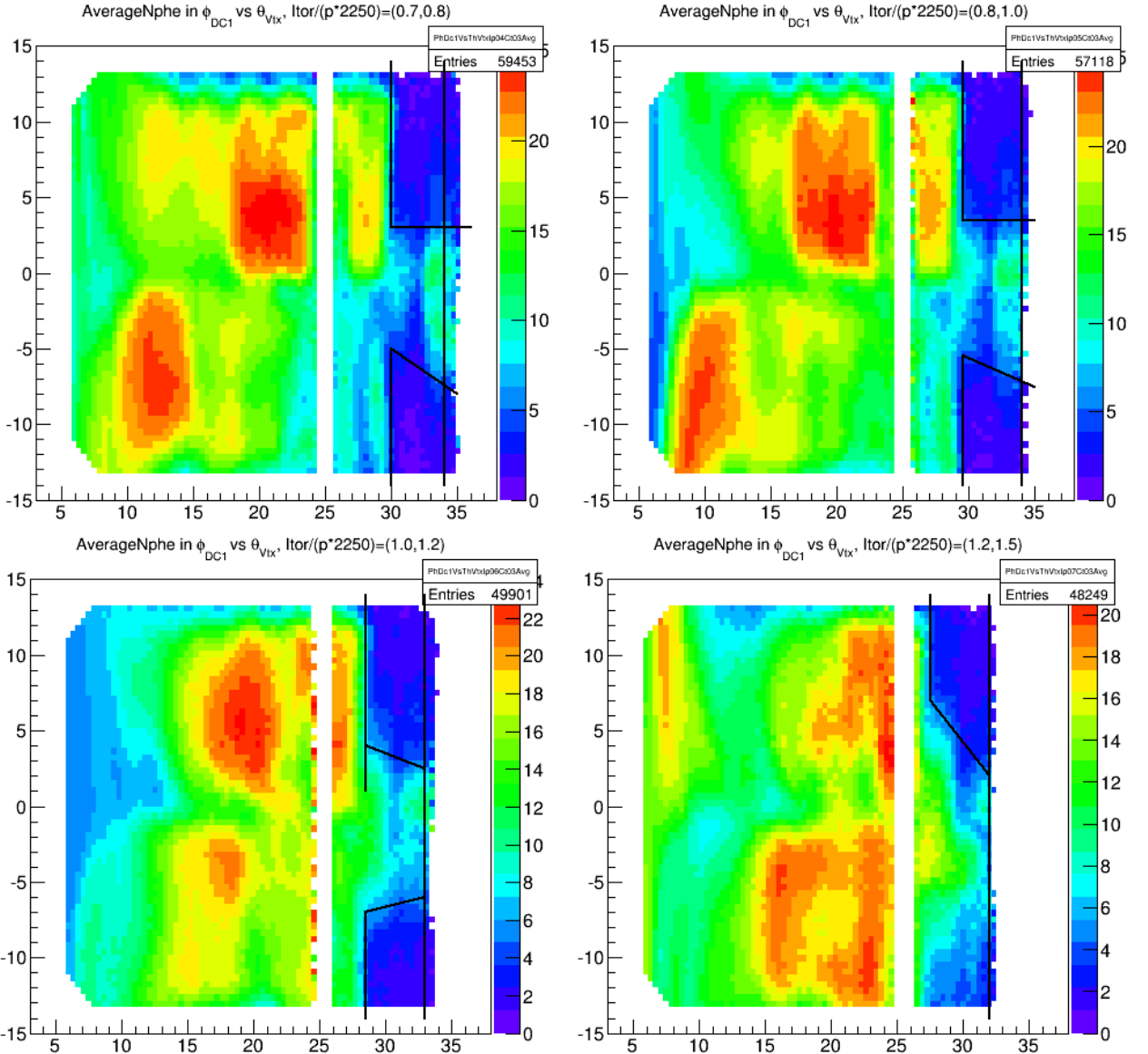


FIG. 3.21. Average Nphe distributions as a function of ϕ_{DC1} (along Y-axis) and θ_{vtx} (along X-axis) in next four bins of $\frac{I_{tor}}{p \cdot 2250}$. The black lines show the cuts that reject the very low CC-inefficiency regions.

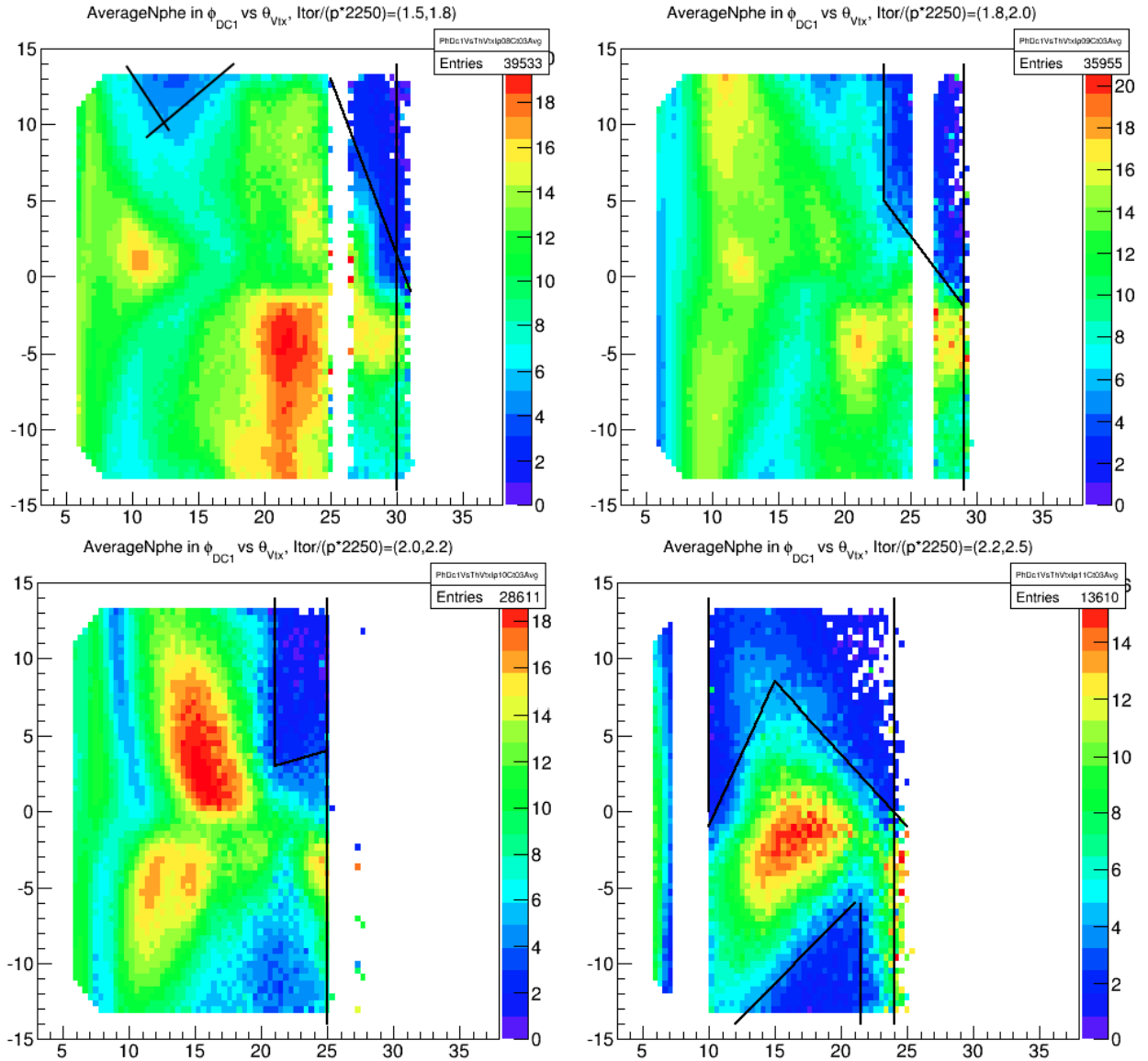


FIG. 3.22. Average Nphe distributions as a function of ϕ_{DC1} (along Y-axis) and θ_{vtx} (along X-axis) in last four bins of $\frac{I_{tor}}{p \cdot 2250}$. The black lines show the cuts that reject the very low CC-inefficiency regions.

637 3.4 Data Quality and Stability Checks

638 With an available set of good event/electron selection cuts, beam charge (measured by
 639 Faraday cup) normalized total event counts (sometimes also known as event “yield”),
 640 as well as polarization dependent differences, were calculated for each of the data files
 641 for all the runs and then plotted against the run number to study the data quality
 642 and stability as shown in Figs. 3.23, 3.24 and 3.25.

643 If nothing unusual happened or if the experimental conditions are not changed,
 644 then it is expected that the event yield as well as the count differences remain constant
 645 over time. Therefore, the graphs of these event counts plotted versus time or run
 646 number (which also roughly reflect the flow of time) should indicate the stability and
 647 quality of the data collected. For example, Fig. 3.23 shows such a total yield plot
 648 for all the data files from the 2.0 GeV beam energy data set on deuteron target. We
 649 can see that these data runs display some features of instability over the full period
 650 of time, but stability over short time periods. For example, all the data with run
 651 numbers below about 51610 show significantly higher event yield than the runs after
 652 that run (possibly due to beam-target misalignment as indicated by raster magnet
 653 ADC values in Fig 3.25.

654 Likewise, the stability of the polarized count differences in the elastic region (0.9
 655 GeV $< W <$ 1.0 GeV) as well as separately in the delta (Δ) resonance region were
 656 studied by plotting them versus the same run numbers (here the elastic and Δ -
 657 resonance regions are considered separately, because the spin asymmetries in these
 658 two regions have opposite signs, which would have decreased the observed difference
 659 if combined. To further enhance the sensitivity of the observation, the difference of
 660 the count differences measured in the elastic and Δ -resonance regions as given by

$$\Delta N_{elastic} - \Delta N_{\Delta-res} = \frac{1}{P_b P_t} \left[\left(\frac{N^+}{FC^+} - \frac{N^-}{FC^-} \right)_{elastic} - \left(\frac{N^+}{FC^+} - \frac{N^-}{FC^-} \right)_{\Delta} \right] \quad (3.3)$$

661 were plotted (see Fig. 3.24). It was observed that this elastic normalized count
 662 difference (which is what really matters to our analysis, in the end) was much more
 663 stable than the total yield.

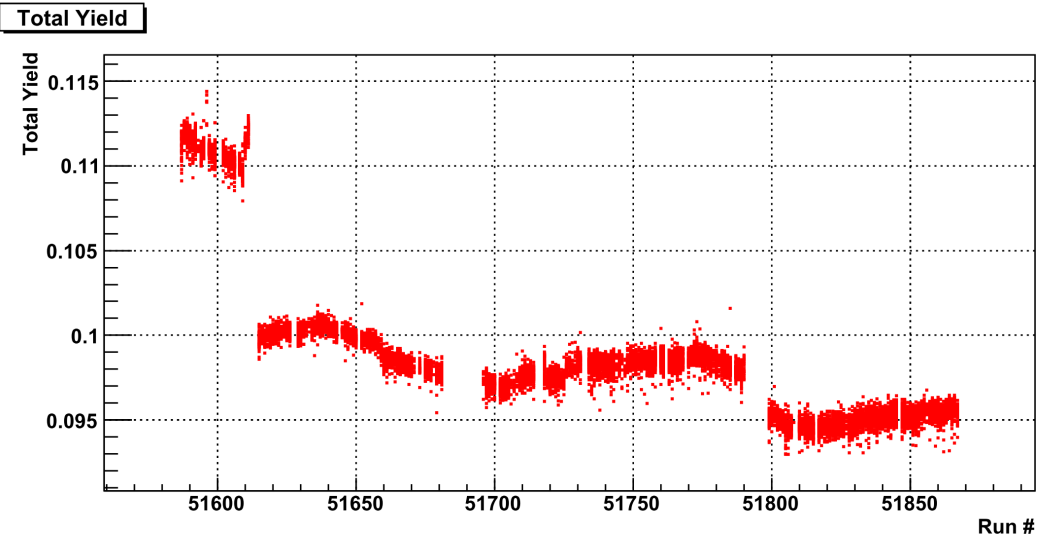


FIG. 3.23. Total normalized yield ($= \frac{N^+ + N^-}{FC^+ + FC^-}$) for 2.0 GeV ND₃ runs.

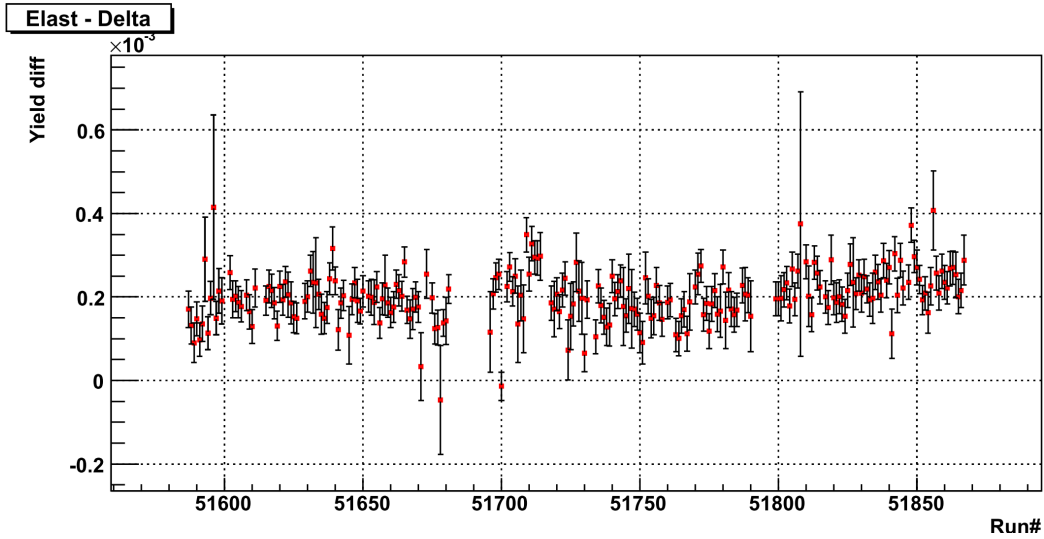


FIG. 3.24. Polarized yield differences (Eq. 3.3) normalized with $P_b P_t$ and BPM/F-cup for elastic peak minus that for the Δ peak for the 2.0 GeV ND₃ runs.

664 The same was also repeated for the other variables such as the root-mean-square
 665 of the ADC values (see Fig. 3.25) which carry information on the X and Y coordinates
 666 of the beam at the interaction vertex, thus their plots giving us somewhat more direct
 667 information on whether there was any misalignment between the beam and the target.

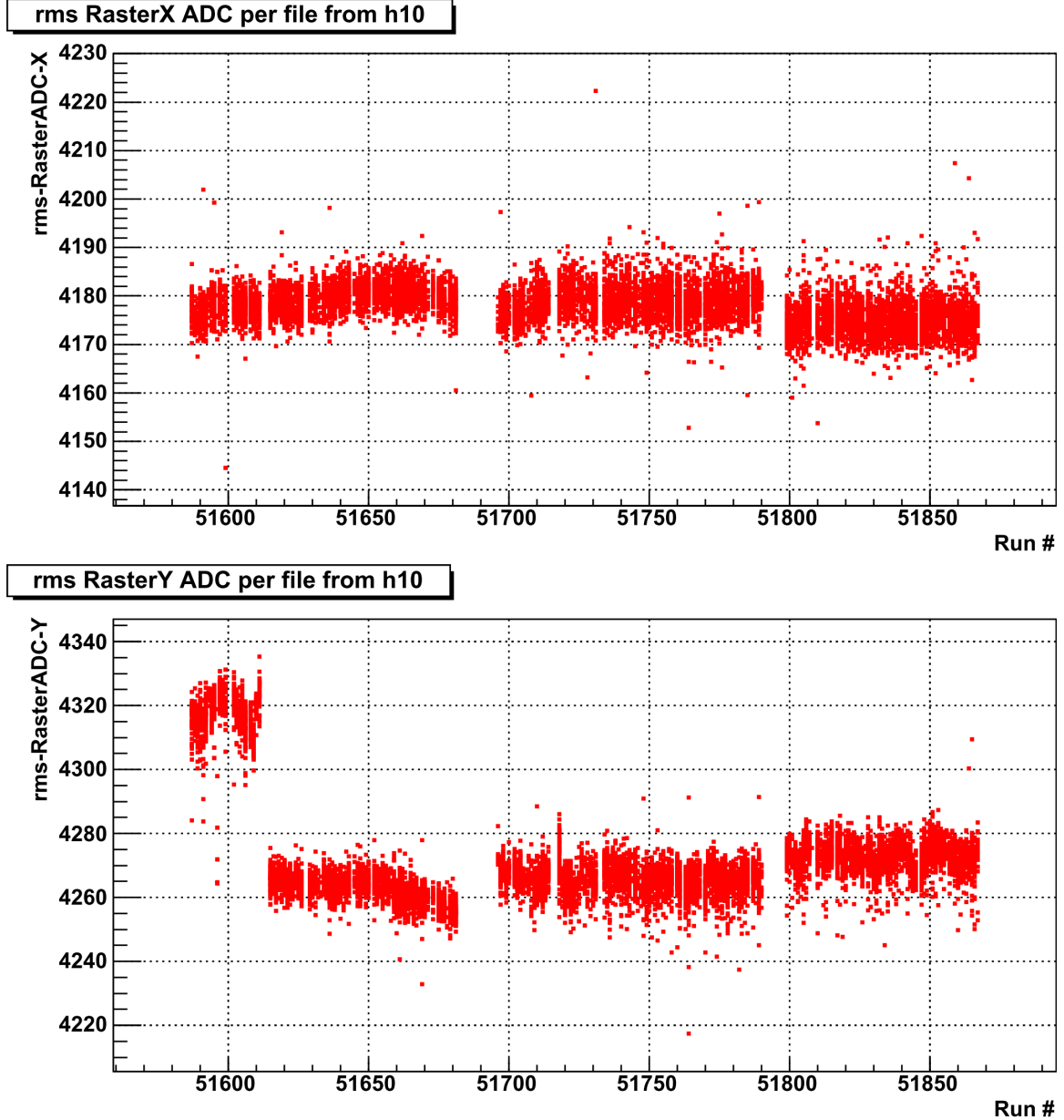


FIG. 3.25. Root-mean-square of the ADC values for the raster magnet currents in the directions X and Y. The distributions show a larger raster size in the y-direction for the first group of runs, indicating that the beam may have been hitting the edges and the walls of the target or other more dense structure support materials, thus explaining the higher total yield for the corresponding runs as shown by the Fig. 3.23. This does not affect our final analysis because these off-target materials are not polarized and, hence, do not contribute to the polarization dependent count difference (ΔN) used in the final analysis.

668 Based on the studies of these quality and stability plots, the data runs were di-
669 vided into subgroups with each beam energy data set. In each subgroup, the data
670 showed more stability than over the whole run period for the given beam energy.
671 For example, in case of the 2.0 GeV deuteron data, the runs were divided into four
672 distinct sub groups corresponding to the four separate bands as seen in the Fig. 3.23.
673 These subgroups were later treated and analyzed separately to get the corresponding
674 normalized polarized count differences (with all data runs from each subgroup com-
675 bined together). After the initial combination within the subgroups, they were again
676 combined into the grand total by properly considering the half-wave-plate status, and
677 the target polarization directions.

678 **3.5 Kinematic Corrections**

679 The reconstructed event vertices and associated particle 4-momenta are slightly off
680 from their true values for several reasons. First, RECSIS does not take into account
681 the fact that the beam is rastered in polarized target experiments. Next, any imper-
682 fections and mis-alignments of detectors and other components of the experimental
683 set-up are not accounted for. Furthermore, the torus field map is not known precisely.
684 In addition, the effects of multiple-scattering and particle energy losses are not con-
685 sidered in RECSIS. Therefore, to get more accurate results from the data analysis, the
686 data quality must be improved by applying various kinematic corrections. Following
687 is the list of the corrections that were applied for the analysis:

- 688 1. Incoming (beam) energy loss correction (due to ionization)
- 689 2. Tracking corrections
- 690 3. Drift chamber dependent momentum correction
- 691 4. Outgoing energy loss correction (due to ionization after scattering)

692 **3.5.1 Incoming Energy Loss Correction**

693 The first correction listed above considers the loss of beam energy due to atomic
694 collisions before the actual nuclear scattering takes place. A good estimate for this
695 loss is 2 MeV on average [26, 27], which is subtracted from the nominal beam energy.
696 This correction is applied during the analysis whenever the beam energy is involved⁵,
697 and therefore it is not included in the correction package described below.

⁵The beam energies that we used were derived from the Hall A and Hall C Tiefenback energies or the MDSY1c or MDSY3c energies[28]

698 **3.5.2 Tracking Corrections**

699 This work is mostly based on the work documented in the EG1-DVCS-TN-004[29] , in
700 which a routine or method is developed to swim the particles through the field map of
701 the target magnet to the drift chambers in order to determine the particle angles and
702 position at the target, provided the direction cosines of the tracks at DC and the beam
703 position from the raster magnets are known. It is expected that the method improves
704 both the angular resolution and the reconstructed longitudinal vertex position. The
705 slightly modified version of the corresponding C/C++ routine is used with some of
706 the constants in the routine replaced by new parameters to be determined by the
707 method of **χ^2 -square minimization** using ep-elastic events. (Since this data set
708 didn't have enough e^+e^- pairs, we didn't use them in the minimization like in the
709 EG1DVCS.)

710 **Method**

711 First of all, in order to convert raster magnet ADCs into corresponding beam positions
712 x_0 and y_0 , we need conversion parameters. These parameters are determined by using
713 a method outlined in EG1-DVCS-TN-002[30]. The method determines the values of
714 the slopes and offsets that convert the X- and Y-raster ADC readings to corresponding
715 beam positions x_0 and y_0 in cm by minimizing the sensitivity of target vertex position
716 (v_z) for charged tracks to beam motion.

717 Next, ep-elastic events are skimmed (from all of the NH_3 target data-set) using
718 electron ID cuts for the electrons (see section 3.3) in the sixth sector and proton ID
719 consisting mainly of the time-of-flight cuts are used to select protons in the third
720 sector (opposite to the sixth one). Then missing momentum cuts (less than 0.1 GeV
721 for each of the four components P_x , P_y , P_z and E) based on 4-momentum conservation
722 requirements (within measurement uncertainties) are used to help further clean up
723 the accidental coincidences. These skimmed events are saved in root files and later
724 reused for the minimization process described here.

725 The cuts used in the initial data skimming required that each of the four missing
726 components $(P_x, P_y, P_z, E)_{miss}$ be less than 0.1 GeV.

727 After that a correction routine involving a set of correction equations with several
728 unknown parameters are established. Then with the help of TMinuit (ROOT version
729 of Minuit), several sets of trial values are given to these unknown parameters and
730 the corresponding correction is applied to the particles in the skimmed events. For
731 each set of these trial values, a specifically defined χ^2 (see below) is evaluated looping
732 over all the skimmed events and the Minuit tries to find the optimum set of these
733 parameter values for which the χ^2 is minimum. Such an optimal set of values are
734 chosen as the correct values of these parameters and is used in the eventual correction

735 routine.

736 **The correction routine**

737 The routine uses 17 constants (free parameters determined by the above mentioned
738 process of χ^2 -minimization) and the following input and output variables:

- 739 • **Input variables:** x_r , y_r , $\text{cxd}\mathbf{c}$, $\text{cyd}\mathbf{c}$, xdc , ydc , zdc , p , q .

- 740 – x_r , y_r are x & y beam positions as returned by the raster correction routine
741 (see appendix)
- 742 – **cxd \mathbf{c}** , **cyd \mathbf{c}** are direction cosines of the track as measured at DC1
- 743 – **xdc**, **ydc**, **zdc** are the coordinates of the track measured at DC1
- 744 – p , q are the momentum and charge of the track

- 745 • **Output variables:** cxc , cyc , czc , vzc (all three corrected direction cosines and
746 the corrected Z-coordinate at the vertex) .

747 The sequence of calculation steps taken (inside the routine) to arrive at the output
748 results are as follows (where, I am also using the notations of P. Bosted i.e., subscripts
749 '0' used to indicate variables at vertex, subscript 'f' for those at the drift chambers
750 (these are the t1_ variables in the ntuples), and the values of (x, y, z) are in cm):

- 751 • First of all, get ready the following constants and variables:

- 752 – $f_c = \frac{B}{50} = 0.995$ is the overall field correction
- 753 * (i.e., the $B.dl$ correction factor. Our $B = 4.97T$, with B in kG f_c is
754 0.995)
- 755 – $\text{targsign} = 1$
- 756 – $\theta_f = \text{acos}(cz_{dc})$
- 757 – $\phi_f = \text{atan2}(cy_{dc}, cx_{dc})$

- 758 • Then, θ_f is corrected (for the misalignment of the DC) as follows:

- 759 – If it's the electron in the event,
- 760 * $\theta_f = \theta_f + (\text{par}[0] + \text{par}[1] \times \phi_f) \frac{\cos\theta_f}{\cos\phi_f} + (\text{par}[2] + \text{par}[3] \times \phi_f) \sin\theta_f$
- 761 – else if its the proton,
- 762 * $\theta_f = \theta_f + (\text{par}[4] + \text{par}[5] \times \phi_f)$

- 764 • Next, get ϕ_0 without raster corrections yet
 - 765 – $\phi_0 = \phi_f + \text{targsign} \times f_c (0.186 + \text{par}[10] + (0.045 + \text{par}[11]) \theta^2 + (0.008 +$
 - 766 $\text{par}[12]) \theta_f^3 + (0.0032 + \text{par}[13]) \theta_f^3/p^2) \frac{q}{p}$
- 767 • Correction to polar angle from focusing effect. First, get focusing term for beam
 - 768 (x,y)=0.
 - 769 – $\delta\theta = f_c (0.90 \theta_f + 1.2 \theta_f^3)/(100 p^2)$
- 770 • Displacement of beam along trajectory (x_p) and perpendicular to it (y_p)
 - 771 – $x_p = x_r \cos\phi_0 + y_r \sin\phi_0$
 - 772 – $y_p = -(x_r + \text{par}[6]) \sin\phi_0 + (y_r + \text{par}[7]) \cos\phi_0$
- 773 • Correction to $\delta\theta$ from radial target field, which only depends on raster x and y
 - 774 but not vertex z. Also, no effect on peak at zero!
 - 775 – $\delta\theta = \delta\theta (1. + \text{targsign} q p (0.5/\theta_f) (y_p/0.75))$
- 776 • Now can get cz
 - 777 – $\theta_0 = \theta_f + \delta\theta$
 - 778 – $cz_c = \cos\theta_0$
- 779 • Now ϕ_0 again, this time including raster correction
 - 780 – $\phi_0 = \phi_f + \text{targsign} f_c (0.186 + \text{par}[10] + (0.045 + \text{par}[11]) \theta^2 + (0.008 +$
 - 781 $\text{par}[12]) \theta_f^3 + (0.0032 + \text{par}[13]) \theta_f^3/p^2) \frac{q}{p} (1 - (0.09 + \text{par}[14]) \frac{0.35 - \text{par}[15]}{\theta_f} x_p)$
- 782 • Get cx and cy using this cz
 - 783 – $cx_c = \sin\theta_0 \cos\phi_0$
 - 784 – $cy_c = \sin\theta_0 \sin\phi_0$
- 785 • Renormalize czc
 - 786 – $cz_c = \sqrt{1.0 - cx_c^2 - cy_c^2}$
- 787 • **Apply target field rotation correction**

788 – $cx_c = cx_c - \text{targsign } q \text{ par}[8] cz_c/p$
 789 – $cy_c = cy_c + \text{targsign } q \text{ par}[9] cz_c/p$

790 • Renormalize again:

791 – $czc = \sqrt{1.0 - cx_c^2 - cy_c^2}$
 792 – $\theta_0 = \text{acos}(cz_c)$

793 • Get vertex z in cm

794 – $r_{dc} = \sqrt{(x_{dc} - x_r)^2 + (y_{dc} - y_r)^2}$
 795 – $Z_c = Z_{dc} - \frac{r_{dc} - (22 + \text{par}[16]) \cos\theta_0 (\tan\theta_0 - \tan\theta_f)}{\tan\theta_f}$

796 • Finally, the routine outputs (returns) the four corrected quantities

797 – $cx_c, cy_c, cz_c, Z_c.$

798 • Calculation of χ^2 (to be minimized)

799 The chi-square has different components as follows:

$$800 \quad \chi^2 = \chi_{Z\text{var}}^2(\mathbf{e}) + \chi_{Z\text{var}}^2(\mathbf{p}) + \chi_{E\text{var}}^2 + \chi_{\text{miss}}^2 + \chi_{P\text{pen}}^2 + \chi_{E\text{pen}}^2 + \chi_{Z\text{pen}}^2 + \chi_{\Delta E}^2$$

801 where,

802 • $\chi_{Z\text{var}}^2(\mathbf{e})$ and $\chi_{Z\text{var}}^2(\mathbf{p})$ are Z-variance contributions from electron and proton
 803 candidates in the ep-elastic events and are calculated as $\chi_{Z\text{var}}^2 = \frac{1}{N_{ep}-1} \left(\sum Z_c^2 - \frac{(\sum Z_c)^2}{N_{ep}} \right) / (0.05)^2$ separately for the electrons and protons. (Here, Z_c is the
 804 corrected Z of vertex and N_{ep} is the number ep-elastic events used in the mini-
 805 mization)

807 • $\chi_{E\text{var}}^2 = \frac{1}{N_{ep}-1} \left(\sum E_b^2 - \frac{(\sum E_b)^2}{N_{ep}} \right) / (0.005)^2$ is E_b -variance contribution. (Here,
 808 $E_b = M_p \left(\frac{1}{\tan(\theta_p)\tan(\theta_e/2)} - 1 \right)$ is the beam energy calculated after the angles are
 809 corrected by the correction routine.)

810 • $\chi_{\text{miss}}^2 = 100 \times \left(\frac{\sum p_x^2(\text{miss}) + \sum p_y^2(\text{miss})}{0.02^2} + \frac{\sum p_z^2(\text{miss}) + \sum E^2(\text{miss})}{0.05^2} \right)$ is missing four-
 811 momentum contribution. (Here, 100 is an arbitrary number to make the weight
 812 of this contribution comparable to others.)

- 813 • $\chi_{\text{Ppen}}^2 = \sum_{i=0}^{16} \frac{(par[i] - iPar[i])^2}{0.01^2}$ is the contribution due to runaway penalty on free
 814 parameters of the minimization. (Here, par[i] & iPar[i] are the current and
 815 initial values of the 'i'th parameter. In the first iteration, initial values were
 816 set to either zeros or the corresponding values as determined for EG1-DVCS by
 817 P. Bosted. In later iterations, they were set to the values determined from the
 818 previous iteration of the minimization.)
- 819 • $\chi_{\text{Zpen}}^2 = \sum_{e,p} \left(\sum_{N_{ep}} \frac{(Z_c - (-100.93))^2}{0.05^2} \right)$ is a penalty term when Z_c runs away from the
 820 known/nominal target center (-100.93 cm)
- 821 • $\chi_{\text{Epen}}^2 = \sum_{i=2}^4 \left(\frac{\sum_{N_{ep}} E_b}{N_{ep}} - E_0 \right)^2 / (0.005)^2$ is a penalty term to constrain E_b running
 822 away from the nominal values E_0 of beam energy.
- 823 • $\chi_{\Delta E}^2 = \left(\sum_{i=2}^4 \frac{\sum_{N_{ep}} (E_b - E_0)^2}{N_{ep}} \right) / (0.005)^2$ is another penalty term to constrain E_b run-
 824 ning away from the nominal values E_0 of beam energy.

825 **Minimization**

826 TMinuit is used to minimize the value of χ^2 as calculated above and, thereby, determine
 827 the values of the free parameters used in the correction routine. The minimization
 828 was done in such a way that the parameters were determined step by step - first
 829 deciding the first six parameters (keeping others fixed to initial values), then next
 830 two, then next two, then next four, then next 2 and finally the last one respectively.

831 **Tracking Correction Results**

832 With the method of χ^2 -minimization described above, the following set of values were
 833 determined for the 17 parameters from par[0] through par[16] respectively:
 834 -0.00165789, -0.00131314, -0.00643021, -0.00721441, -0.00775272, 0.00483673, 0.063387,
 835 -0.0615822, 0.00133127, 0.000839944, 0.0210091, -0.0363265, 0.00335536, 0.00104193,
 836 2.51519, -0.0313527, -1.29325
 837 As a result of the corrections with these newly determined parameter values,
 838 various quantities before and after the corrections looked as shown in the following
 839 figure:

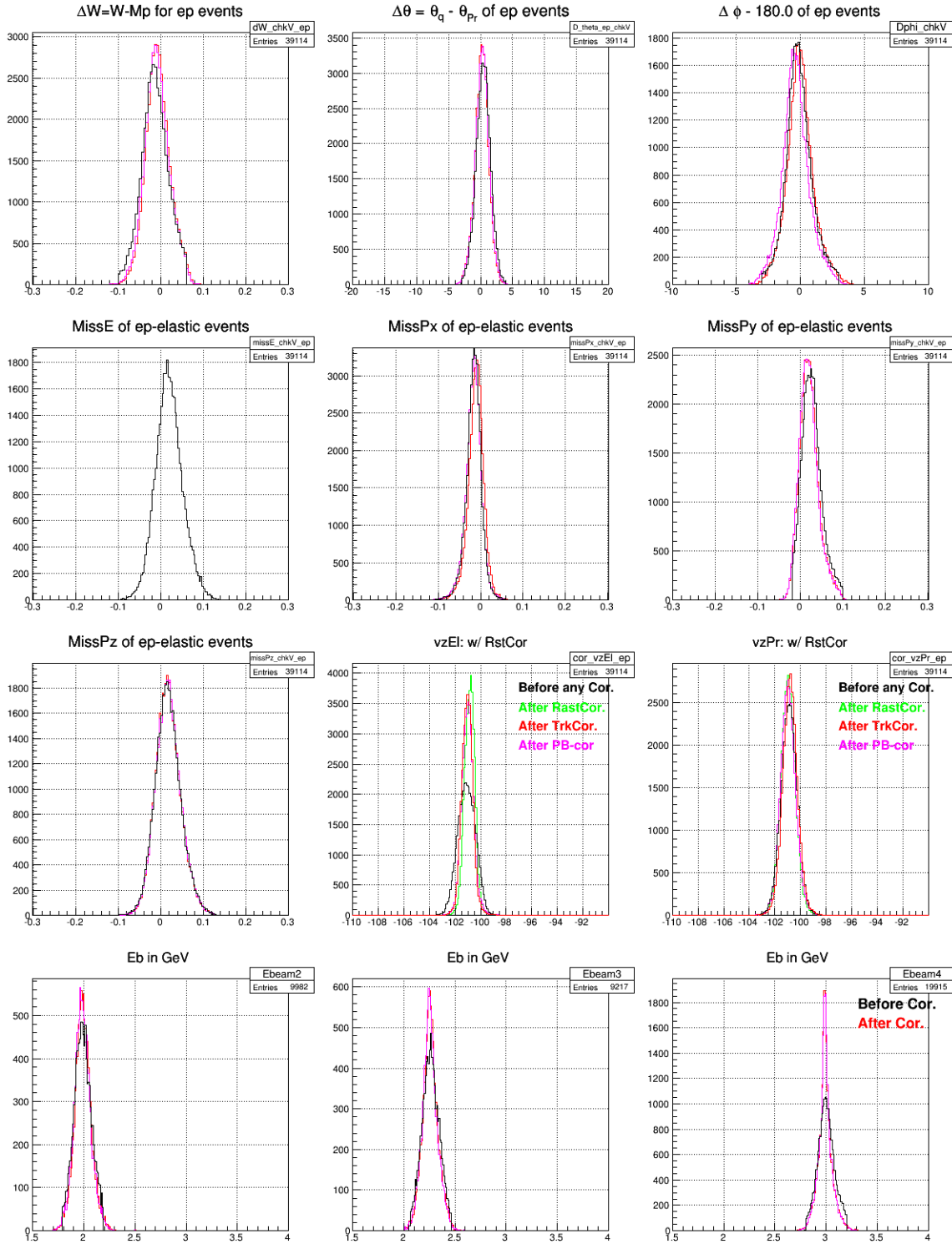


FIG. 3.26. Comparing various quantities before and after the tracking corrections which affects only the angles (and not the magnitude 'p') of the momentum.

840 **3.5.3 Momentum Correction**

841 Different DC related factors contribute to the biggest part of the systematic deviations
842 of particle momenta as reconstructed by RECSIS. The drift chambers could be
843 misaligned relative to their nominal positions or the survey results that is used by
844 RECSIS could be inaccurate or out-of-date. The effects of physical deformations (due
845 to thermal and stress distortions) of the chamber including wire-sag, incorrect wire
846 positions may not have been incorporated properly. The torus field map used by the
847 reconstruction software may not have been accurate and complete enough [31]. Ef-
848 fects on angles θ and ϕ due to these contributions are already factored in the tracking
849 correction described earlier. However, a separate method is developed to correct for
850 the effect on the magnitude p of the momentum. This p -correction methods picks up
851 and builds on some of the ideas outlined in the CLAS-NOTE 2003-005 [31].

852 **Procedure to determine the first 11 parameters**

853 The procedure involved dividing the covered kinematic space into a number of bins,
854 finding in them the magnitude of shifts of the inclusive elastic peaks w.r.t. the
855 expected position and use that to fit to a function to get an analytical expression for
856 the correction. The following angular bins were used:

- 857 • Six θ_{dc1} bins: (0,8),(8,10),(10,12),(12,15),(15,20),(20,30) degrees
858 • Five ϕ_{dc1} bins: (-10,-6),(-6,-2), (-2,2), (2,6), (6,10) degrees

859 where the angles used are the ones measured at the first drift chamber and ϕ_{dc1} is
860 measured w.r.t the sector mid-plane (thus the maximum range allowed is (-30.0,30.0)).

$$E'_{elastic} = \frac{E_{beam}}{1 + \frac{2E_{beam}}{M_p} \sin^2(\theta_e/2)} \quad (3.4)$$

861 In each of these kinematic bins, the quantity $\Delta E = E'_{elastic} - p$ (see Eq. 3.4) is
862 histogrammed for both NH₃ and ¹²C data separately. Next, the carbon histogram is
863 cross-normalized with the ammonia histogram (by comparing the two in the region left
864 to the quasi-elastic peak) and subtracted from the latter one to remove the nuclear
865 background. The difference gives histograms for the elastic events (as shown by
866 the dashed green histogram in Fig. 3.27). A Gaussian fit to the extracted elastic
867 histogram gives the position and width of the distribution. The offset or shift of
868 average position of the peak with respect to the expected $\Delta E = 0$ gives us the
869 needed correction on energy $E \approx p$ for the electron. This process is repeated for
870 all of the bins listed above and the corresponding ΔE offsets or the corrections are

871 determined for each of them. Additionally, ΔE distributions using ^{15}N nuclear mass
 872 in calculating $E'_{elastic}$ are also made and off-sets in the corresponding elastic peaks are
 873 also recorded whenever possible (particularly from the lower θ bins from low beam
 874 energy data where the nuclear-elastic and quasi-elastic peaks are well separated).
 875 Finally, these values of corrections for different average values of θ_{dc1} and ϕ_{dc1} are fit
 876 to Eq. 3.5 (which is based on similar work done for EG1b analysis[22]) and using the
 877 method of χ^2 -minimization in order to determine the values of the 11 fit parameters.

$$\frac{\Delta p}{p} = Pcorr1 + Pcorr2 + PatchCorr \quad (3.5)$$

878 where, $\frac{\Delta p}{p}$ is the ratio of the correction (Δp) to the magnitude (p) of the momentum
 879 and

$$Pcorr1 = \left((E + F\phi) \frac{\cos \theta}{\sin \phi} + (G + H\phi) \sin \theta \right) \frac{p}{qB_{torus}} \quad (3.6)$$

$$Pcorr2 = (J \cos \theta + K \sin \theta) + (M \cos \theta + N \sin \theta)\phi \quad (3.7)$$

$$PatchCorr = 0.02 \left(P + (Q + R \frac{\phi_{deg}}{30^\circ}) (\frac{10^\circ}{\theta_{deg}})^3 \right) \quad (3.8)$$

880 The quantity B_{tor} stands for $\int B_\perp dl$ along the track length multiplied by the speed
 881 of light in the units of m/ns ($c = 0.29979$ m/ns) and is given by

$$B_{tor} = 0.76 \frac{I_{tor} \sin^2(4\theta)}{3375\theta/rad} \quad \text{for } \theta < \frac{\pi}{8} \quad (3.9)$$

$$B_{tor} = 0.76 \frac{I_{tor}}{3375\theta/rad} \quad \text{for } \theta > \frac{\pi}{8} \quad (3.10)$$

882 In all these equations, sector number, θ , ϕ , θ_{deg} , and ϕ_{deg} come from the angle
 883 information measured at DC1. The direction cosine variables t11_cx, t11_cy, t11_cz
 884 (from pass1 ntuples) are used to derive these quantities. C++ standard functions
 885 acos() and atan2() are used to evaluate θ , ϕ (w.r.t the sector mid plane).

886 These total of eleven unknown parameters were determined by fitting above men-
 887 tioned momentum offsets (in combination with ionization energy loss correction for
 888 electrons (see Sec.3.5.4 below)) to the correction function given by the Eq. 3.5.

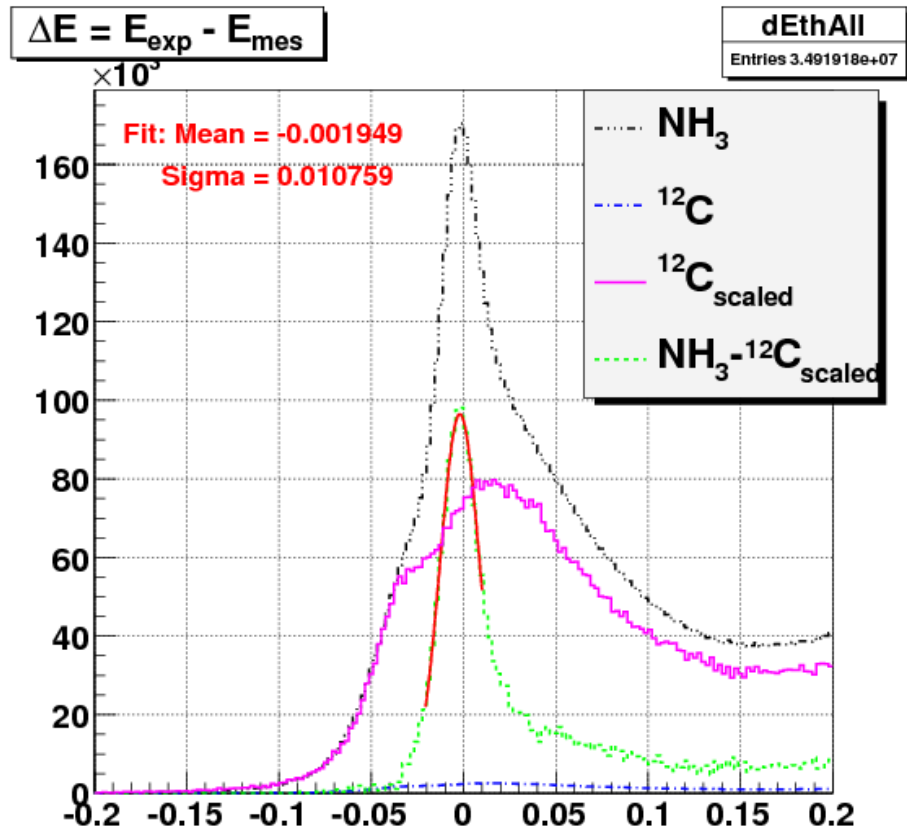


FIG. 3.27. Plots showing background removal from the ΔE counts from NH₃ (shown by “NH₃” line) data (by subtracting cross-normalized counts from ¹²C data (shown by “¹²C_{scaled}” line)) to separate the elastic peak (shown by “NH₃ - ¹²C_{scaled}” line) in one of the kinematic bins, thereby getting the momentum offset for that bin. The ¹²C data is used to account for the nuclear elastic background from ¹⁵N nuclei in the ammonia target. It would have been best to have data from ¹⁵N target itself but due to technical difficulties that was not possible and, therefore, ¹²C target was chosen as the closest possible approximation of ¹⁵N target.

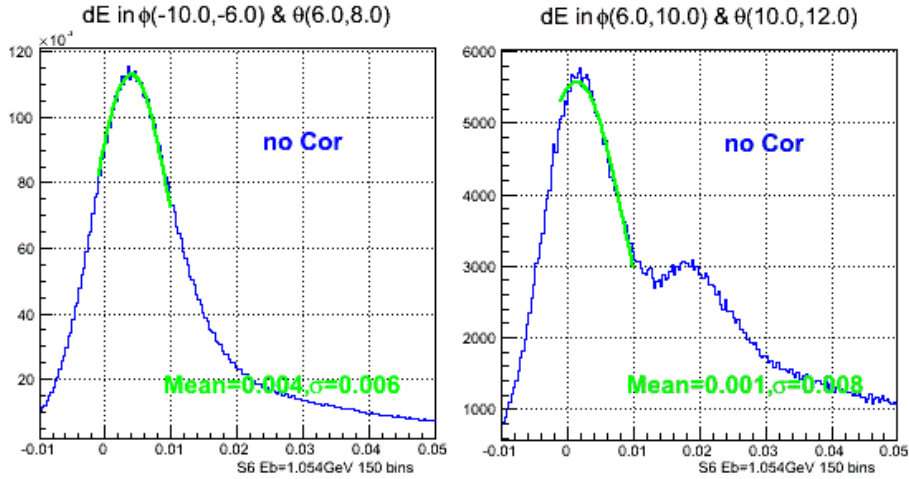


FIG. 3.28. Nuclear elastic peaks from ^{15}N target and the Gaussian fits in two of many kinematic bins as seen in $\Delta E = E'_{\text{elastic}} - p$ distributions from NH₃ data before the momentum corrections. In this case E'_{elastic} is evaluated using known mass of ^{15}N in Eq. 3.4. In the second plot, the proton elastic peak is also visible. Ideally, after all the corrections, the nuclear elastic peak is expected to be centered at zero. But, as is obvious from these figures, these peaks show offsets. These offsets (given by the mean values of the Gaussian fits) are collected from those bins in which the nuclear elastic peaks are very well separated (particularly the first few angular bins) and used in the χ^2 -minimization along with all the offsets of elastic peaks (see Fig. 3.27)

889 3.5.4 Outgoing Ionization Loss Correction

890 In addition to the corrections described above, the energy (E) of each of the particles
 891 is corrected for the outgoing ionization loss by adding an estimation of ionization loss
 892 as follows: $E_{\text{cor}} = E + \Delta E$ with $\Delta E = \frac{dE}{dX}\tau$ where the factor τ is the total effective
 893 mass thickness traversed by the particle and

$$dE/dX \approx 2.8 \text{ MeV}/(\text{g cm}^{-2}) \quad \text{for electrons} \quad (3.11a)$$

894 and, for hadrons [32]

$$dE/dX \approx 0.307 \times \frac{0.5}{\beta^2} \left(\ln \left(2.0 \times 511.0 \frac{\beta^2 \gamma^2}{0.090} \right) - \beta^2 \right) \text{ MeV} \quad (3.11b)$$

895 which is an approximation of the Bethe-Block formula [32]:

$$-\frac{1}{\rho} \frac{dE}{dx} = 4\pi N_a r_e^2 m_e c^2 \frac{Z}{A} \frac{1}{\beta^2} \left(\ln \left(\frac{2m_e c^2 \gamma^2 \beta^2}{I} \right) - \beta^2 \right) \quad (3.12)$$

896 The total effective mass thickness τ (in cm) is calculated as follows:

- 897 • $\tau = \tau_{\parallel} / \cos \theta$ if $\theta <= \pi/4$
 898 • $\tau = \tau_{\parallel} / \cos(\pi/4)$ if $\theta > \pi/4$

899 where τ_{\parallel} is calculated as:

- 900 • $\tau_{\parallel} = \Delta z \times 0.6 + 0.4$ if $\Delta z > 0.0$ and $\Delta z < 1.0$
 901 • $\tau_{\parallel} = 0.6 + 0.4$ if $\Delta z \geq 1.0$
 902 • $\tau_{\parallel} = 0.4$ if $\Delta z \leq 0.0$

903 with $\Delta z = z_{target_center} - z_{ave} + L_{target}/2 = (-101.0 \text{ cm} - z_{ave} + 0.5) \text{ cm}$ being the
 904 physical distance (along the target length) traveled by the particle through the polar-
 905 ized target material (e.g. the EG4 ND₃ target has length 1.0 cm and is positioned at
 906 $z = -101.0 \text{ cm}$). The factor 0.6 is the effective mass thickness of ND₃ (density of ND₃
 907 ($\sim 1 \text{ g/cm}^3$) multiplied by the packing fraction which is roughly 0.6 [33], whereas 0.4
 908 is the sum of the mass thicknesses of He (~ 0.3) and that of window foils (~ 0.1) [22].

909 Using the ionization loss corrected energy and the rest mass of the particle, mo-
 910 mentum is recalculated as $p_{cor} = \sqrt{E_{cor}^2 - m^2}$ (where m is the mass of the particle).
 911 Finally, this new p is used along with the previously corrected angles to evaluate the
 912 three cartesian components p_x , p_y and p_z of the momentum as follows:

$$\begin{aligned} p_x &= p \sin \theta \cos \phi \\ p_y &= p \sin \theta \sin \phi \\ p_z &= p \cos \theta \end{aligned} \quad (3.13)$$

913

914 3.6 Cerenkov Counter (CC) Efficiency

915 In the EG4 experiment, the Cherenkov Counter (CC) signal plays a major part in
 916 forming the event trigger for the data-acquisition system (DAQ). As stated earlier (see
 917 2.1), for the purpose of achieving low Q^2 measurements with high detector efficiency⁶,
 918 a new dedicated CC was designed and placed in the sixth sector. Even though the
 919 new CC was designed to have a very high and uniform detection efficiency, some
 920 variation occurs over the covered kinematic range and therefore the knowledge of
 921 the detector efficiency as a function of the kinematics is required by our method of
 922 absolute cross-section difference. Therefore, a study was done to determine the CC
 923 efficiency as follows.

⁶High detection efficiency is crucial for achieving smaller systematic uncertainties in the extracted physics quantities.

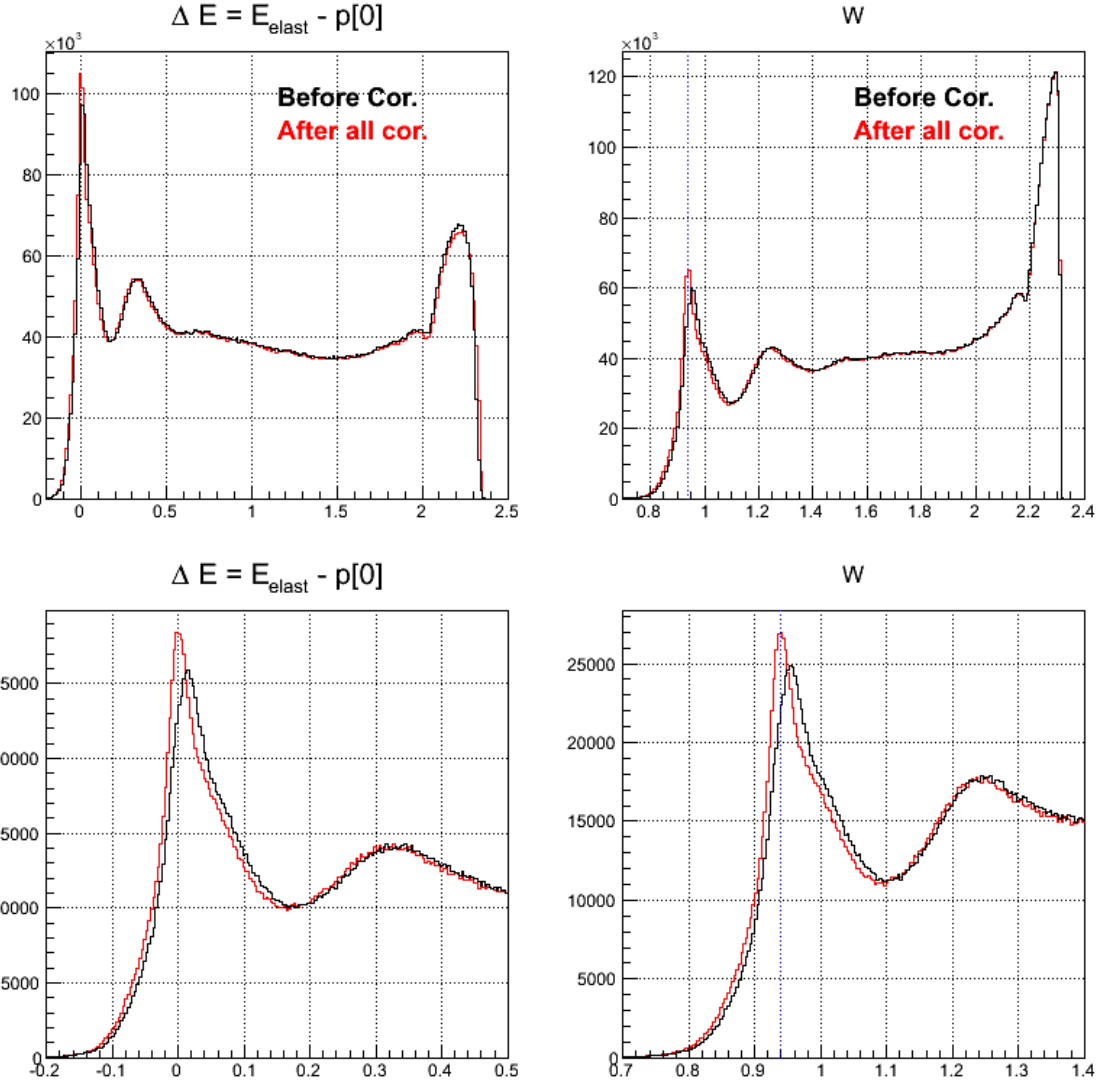


FIG. 3.29. Effects of kinematic corrections on inclusive events from 3 GeV NH₃ data. Here, distributions of ΔE and W are shown in two different ranges. The upper ones show the full range distributions, whereas the lower two show the distributions near the quasi-elastic peak. The distributions before the corrections are shown by **black continuous** lines and the ones after the corrections are shown by the **red** lines. Here, E_{elast} is the calculated or expected energy of the scattered electron assuming it was scattered off elastically, whereas, $p[0]$ is the momentum as measured by CLAS. From these plots it is evident that the momentum correction works as expected because the peak of ΔE is narrower and better centered at zero after the correction.

3.6.1 Procedure

The efficiency for some specific kinematic bin depends on the average number of photoelectrons produced by electrons in that bin which, in turn, is determined by the hit location on the Cerenkov PMT-projected plane as well as the angle with which the electron hits (or intersects) the plane. In the following, we describe how we determined the efficiency as a function of kinematic variables.

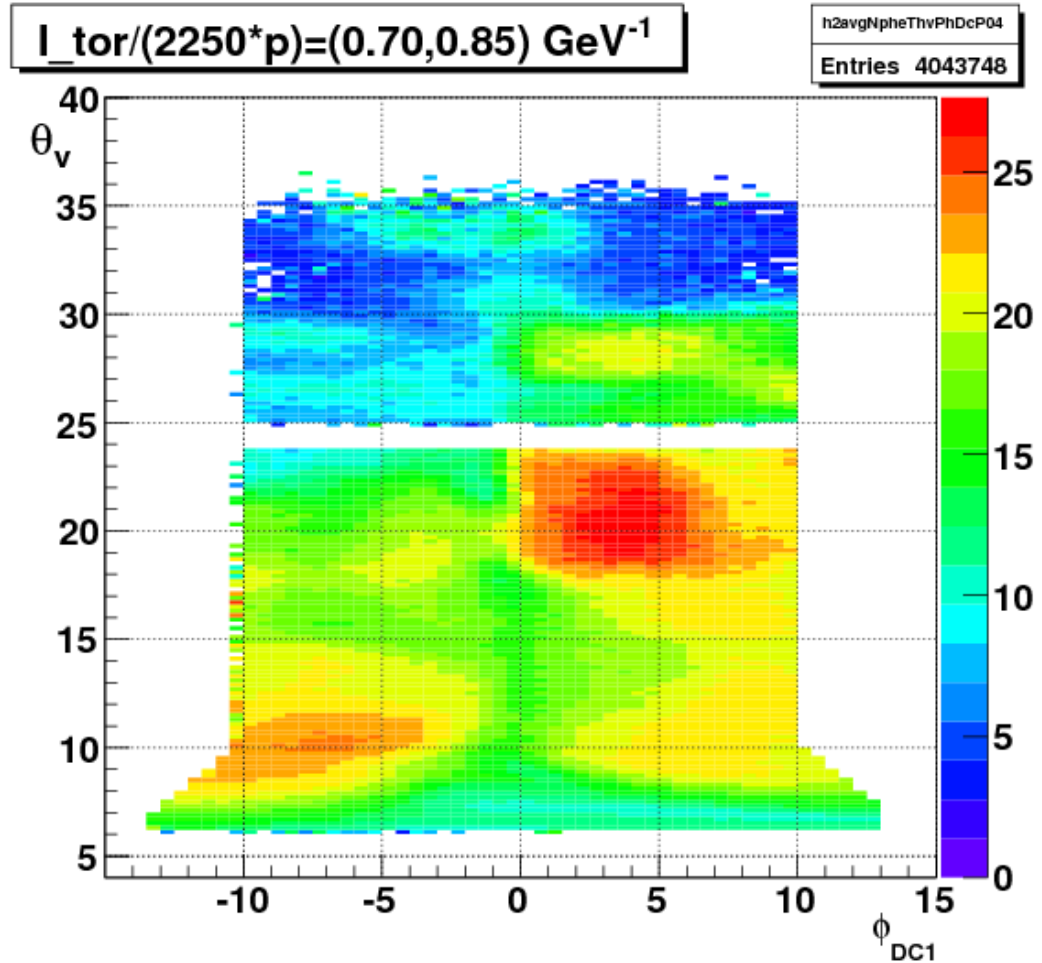


FIG. 3.30. Average photoelectron number (color-coded) produced in the 6th sector CC as a function of θ_{vtx} and ϕ_{DC1} in the second bin of the variable $ip = (I_{tor}/2250)/p$ (from the 2.3 GeV NH₃ data).

1. First, we define a torus-current normalized inverse-momentum variable $ip = (I_{tor}/2250)/p$ (see above), and divide the whole kinematic space into 12 bins in

932 “ip” as follows: (0.3, 0.4, 0.5, 0.6, 0.7, 0.85, 1.0, 1.25, 1.5, 1.75, 2.0, 2.25, 2.53).
 933 (For example, a 0.5 GeV electron during a 2 GeV run, which used 2250 A for
 934 torus current, would have $ip = 2.0 \text{ GeV}^{-1}$)

- 935 2. Next, for each bin in “ip”, a 2D map of the average number of photoelectrons
 936 is produced in a kinematic space defined by θ_{vtx} (scattering angle measured at
 937 the event vertex) and ϕ_{DC1} (azimuthal angle as measured at DC1). For this
 938 step, some data from NH₃ production runs⁷ are used with the standard electron
 939 selection cuts. One of these average-nphe maps is shown in the Fig. 3.30.
- 940 3. Next, using the “EC-only-trigger” data runs, good electron candidates are se-
 941 lected using the same cuts as before but without any CC-related cuts. For
 942 each of the selected electrons, the expected number of photoelectrons in the
 943 CC is determined in a look-up from the above average N_{ph} -maps based on its
 944 momentum and angles. This expected N_{ph} is then histogrammed in two ways
 945 - one histogram for those electrons which either didn’t trigger CC or didn’t
 946 pass all of the CC related cuts and another histogram for all electrons. The
 947 ratio of these two histograms (shown in the top-right and top-left panels of
 948 Fig. 3.31 respectively) gives us the inefficiency of the CC-detector as a func-
 949 tion of N_{ph} (as shown in the bottom two panels of the same figure). (Errors
 950 in the inefficiencies have not been drawn (for the purpose of cleaning) in the
 951 figures but they were calculated using the fact that the error in a ratio N2/N1
 952 is $\sqrt{N2(1 - N2/N1)/N1}$).
- 953 4. The ideally expected CC intrinsic inefficiency is given by the Poisson distribu-
 954 tion, since we require more than 2 photoelectrons, the theoretical prediction
 955 for the inefficiency is actually $(1 + N_{ph} + 1/2 N_{ph}^2) * \exp(-N_{ph})$. However, we
 956 found empirically that if we calculate N_{ph} only with electrons that exceed the
 957 threshold of 2.5, then we find that the functional form is pretty close to the
 958 form $y = p_0 + p_1 \cdot \exp(-p_2 x)$, where x represents $\langle N_{ph} \rangle$, and y represents
 959 the inefficiency. This form was used to fit with the above measured inefficiency
 960 and the result of the fit is shown in Fig. 3.31. We find that the inefficiency
 961 agrees very well with the expectation at low nphe, but remains at a very small
 962 constant value of around 0.01 (we call it the “constant background”) at higher
 963 nphe.

⁷This method relies on the use of two different sets of data. One is the regular NH₃ target data and another is the “EC-only” data runs which were collected without using CC in the trigger. Since the latter type of data were collected with NH₃ as target, to be consistent, NH₃ production data was chosen rather than the ND₃ ones to make the N_{ph} -maps.

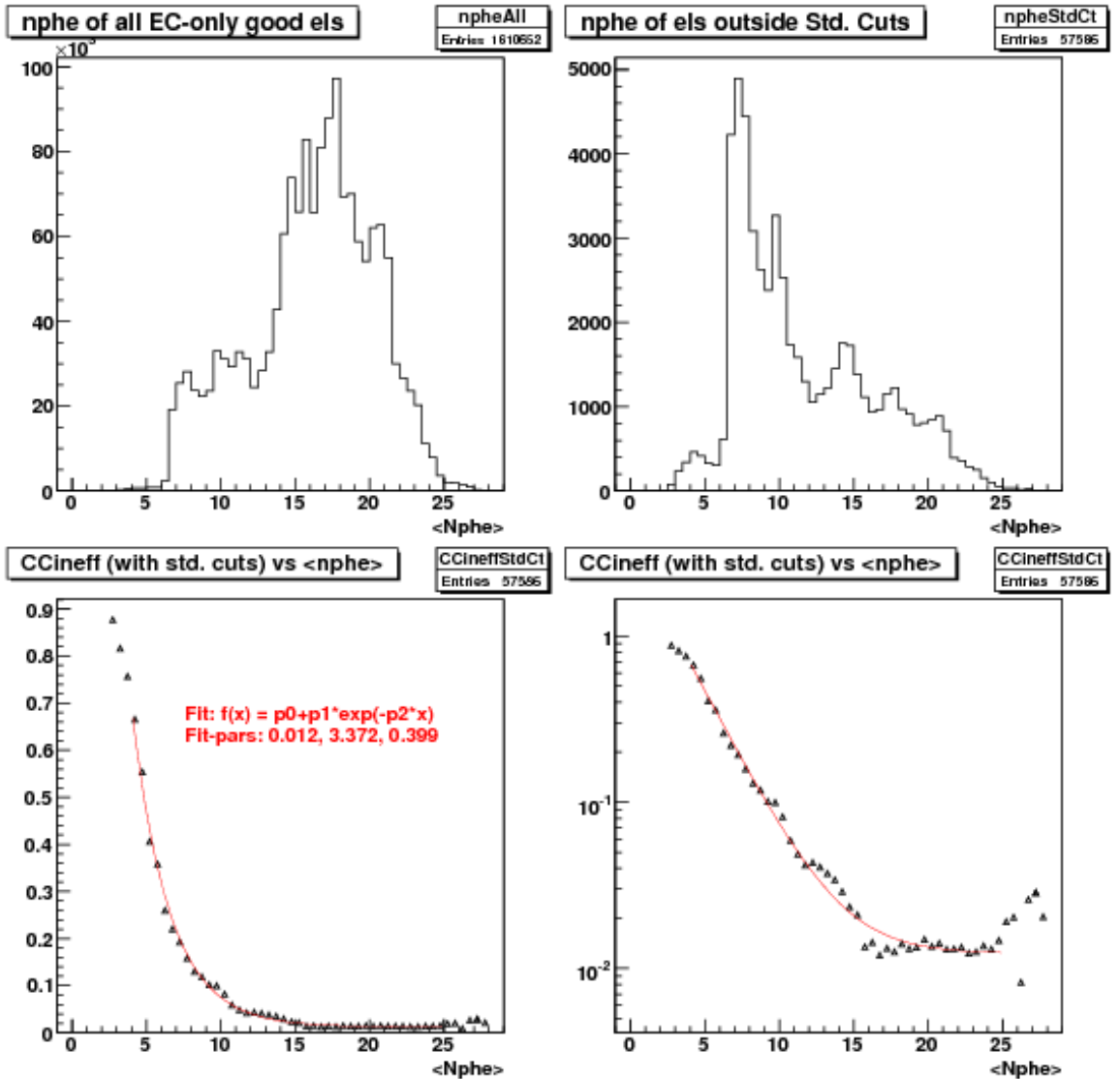


FIG. 3.31. EC detected good electrons (for all momenta) as a function of $\langle N_{ph} \rangle$ (top left). Similar distribution (top right) for those good electrons that were detected by the EC but were rejected by the standard set of event selection cuts which includes CC-dependent cuts. By dividing the latter with the former, one gets the calculated CC inefficiency. The bottom two plots show the inefficiency distribution and a fit (red continuous line) in both linear (in third panel) and logarithmic (fourth panel) scales. Looking at the first plot, it can be seen that most electrons are above $N_{ph} = 15$ where the inefficiency is at most 1-2 %.

964 5. Finally we use the inefficiency fit just developed to evaluate the corresponding
 965 efficiencies and transform the 2D map of N_{ph} into the corresponding efficiency

966 maps (see Fig. 3.32 for such a map in one momentum bin.). These maps are
 967 later used to apply the efficiency correction on an event by event basis in the
 968 simulation.

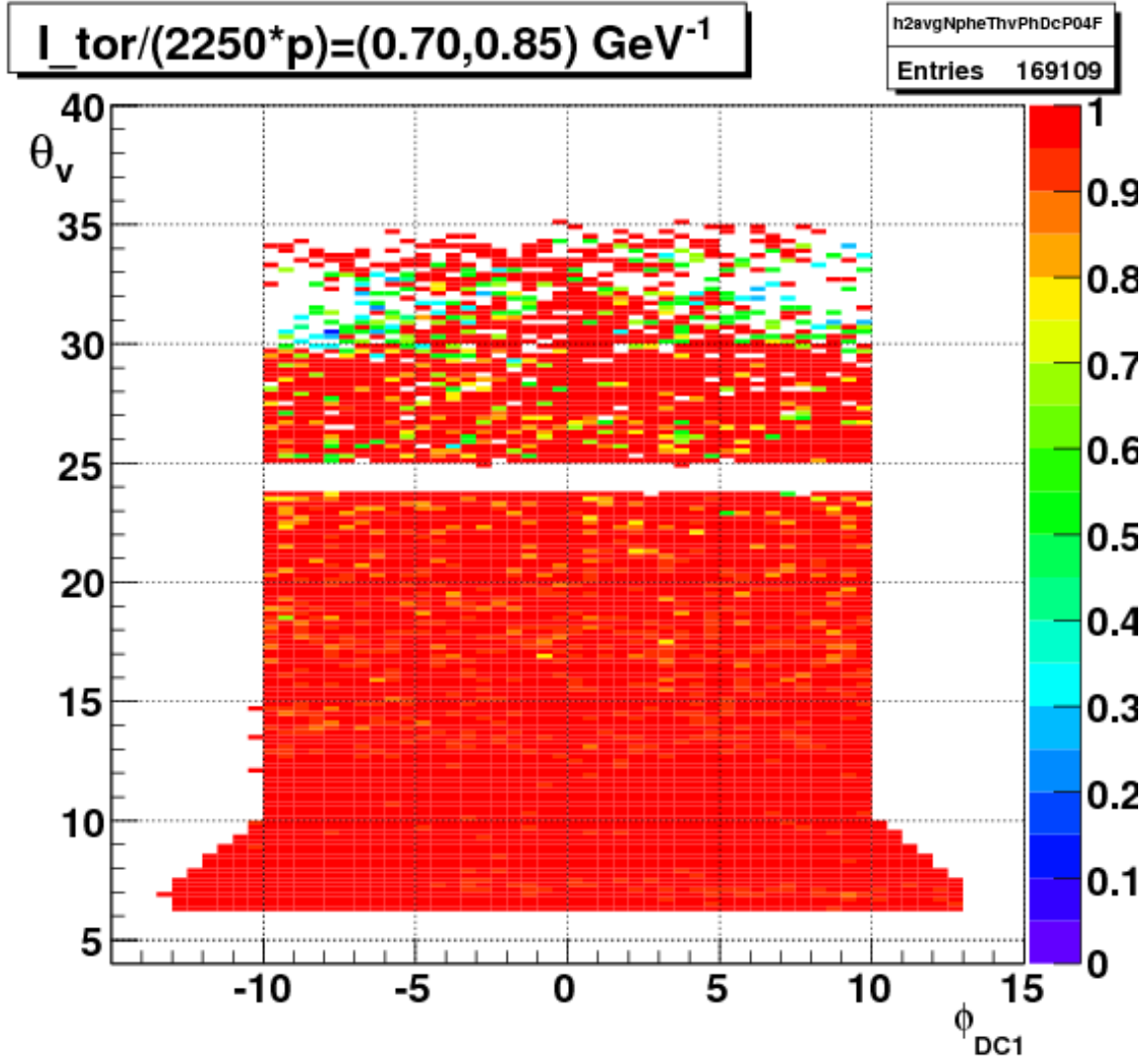


FIG. 3.32. CC-efficiency in a momentum bin .

969 From this study, we see that the CC is very efficient in most of the kinematic region
 970 (see Fig. 3.32). Once, the CC-(in)efficiency was estimated, we use the calculated CC
 971 efficiency to multiply our simulation (i.e., for each simulated event, we look up the
 972 CC efficiency and weigh the event with it.

973 3.7 Pion Contamination Corrections

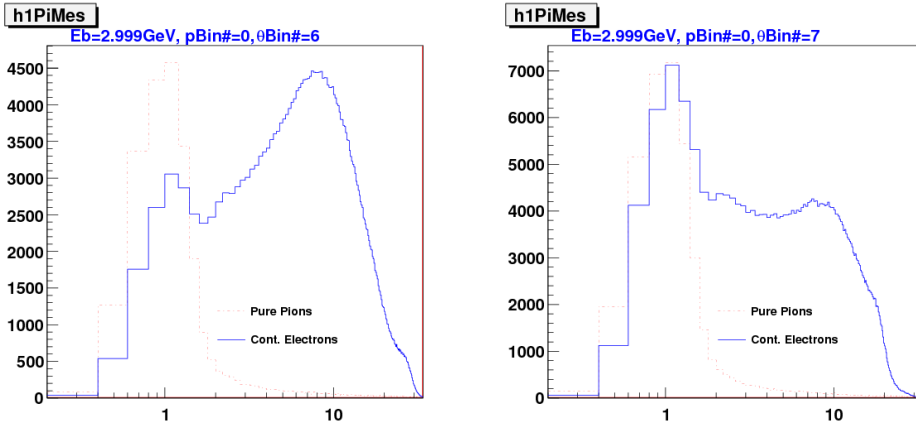
974 One of the two major sources of backgrounds in the measured EG4 electron rates
975 comes from misidentified negatively charged pions (π^-) that produce similar set of
976 signals as electrons in various detector components and thus pass the electron ID
977 cuts. In the EG4 experiment, signals from the electromagnetic calorimeter (EC) and
978 Cherenkov counter (CC) are used to identify electrons from pions, but even with
979 stringent conditions on these signals, some of the pions get misidentified as electrons.
980 To avoid limiting statistics too much in order to minimize the final statistical error
981 in a given kinematic bin, a trade-off in purity versus efficiency (statistics) is made by
982 quantifying the amount of this kind of contamination.

983 3.7.1 Method

984 First, the whole kinematic space covered by EG4 is divided into 90 two-dimensional
985 bins - 9 in p and 10 in θ^8 .

986 For each kinematic bin, a histogram of the number of photo-electrons (variable
987 ' N_{phe} ' in the data ntuple) produced by the electron candidates (selected using the
988 standard particle selection conditions (cuts) except that no cut on ' N_{phe} ' is included) is
989 made (see Fig. 3.33). Likewise, using a very stringent set of cuts, a similar histogram
990 is made for the cleanest possible sample of pion candidates in the same kinematic
991 bin.

8For 2 GeV or higher beam energy data sets, the p -bin boundaries are chosen as (0.30, 0.60, 0.90, 1.20, 1.50, 1.80, 2.20, 2.60, 3.00) and (0.30, 0.45, 0.60, 0.75, 0.9, 1.1, 1.4) for others. And, for θ , the boundaries are (5.0, 6.0, 7.0, 8.0, 9.0, 10.0, 12.0, 15.0, 19.0, 25, 49). The choice of the binning was rather arbitrary. Nevertheless higher statistics region was divided into relatively finer bins (event population peaks around $\theta = 10$ degrees).



(a) For the 1st p-bin and 7th θ -bin.

(b) For the 1st p-bin and 8th θ -bin.

FIG. 3.33. Number of photo-electrons produced in CC by clean pion and contaminated electron samples (3.0 GeV data)

- **Estimating the contamination in each bin:** A 7th order polynomial is fit to the N_{phe} histogram for electrons in the N_{phe} range extending from $N_{phe} = 1.8$ to $N_{phe}=10$. The fit is then extrapolated down to $N_{phe} = 0$ (see Fig. 3.34). Subtracting the extrapolated fit from the impure electron distribution results in the extraction of the contaminating pion peak⁹. Rescaling the pure pion sample to the extracted peak gives us the distribution of the actual pion contamination over the complete range of N_{phe} . Finally, the counts corresponding to this rescaled pure sample in the region above the standard cut $N_{phe} > 2.5$ is calculated. Then the ratio of this count to the impure electron count in the same standard N_{phe} range gives the measured contamination for the bin.
- The contaminations thus evaluated for different momentum bins belonging to a particular θ -bin are then plotted against the corresponding momenta. Then, this is fit to an exponential function.
- The parameters par1 and par2 of the exponential fit performed in different theta bins are next graphed together to see the presumed linear dependence.
- Finally, a global fit is performed on all the contaminations in different θ - and p- bins (not on the fit parameters). The fit parameters from the earlier two fits

⁹Beyond $N_{phe} = 1.8$, the electron sample is nearly pure except for a tiny fraction due to the pion tail, so any function that fits that section of the N_{phe} -distribution is supposed to represent the pure electron distribution. In order to simplify the situation, we chose to fit only from 1.8 to 7.0 rather than covering the full range beyond 7.0.

1009 only give us a hint to the type of the dependence, thus allowing us decide the
1010 form of the fit function.

1011 From the study, it is found that the typically pion contamination is less than 1
1012 %.

1013 **3.8 e^+e^- -Pair Symmetric Contamination Corrections**

1014

1015 The next major source of background is the secondary electrons from various e^+e^- pair
1016 production processes. When an electron originating from such a pair passes through
1017 the detector, the detector has no way to distinguish it from the electrons that actually
1018 scattered off the target. Therefore, the detector simply accepts it as a true scattered
1019 electron candidate, thus producing a contamination that has to be estimated and
1020 corrected for. The first such source is the wide-angle e^+e^- pair production from
1021 bremsstrahlung photons generated in the target. The other major source is hadron
1022 decay such as the Dalitz decay ($\pi^0 \rightarrow e^+e^-\gamma$), $\pi^0 \rightarrow \gamma\gamma$ and then conversion of these
1023 photons into e^+e^- pairs. Likewise, the pseudoscalar particle η , and the vector mesons
1024 ρ , ω , ϕ also decay to e^+e^- , but they are not major contributors because of their very
1025 small decay probabilities as well as the small population compared to the π^0 and
1026 photons. Of all these sources, the biggest contributor to the secondary electrons is
1027 the $\pi^0 \rightarrow \gamma\gamma$ with γ conversion to e^+e^- [34].

1028 The amount of contamination from this type of process can be estimated by
1029 monitoring the amount of positrons that were recorded under the same experimental
1030 and kinematic conditions. Because of the symmetry in the amount of electrons and
1031 positrons produced from these sources, the positron to electron ratio gives us the
1032 amount of the pair-symmetric contamination. However, due to the presence of the
1033 strong magnetic field inside the detector and the fact that the positrons have opposite
1034 charges, their detector acceptance would be different in a given setting. By reversing
1035 the magnetic field while keeping everything else the same, it is possible to estimate
1036 the contamination. For some of the beam energies used for the NH₃ data of the EG4
1037 experiment, some data were collected with identical experimental setting but with
1038 the torus field reversed. The data from those runs were used to estimate the amount
1039 of positrons in somewhat the same fashion as pion contamination. For example, Fig.
1040 3.35 shows one estimate (both data points and the fit) of the contamination in EG4
1041 compared with those determined for the EG1b experiment [22].

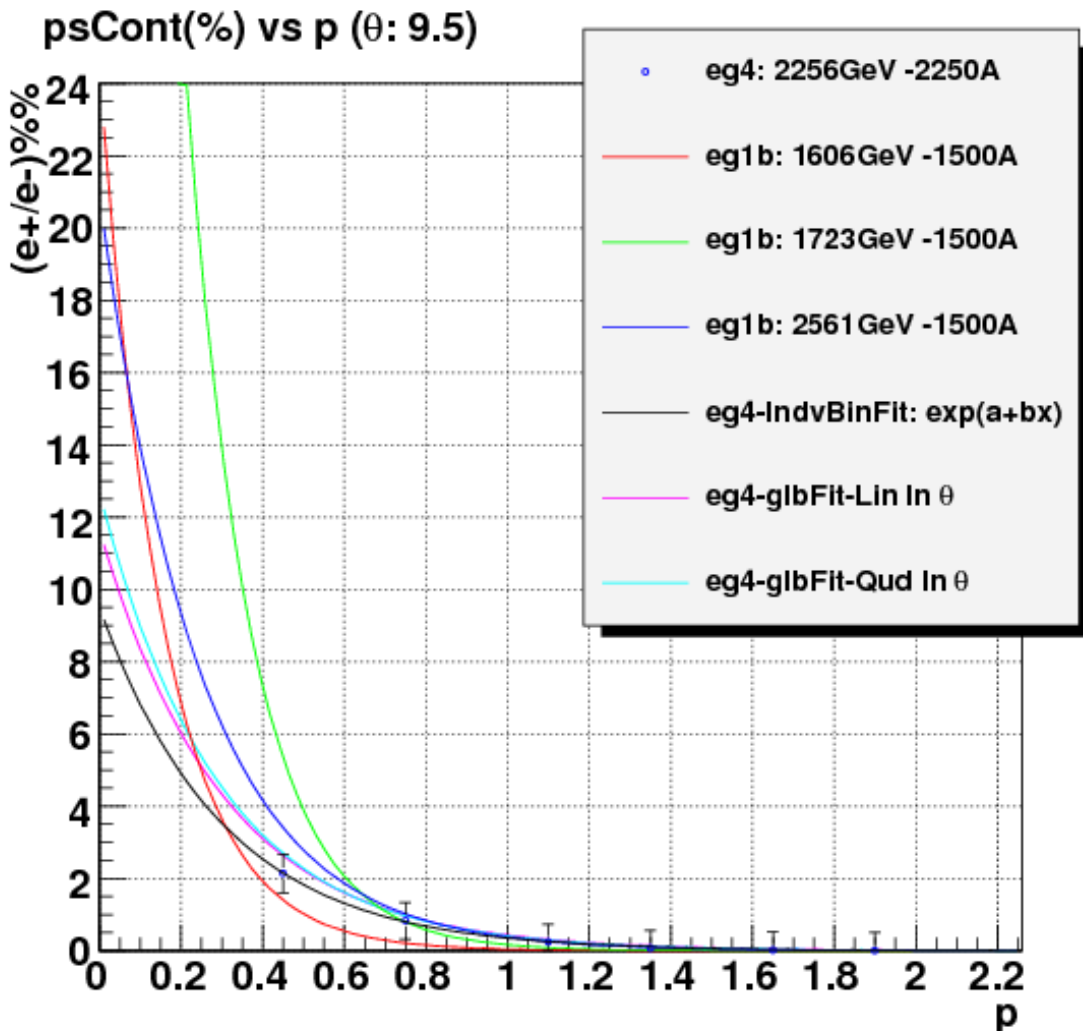


FIG. 3.35. Pair-symmetric contamination Fits (%) as a function of electron momentum.

1042 For this analysis, both the pion and e^+e^- pair symmetric contaminations are small
 1043 enough to be ignored. This leads to only a slight increase in the systematic error in
 1044 the final physics results.

1045 **3.9 Study of NH₃ Contamination of EG4 ND₃ Tar-
1046 get**

1047 In equation (3.1), it is assumed that the ammonia target is 100% pure i.e. composed of
1048 only ¹⁵ND₃ molecules and that the contribution from the slightly polarized nitrogen
1049 is negligible. But, in practice, the standard ND₃ sample is not a 100% pure material.
1050 Rather, it contains one or two percent of ¹⁴ND₃, ¹⁵NH₃ [35], and some traces of
1051 other isotopic species of ammonia. It was reported by the EG1-DVCS experiment
1052 at Jlab [36][37] that a higher than usual amount of NH₃ (about 10%) was observed
1053 in the ND₃ target, indicating that an inadvertent mix-up of NH₃ and ND₃ materials
1054 could have happened during the experimental run. Wondering if the EG4 experiment
1055 had a similar incident, we decided to investigate and estimate the amount of NH₃
1056 contamination of our ND₃ target by looking at the data from the ND₃ run period of
1057 the experiment as described below.

1058 **3.9.1 Procedure**

1059 The method involves using ep elastic (or quasi-elastic in the case of non-proton target)
1060 events and comparing the width in some quantity that reflects the correlation between
1061 the scattered electron (e) and the recoiling proton (p) due to the kinematic constraints
1062 of such events. The most suitable correlation is the one between the polar angles of
1063 the electron and the proton. That is because of the better angular resolution in CLAS
1064 than that for momentum, and also due to the fact that polar angle (θ) resolution is
1065 much better than that of the azimuthal angle (ϕ) because of the rotational effect (on
1066 ϕ) of the polarized target field as well as the drift chamber resolutions [36].

The θ -correlation can be studied mainly in two ways. The first way is to reconstruct and histogram the beam energy using the measured polar angles and the known target mass and then compare the histogram from the ND₃ target run with that from a pure NH₃ target run. The other equivalent way is to predict the proton polar angles (using the measured electron angles, known target mass and the beam energy) and then histogram the deviation of the measured proton angles from the expected values. We chose to use a slightly modified version of the latter approach in which we histogram the following quantity¹⁰:

$$\Delta = p_p \cdot (\sin \theta_q - \sin \theta_p) \quad (3.14)$$

where p_p is the measured proton momentum, θ_p is the measured polar angle of the proton, and θ_q is the expected polar angle of the recoiling proton (which is also the

¹⁰We chose this quantity Δ rather than the simple angle difference ($\theta_q - \theta_p$) because the former is more directly interpretable in terms of transverse missing momentum for the case of quasi-elastic scattering.

angle of the exchanged virtual photon (q) given by:

$$\theta_q = \tan^{-1} \left(\frac{M_p}{\tan(\theta/2) \cdot (E_{beam} + M_p)} \right) \quad (3.15)$$

The method exploits the fact that the width of the quantity Δ from data with deuteron target decreases because the Fermi motion of the protons in the deuteron nuclei gives a spread of the order of 50 MeV in transverse momentum, and for longitudinal particle momenta of order of a few GeV, we obtain a polar angle spread about 20 mr, which is much larger than the intrinsic CLAS resolution of about 2 mr.

3.9.2 Event Selection

First, for each data set (corresponding either to NH_3 , ND_3 or ^{12}C runs), using standard electron and proton identification cuts , events with a well reconstructed scattered electron and a similarly well reconstructed candidate for proton are selected. We accept only events each of which have one electron, one proton and at most one neutral particle candidate (expected to be a neutron coming off from the deuteron target break-up). If the event is of the above type, the following additional cuts are applied to make sure it is elastic or quasi-elastic event:

- $E_X < 0.15 \text{ GeV}$ with $E_X = M_p + E_e - E_{e'} - E_p = M_p + \nu - E_p$
- $P_X < 0.5 \text{ GeV/c}$ with $\vec{P}_X = \vec{0}_p + \vec{P}_e - \vec{P}_{e'} - \vec{P}_{p'} = \vec{P}_e - \vec{P}_{e'} - \vec{P}_{p'}$
- $0.88\text{GeV} < M_X < 1.04\text{GeV}$
- $\theta_q < 49.0^\circ$
- $|\phi_e - \phi_p| - 180.0^\circ | < 2.0^\circ$

where X indicates the missing entity in the $d(e,e'p)X$ channel, which is expected to be neutron in the case of the quasi-elastic channel, thus E_X is the missing energy and SO ON.

If it passes these cuts, the quantity Δ in Eq. 3.14 is calculated for the event and then histogrammed as shown by the red curves in the top-left (from ^{12}C runs), top-right (from NH_3 runs), and bottom-right (from ND_3 runs) panels of Fig. 3.36.

After getting the histograms for the quantity Δ for the ep-elastic or quasi-elastic events from the NH_3 , ND_3 and ^{12}C target data sets, we first remove the contribution from the non-hydrogen component of NH_3 and ND_3 targets by subtracting the corresponding carbon histogram (properly scaled to match with the left-shoulders (mainly from the nuclear elastic background in each of the ammonia data)). Since the carbon

1096 data is too low in counts (hence the raggedness in the histogram), a fit (a 'gaussian'
1097 times a 'linear' function) to the carbon data is obtained, and that fit (shown as the
1098 blue line in the first panel in Fig. 3.36 is used instead of the histogram itself to
1099 remove the background. The blue line in the second (top-right) panel and the cyan
1100 line in the last (bottom-right) panel show the properly scaled carbon fits which are
1101 subtracted from the NH₃ and ND₃ histograms (shown by red lines) respectively. After
1102 the subtraction, we get new histograms that represent 'pure' elastic or quasi-elastic
1103 data from protons and deuterons (shown by the magenta lines in the third and last
1104 panels respectively).

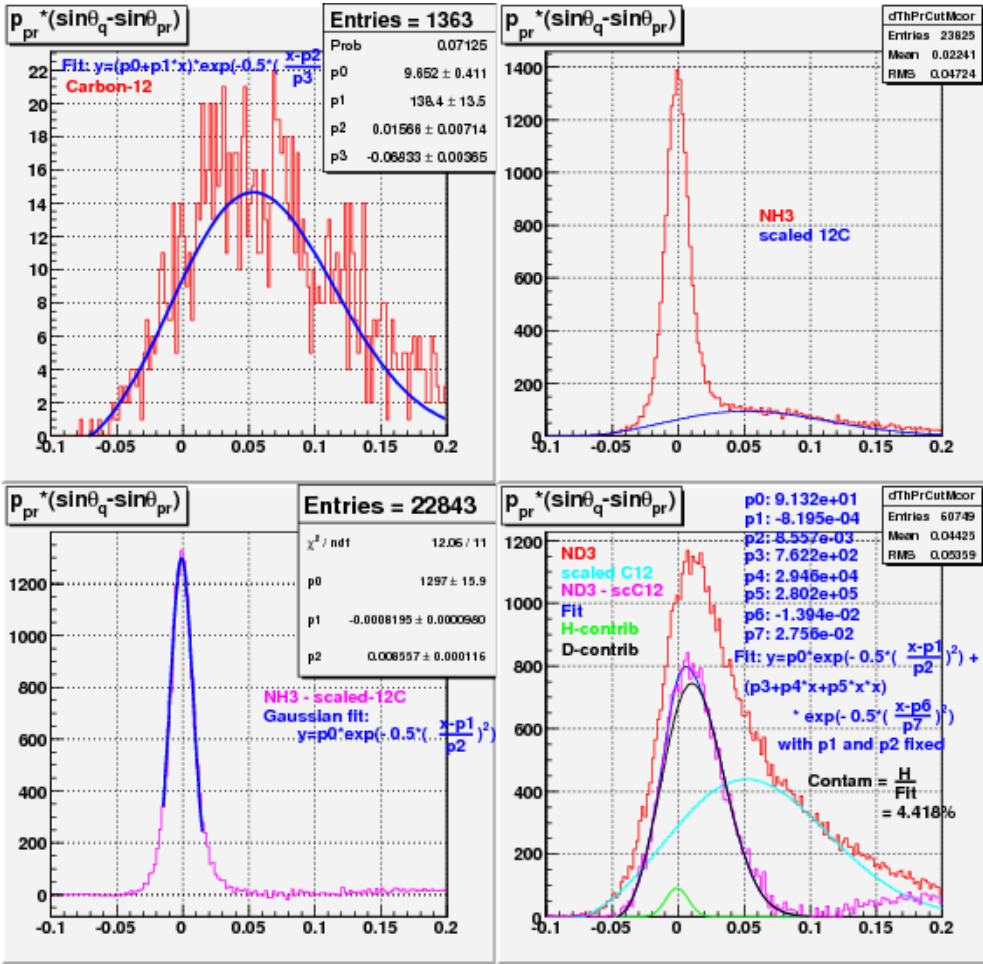


FIG. 3.36. Histograms showing the quantity $\Delta = p_p \cdot (\sin \theta_q - \sin \theta_p)$ for elastic or quasi-elastic events from carbon-12 (top-left), NH₃ (top-right) and ND₃ (bottom-right) target runs respectively. The third (bottom-left) panel shows the background removed elastic events from the NH₃ data. In the fourth panel, various Δ are shown - red is the raw ND₃, light green is the scaled-¹²C for the nuclear background, brown is for the difference between the two.

1105 3.9.3 Extracting the Contamination

1106 After we have the 'pure' elastic or quasi-elastic data from NH₃ and ND₃ runs, we get
 1107 the mean and the spread (standard deviation σ) of the proton elastic peak by fitting
 1108 the NH₃ data to a Gaussian function $f_p(x)$ (the blue line in the third panel with
 1109 parameters p0=height, p1=mean and p2= σ). After we have the fit for the proton
 1110 elastic peak, we fit the background subtracted deuteron data to a function f(x) that

1111 is a linear combination of the pure proton fit and a pure deuteron fit (the latter with
1112 the form of **a quadratic function \times a Gaussian**¹¹) as follows:

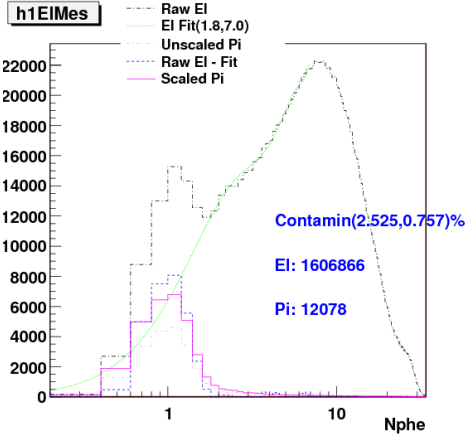
$$f(x) = p_0 \cdot f_p(x) + (p_1 + p_2 \cdot x + p_3 \cdot x^2) \cdot e^{-0.5 \cdot \left(\frac{x-p_4}{p_5}\right)^2} \quad (3.16)$$

1113 where p_i ($i = 0, 2, \dots, 5$) are the free parameters which are determined by fitting of
1114 $f(x)$ to the deuteron data. The first term $p_0 \cdot f_p(x)$ in $f(x)$ represents the contribution
1115 from the contaminant (i.e., protons in ND_3) and the rest of the term in $f(x)$ represents
1116 the contribution from the deuterons in ND_3 . The total fit function $f(x)$, the proton
1117 contribution and the deuteron part are shown by the blue, green and black lines in
1118 the fourth panel. The ratio of the area under the green line to that under the blue
1119 line gives us the relative amount of the NH_3 contamination in the ND_3 target.

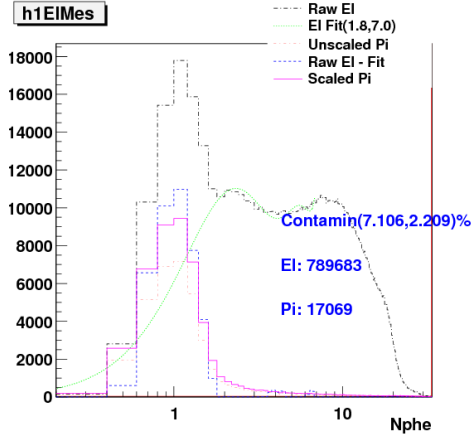
1120 3.9.4 Results and Conclusion

1121 From the calculation as described above, the estimate for the ND_3 contamination came
1122 out to be 4.4%. It was not possible to do a similar analysis on the 1.3 GeV ND_3 data,
1123 because the CLAS acceptance constraints did not allow for the coincident detection
1124 of e and p from the exclusive (quasi-)elastic events. The basic conclusion is that at 2
1125 GeV, we cannot get a 'pure' Gaussian spectrum for deuteron, and therefore, there is
1126 no way to unambiguously separate deuteron from proton in ND_3 . The fact that the fit
1127 looks reasonably well (with contamination coming out to be only a few percent) and
1128 that we clearly do not see a narrow peak on top of a wider one (unlike in EG1-DVCS)
1129 should be sufficient to ascertain that EG4 did NOT have the same contamination
1130 problem as EG1-DVCS (which still has not been explained yet) [26]. To accommodate
1131 the fact that the contamination measurement is not reliably unambiguous, we will
1132 assume a rather generous systematic error due to the contamination.

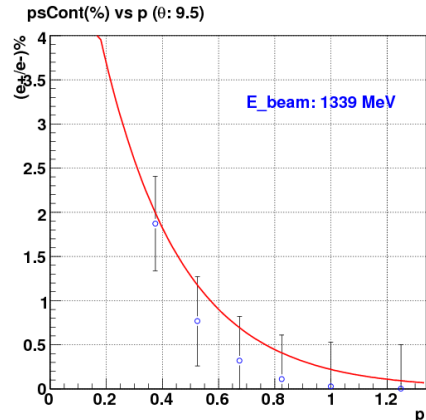
¹¹A pure Gaussian and other forms for the deuteron spectrum were tried but the overall fit was not as good.



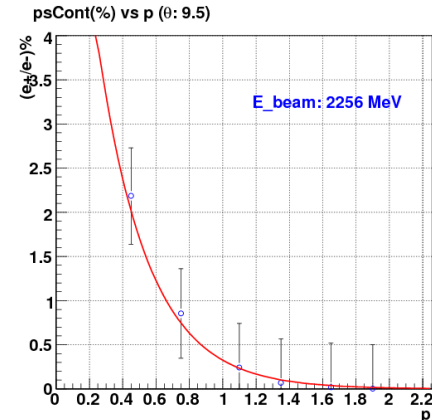
(a) For the first bin in momentum and seventh bin in θ .



(b) For the first bin in momentum and eighth bin in θ .



(c) Fits in the $\theta(9.0, 10.0)$ bin for 1.339 GeV data.



(d) Fits in the $\theta(9.0, 10.0)$ bin for 2.0 GeV data.

FIG. 3.34. The top row plots show the calculation of pion contamination of electrons for the given kinematic bins of 3.0 GeV data. The dotted black line indicated by the label “Raw El” in the legends of each of the two plots are the contaminated electrons. Likewise, the line labeled “El Fit” is a polynomial fit to the electron distribution (in this case fitted from $N_{phe}=1.8$ to 7.0 , but extrapolated down to $N_{phe}=0$). The line labeled “Unscaled Pi” is the pure pion distribution obtained with stringent set of cuts. “Raw El - Fit” is the difference between the contaminated electron sample and the polynomial fit and finally “Scaled Pi” is the pure pion-sample but after its scaled to match with the “Raw El - Fit” at the pion peak position (around 1 N_{phe}). The bottom row plots show the fits of the contaminations as a functions of momentum (p) in a given θ bin.

₁₁₃₃ **Chapter 4**

₁₁₃₄ **Monte Carlo Simulations and**
₁₁₃₅ **Extraction of g_1 and $A_1 F_1$**

₁₁₃₆ **4.1 Simulation and Approach to Analysis**

The EG4 data consist of a table numbers of electrons reconstructed within various (W, Q^2) bins that are scattered off polarized hydrogen (NH_3) or deuteron (ND_3), divided by the (life-time gated) integrated charge, for two different combinations of target polarization and beam helicity:

$$n^\pm = N^\pm / FC^\pm, \quad (4.1)$$

where “+” refers to beam helicity and target polarization anti-parallel, while “−” refers to the parallel case. The difference between these two normalized counts is given by

$$\Delta n(W, Q^2) = n^+(W, Q^2) - n^-(W, Q^2) = \mathcal{L}_r \cdot P_b P_t \cdot \Delta\sigma(W, Q^2) \cdot AccEff(W, Q^2) + Bg \quad (4.2)$$

₁₁₃₇ where the “relative luminosity” \mathcal{L}_r is a constant factor containing the density of
₁₁₃₈ polarized target nuclei per unit area and the conversion factor from Faraday cup
₁₁₃₉ counts to integrated number of electrons incident on the target; P_b and P_t are the beam
₁₁₄₀ and target polarization, Acc and Eff are the geometric acceptance and detection
₁₁₄₁ efficiency of CLAS for electrons within the kinematic bin in question (including cuts
₁₁₄₂ and trigger efficiency), and the background Bg comes from several sources, including
₁₁₄₃ pions misidentified as electrons, electrons from e^+e^- pair production, and electrons
₁₁₄₄ scattered off (partially) polarized target nucleons and nuclei that are not the intended
₁₁₄₅ species (e.g., bound protons in ^{15}N , free proton contamination in nominal ND_3 targets,

1146 and bound proton-neutron pairs in any ^{14}N contamination present)¹.

1147 Our main goal is to extract the spin structure function g_1 and calculate its mo-
1148 ments. The cross section difference $\Delta\sigma(W, Q^2)$ on the right side of the above equation
1149 is what contains the information on $g_1(W, Q^2)$ along with various other contributions.²
1150 This means we can, in principle, calculate the cross section (and then use that to ex-
1151 tract g_1), from the background corrected measured quantity $\Delta n(W, Q^2)$ by putting in
1152 the values for all the rest of the quantities involved in Eq. 4.2. But, in reality, having
1153 an accurate knowledge of Acc and Eff is challenging and the available measurements
1154 of polarizations and luminosities are not reliable enough. So, experimentalists usually
1155 resort to Monte-Carlo simulation to determine some or all of those factors that are
1156 involved in the relation between the counts and cross-section differences.

1157 A standard way to extract the sought-after Physics quantities from these kinds of
1158 measurements proceeds along the following steps [38]:

- 1159 1. Use a full simulation of CLAS with a “realistic” event generator, detector simu-
1160 lation and event reconstruction including cuts to obtain the product $AccEff$ as
1161 the ratio of events reconstructed in a particular bin, divided by events thrown
1162 in that same bin.
- 1163 2. Extract the product $\mathcal{L}_r \cdot P_b P_t$ from the ratio of the acceptance and efficiency
1164 corrected Δn in the (quasi-)elastic region ($0.9 < W < 1.0$) to the well-known
1165 theoretical cross section difference for elastic (or quasi-elastic) scattering off the
1166 proton (deuteron).
- 1167 3. Estimate and correct for Bg .
- 1168 4. Apply radiative corrections, which use a model of the unradiated Born cross
1169 section and a calculation of the radiated cross section based on programs like
1170 RCSLACPOL (see below).
- 1171 5. Express the extracted Born cross section difference in terms of the desired quan-
1172 tity (here: g_1) and additional inputs (e.g., $A_2 F_1$). Use a model for the latter
1173 to extract g_1 only. Vary the model (concurrently with the model input to the
1174 previous step) to assess systematic uncertainties.

1175 One conceivable problem with this approach lies in the first step, and in particular
1176 with the choice of the “realistic event generator”. However, this choice would not
1177 matter at all if two conditions are fulfilled [38]:

¹While this background is a small correction for hydrogen targets, in the case of deuteron targets, it must be corrected for (see Sec. 5.1).

² $\Delta\sigma(W, Q^2)$ also has contributions from the unmeasured g_2 or, equivalently, from the product $A_2 F_1$. Moreover, the cross section receives modifications and tails from radiative effects (both internal and external radiation) and kinematic resolution smearing.

- 1178 1. The kinematic bins are chosen so small that the variation of the cross section
 1179 over the bin (and/or the corresponding variation of the acceptance times effi-
 1180 ciency) do not lead to any significant deviations for the *average AccEff* between
 1181 the simulation and the real detector.
- 1182 2. The counts reconstructed within any one bin are directly proportional to the
 1183 number of initial electrons generated within that *same* bin (the proportionality
 1184 constant being *AccEff*), without any “bin migration” from other kinematic
 1185 bins. (Otherwise, the ratio reconstructed/generated depends on those “migra-
 1186 tion tails”, and the simulation will give different results from the “true value”
 1187 if the overall cross section model of the generator is not accurate enough.)

1188 Unfortunately, assumption 1 tends to directly contradict assumption 2 because 1
 1189 favors small bins and 2 favors large bins! For most precision experiments, bin mi-
 1190 gration effects are significant. This is aggravated by the difficulty of making a clean
 1191 separation between bin migration due to detector resolution alone and the contribu-
 1192 tion from radiative effects. For instance, GEANT and therefore GSIM includes (at
 1193 least by default) photon radiation as part of the simulation of outgoing electron tracks
 1194 throughout the gas and building materials of all detectors. It is very important not
 1195 to “double count” when simulating an experiment; the radiative calculations in step
 1196 4 above should not include any “after” radiation beyond the limit of the target itself
 1197 (which, in turn, should then **NOT** be included in the GSIM simulation as material
 1198 to be traversed).

1199 This is a problem for all CLAS experiments attempting to extract absolute cross
 1200 sections (or, here, cross section differences); however, the problem is magnified for our
 1201 case: Since the cross section difference itself is not required to be positive, one can
 1202 have both positive and negative tails migrating into adjacent bins. In any case, it is
 1203 clear that using the average, **unpolarized** cross section as a model for the generator is
 1204 not really appropriate (unless one is confident that the asymmetry is fairly constant or
 1205 slowly-varying – not a good assumption in the resonance region where the $\Delta(1232)$
 1206 with negative asymmetry is adjacent to the S11 with positive asymmetry). Using
 1207 a (hopefully realistic) model of the cross section difference instead would be much
 1208 better, but this causes two new problems [38]:

- 1209 1. Prima facie it is unclear how to simulate a negative cross section (difference).
 1210 This problem can be circumvented fairly easily (see below), albeit at extra cost
 1211 in terms of simulation effort.
- 1212 2. It obviously becomes impossible to extract *AccEff* from a simple ratio of re-
 1213 constructed divided by generated events; both of these quantities could be posi-
 1214 tive, negative (even different sign under extreme circumstances), or simply zero

(which is particularly bad for the denominator). From this discussion, it is also clear that such a ratio would depend very sensitively on the cross section model and bin migration tails and be a very poor indicator of the actual product $AccEff$.

For this reason, we decided to try a different approach outlined in the following. The basic idea is to study the dependence of the reconstructed count difference on the model input (in particular g_1) directly through the whole chain of simulation and reconstruction, and then use tables of Born and radiated cross section differences for various model inputs as estimates of systematic uncertainties³.

4.1.1 Outline of the method

The basic idea is the following: If we already had a perfect model of g_1 and all other ingredients that go into Δn (including a perfect simulation of CLAS), a simulation of Δn would agree 100% with the data (within statistical errors). Any (larger than statistical) deviation between such a simulation of Δn and the data can only be due to the following possible sources:

1. The model for g_1 is not perfect and, therefore, must be adjusted to reflect the “true” g_1 . This is the default assumption which we will use to extract g_1 from the data. This will be done by finding the proportionality factor between *small* changes in g_1 and the reconstructed Δn and then adjusting g_1 to fully account for the observed Δn .
2. There could be a systematic error on this proportionality factor (which, after all, will come from simulation); for instance, there could be systematic deviations from the simulated results for acceptance and efficiency (in particular efficiencies of the CC, EC, or tracking, that are not perfectly simulated by GSIM). This is a multiplicative uncertainty that must be carefully estimated and applied to the final data.
3. Any imperfect simulation of the “background” due to all events not originating in the bin in question (migration, radiation), or due to undesired target components (hydrogen, bound polarized nucleons in nitrogen), or from misidentified pions or e^+e^- pairs, or due to contributions to $\Delta\sigma$ from A_2 can lead to an additive systematic deviation that would then be misinterpreted as a change in g_1 . This systematic uncertainty must be studied by varying model inputs, parameters etc. in the simulation.

³We developed this method for the case of an ND₃ target; however, it could, of course, easily be adopted to NH₃, as well

1248 4.2 Radiative Corrections

1249 The physics quantities that we seek to extract from measurements are theoretically
1250 defined or interpreted and calculated in terms of the cross-section of the so called
1251 “Born” scattering process, which is represented by the simplest possible Feynman
1252 diagram i.e., by the lowest order approximation of a single photon exchange process.
1253 However, the measured cross-sections also contain contributions from higher order
1254 electromagnetic processes, which must be accounted for before extracting the quan-
1255 tities of our interest. These additional contributions are grouped into two categories
1256 - **internal and external** radiative corrections.

1257 The **internal corrections** are the contributions from the higher order QED pro-
1258 cesses (higher order Feynmann diagrams) which occur during the interaction. These
1259 include the correction for the internal Bremsstrahlung (i.e., the emission of a real
1260 photon while a virtual photon is being exchanged with the target) by the incoming
1261 or the scattered electron), the vertex correction (in which a photon is exchanged be-
1262 tween the incoming and the scattered electron), and the correction for the vacuum
1263 polarization of the exchanged virual photon (e^+e^- loops).

1264 External corrections include those that account for the energy loss (mainly by the
1265 Bremsstrahlung process) of electrons well before or after the interaction while passing
1266 through the target material and the detector.

1267 If the beam electron radiates a photon before the scattering, the kinematics of the
1268 actual process will be different from the the one calculated with the nominal beam
1269 energy. Likewise, if the radiation occurs after the scattering, the actual energy and
1270 momentum of the scattered electron will be different from what is calculated normally
1271 (i.e., without any radiation). The effect can be quite large for elastic scattering.

1272

1273 4.3 “Standard” simulation

1274 The simulation process consists of mainly three parts - generating inclusive events
1275 similar to the ones produced in the double polarization scattering process, simulating
1276 the CLAS detector response, and finally the event reconstruction from the simulated
1277 detector signals.

1278 The first part is accomplished by using a program that is made by combining the
1279 essential elements of an updated version of the “RCSLACPOL” program (for cross
1280 section generation) and some parts of the “STEG” (SimplesT Event Generator) event
1281 generator (see sections 4.3.1 and 4.3.2). The second part is done by two standard
1282 CLAS software packages running in succession - “GSIM” and “GPP”(see sections
1283 4.3.3 and 4.3.4). And, finally, the standard CLAS package “RECSIS” is used to

1284 reconstruct the events in the same way as for the real CLAS data.

1285 4.3.1 RCSLACPOL

1286 The simulation for the standard model cross sections proceeds as follows. We use the
1287 code “RCSLACPOL” [39] that can generate polarized and unpolarized cross sections
1288 (both Born and radiated) based on the approach by Shumeiko and Kuchto [40] as
1289 well as Mo and Tsai [41], including external radiation in the target. This code has
1290 been extensively tested and used for the analysis of SLAC experiments E142, E143,
1291 E154, E155 and E155x as well as Jefferson Lab experiments like EG1a and EG1b. It
1292 has been updated with the most recent models on polarized and unpolarized struc-
1293 ture functions (F_1, F_2, A_1 and A_2) [39, 42–44] and an implementation of the folding
1294 algorithm developed by W. Melnitchouk and Y. Kahn [45] for structure functions of
1295 the deuteron. The models have been fitted to and tested with data from EG1b as
1296 well as world data on both A_1 and A_2 over a wide range of Q^2 and W , including the
1297 resonance region and the DIS region.

1298 For EG4, we have combined the “RCSLACPOL” code with that of the “STEG”
1299 event generator. This generator uses a grid of (radiated⁴) cross sections generated
1300 by our modified version of RCSLACPOL to generate events that are distributed
1301 according to these cross sections (i.e., the number of events generated in a given bin
1302 is proportional to the cross section integrated over this bin).

1303 4.3.2 Event Generator

1304 The concept and some part of the generator skeleton was inherited from the STEG
1305 (SimplesT Event Generator) program obtained from INFN, in Genova, Italy. The
1306 old event sampling part (which made the program run extremely slow) of the code
1307 was replaced by a new one developed by myself which made the event generation
1308 process much faster. The cross section calculating part was replaced by codes from
1309 an updated version of RCSLACPOL (see Sec. 4.3.1).

1310 The generator works in two steps. First, it generates two separate two-dimensional
1311 maps or tables (in $(p, \cos \theta)$ space) of radiated inclusive polarized cross differences (for
1312 the scattering of polarized electrons from a longitudinally polarized deuteron target,
1313 by using RCSLACPOL) in various kinematic bins encompassing the kinematic region
1314 covered by EG4 data. One map is for positive values of polarization $\Delta\sigma$ and the
1315 other is for negative values of the polarization. These cross section maps (and the
1316 corresponding events later on) were generated in the following angular and momentum

⁴Radiative effects are simulated by passing RADB and RADA as input parameters to the RCSLACPOL program, where RADB and RADA are the average radiation lengths of the materials that the electron passes through before and after scattering.

ranges: 5.0-45.0 degrees for θ , 250.0-325.0 degrees for ϕ (to ensure the CLAS 6th sector is completely covered) and $(0.2, E_{beam})$ GeV for the momenta ($p \approx E'$), where the beam energy E_{beam} took values of 1.337 and 1.993 GeV, corresponding to the two ND₃ data sets of EG4. In our case, the map was created by dividing the kinematic phase space into a grid of small rectangles and then calculating the differential cross-section at the geometric center of each of those squares (such as ABCD in Fig. 4.1). For our application, we need to generate two such maps (because of the impossibility of generating events according to negative cross-sections) and run the program twice - once corresponding to positive $\Delta\sigma$ and the next for the negative one. For all bins in which the integrated cross section $\Delta\sigma \geq 0$, we fill the first table (“positive map”) which is therefore positive-definite. For all bins in which this cross section is below 0, we fill a second table (“negative map”), but with the absolute (i.e. negative) value of this cross section.

In the second stage, events are thrown according to the cross section maps produced in the first stage. The events are given vertex coordinates that are uniformly distributed over the volume of a 1 cm long cylinder with radius 0.01 cm around the beam line - with the center of this volume being at the EG4 target position of (0,0,-100.93 cm). Nearly equal numbers of events are generated for each sign of $\Delta\sigma$; they are finally normalized according to their total cross sections (integrals of the corresponding maps).

The kinematic and other information (positions, momenta, charge) of these generated events are recorded and saved in the BOS format⁵ output files which organizes data into banks. In our case, HEAD, MCEV, MCTK, and MCVX banks are used for the generator output. The generator is also capable of producing output in the hbook format which makes it possible to study the Monte Carlo data using PAW (or ROOT because the h2root program easily converts “hbook” files into “root” files).

4.3.3 GSIM - CLAS Detector Simulation

The Monte Carlo events thus generated are next fed into GSIM - the CLAS Monte Carlo simulation program using GEANT 3.21 libraries from CERN [46]. It simulates the CLAS detector response by implementing a complete model of the detector as well as the propagation of particles through different materials including all physics processes, such as multiple scattering, energy loss, pair production, and nuclear interactions. The program takes the input event particles and then, based on their types, momenta and positions, “swims” (traces) them through all volumes of different materials that are defined using various library routines and the detector parameters. Charged particles are also subjected to the effects of the torus and target magnetic

⁵Existing versions of GSIM, GPP and RECSIS accept only BOS format for input files.

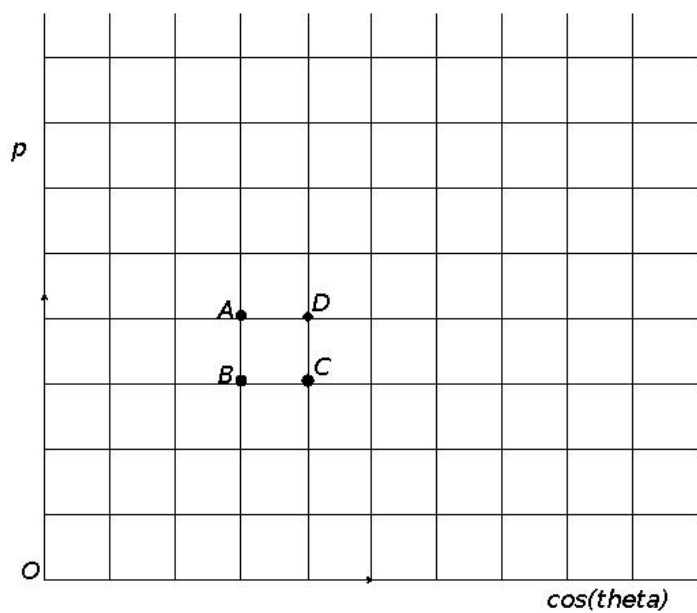


FIG. 4.1. Corners of a typical bin highlighted in the kinematic space covered by the event generator.

1353 fields of the same strength as in the actual experiment (for this the same field maps
1354 are used as in the track reconstruction process using RECSIS). All the ingredients
1355 of the program (field maps, active detection volumes, passive volumes of detector
1356 support structures etc) are modeled as accurately as possible with the help of engi-
1357 neering designs and actual detector measurements. Special subroutines corresponding
1358 to various active parts of the detector produce outputs resembling the real detector
1359 signals which can then be reconstructed and analyzed just as the real experimental
1360 data [47][48]. GSIM is configured to match with the conditions of a given experiment
1361 by giving it proper values of input parameters via a command line input file which
1362 contains various “ffread cards” some of which are listed in table-A.1 along with their
1363 values that were used in our simulation.

1364 **4.3.4 GSIM POST PROCESSOR (GPP)**

1365 The GSIM output is next passed onto GPP - another standard CLAS software package
1366 - to process the simulated data further so that the detector response is accounted for
1367 more accurately. This package improves the response by smearing the detector signals
1368 and removing them if there are dead regions (determined by querying a data base
1369 which in turn is made by looking at the raw data of the experiment).

1370 A lot of known, unknown, quantified, and unquantified factors such as temper-
1371 ature, alignment, dead channels, electronic malfunction etc affect the performance
1372 of the CLAS detector. But, GSIM does not include all these effects and, hence,
1373 the efficiency of the detector is always less than what the simulation provides us.
1374 To make the simulation more realistic by taking into account some of those effects,
1375 another CLAS software called GSIM Post Processor (GPP) is used to process the
1376 GSIM output. The GPP can change the DC, SC, CC and EC signals produced in
1377 the simulation⁶.

1378 As the experimental conditions and detector configurations can change from one
1379 experiment to another, in order to run the GPP, we must have our own experiment
1380 specific calibration constants and parameters such as the run number (R), the DC
1381 smearing scale values for regions 1, 2 and 3 (a, b, c) and the SC smearing scale value
1382 (f). Even for a given experiment, these constants and parameters are determined
1383 to be different for different data sets (corresponding to a given beam energy, for
1384 example). The value for R can be any run number belonging to a specific data set.
1385 This number is used to identify the entry of the calibration constants in the database

⁶The DC signals can be changed by (a) accounting for the dead wires according to the calibration database, (b) shifting the DOCA mean value, and (3) smearing the hit signals according to the resolution determined by the calibration database or according to the command line input. Likewise, SC signals can be changed with a parameter input for smearing the time resolution. And, for EC signals, the GPP can use the hardware thresholds [49].

1386 that corresponds to the given data set. In order to simplify the job, we decided to use
 1387 the timing resolutions determined by the calibration database assuming that they are
 1388 good enough and need only to determine new values for the DC smearing. To further
 1389 simplify the job, we assumed that the three DC Regions had identical resolutions, so
 1390 the DC smear parameters a, b, and c would have the same values, and the common
 1391 DC-smear value is what is determined from the procedure described below.

1392 In order to determine the DC-smear, we generated a statistically significant num-
 1393 ber (about half million) of elastic-electron events distributed according to the elastic
 1394 cross section and then ran them through GSIM, GPP and RECSIS. The pure proton
 1395 target events, turning off the radiative effects are generated using the existing STEG
 1396 event generator.

1397 The simulated elastic events are then fed into GSIM, GPP and RECSIS, with
 1398 GSIM and RECSIS used in the same configuration as when processing the CLAS
 1399 data during the “pass-1” phase, and GPP run with different values of DC-smear
 1400 scales as inputs. The reconstructed data coming out of RECSIS corresponding to a
 1401 given value of DC-smear is then histogrammed in ΔE again and fitted to a Gaussian
 1402 to get its σ (characterizing width) and mean (characterizing position). As we can see
 1403 in figures 4.2(a) and 4.2(b), the width of the elastic peak increases with the DC-smear
 1404 but the position stays more or less the same as expected. In fact, when the two are
 1405 plotted against DC-smear (as in figures 4.3(a) and 4.3(b)) the width shows a linear
 1406 dependance.

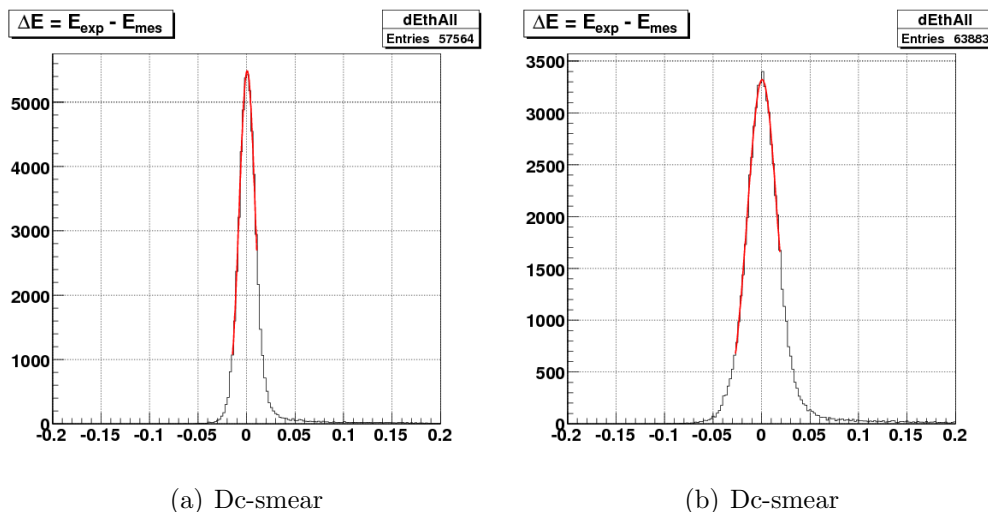


FIG. 4.2. ΔE of 2.3 GeV simulated elastic-only proton-target events passing through GSIM, GPP (with two different Dc-smear scales of 1.3 (a) and 2.9 (b)), and RECSIS.

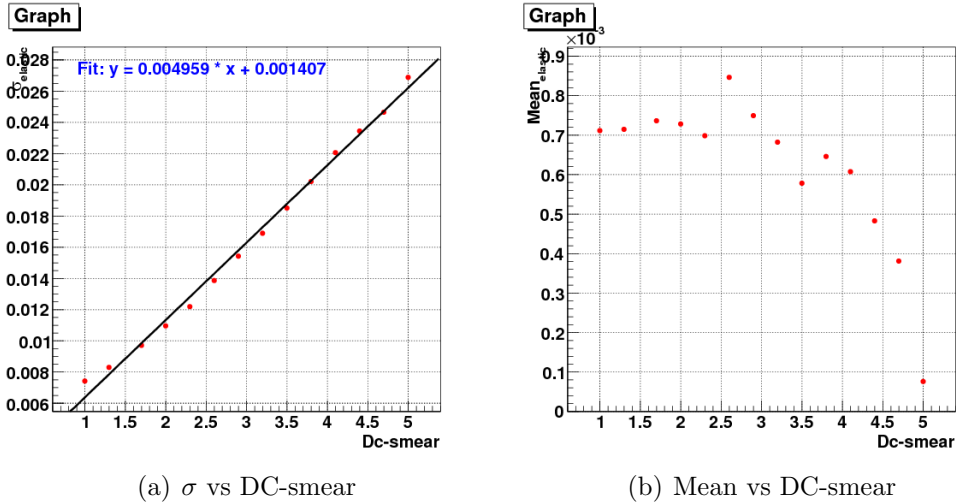


FIG. 4.3. Graphs showing the dependence of width and position (obtained from the Gaussian fits of the elastic peaks on the DC-smear applied to GPP).

With the knowledge of the DC-smear dependence of energy resolution (Fig. 4.3(a)), we can look at the resolution in the real data such as the one estimated in Fig. 3.27, and then determine the right value of DC-smear which would make the resolution in the simulation comparable with that in the real data. By repeating this process of comparing the experimental and simulated resolutions for each of the beam energies, the values of the DC-smear parameters for the GPP were determined as listed in Table. 4.1 below.

Table 4.1: DC-smearing scales determined for different beam energies.

E_{beam} (GeV)	1.054	1.339	1.989	2.256	2.999
DC-smear	2.6	2.0	2.0	2.0	1.7

1414

1415 4.4 Comparison of Data and Simulation

Using our final values for the smear parameters, the simulated data were passed through GPP and then reconstructed with RECSIS. Finally, all applicable cuts and corrections were applied to both sets of polarized simulation data. Because the CC was turned off in GSIM for the simulation, all experimental data cuts except those depending on CC were applied to the simulated data. However, the cuts were modified (see Sec. 3.3) to account for differences between simulation and data.

1422 In the end, we had two sets of simulated events (for the two cases of $\Delta\sigma \geq 0$ and
 1423 $\Delta\sigma < 0$) in each kinematic bin. The number of these two type of events in each bin
 1424 were then cross-normalized with respect to each other by their respective cross-section
 1425 map integrals and the number of generated Monte-Carlo events and then combined
 1426 to make the simulated polarized count difference Δn . To do that, the number of
 1427 simulated event counts in a kinematic bin corresponding to the positive $\Delta\sigma$ was kept
 1428 unchanged but the one corresponding to the negative $\Delta\sigma$ was multiplied with the
 1429 following normalization factor:

$$norm^- = \frac{\sigma_{tot}^-}{\sigma_{tot}^+} \times \frac{N^+}{N^-} \quad (4.3)$$

1430 where $\sigma_{tot}^{+/-}$ and $N^{+/-}$ are the total integral of the cross section map and the corre-
 1431 sponding number of Monte-Carlo events generated for each of the polarization cases
 1432 (+/-).

1433 The next step was to properly cross-normalize the simulated events to the data.
 1434 For this, we found the scale factor SF necessary to have the same Δn in the quasi-
 1435 elastic region (e.g., $0.9 \leq W \leq 1.0$). This factor represents the ratio

$$SF = \frac{n^+ - n^-}{\Delta n(simul)} \quad (4.4)$$

1436 since the physics of QE is known (from form factors etc), we expect the simulation
 1437 in this region is reliable and all other factors⁷ are common to the simulation and the
 1438 data. In fact, we chose one Q^2 bin (the 20th one - for which the agreement between the
 1439 data and simulation was among the best) and calculated above ratio to get the global
 1440 preliminary value of the scaling factor SF_{20} . The simulated Δn was then multiplied
 1441 with this factor to get our best “prediction” of the real data in all the kinematic bins,
 1442 in order to directly compare it with the real data (see Figs. 4.4 and 4.5).

⁷The scaling factor (SF) accounts for the luminosity, the product of the beam and target polarization ($P_b P_t$, and all other constant efficiency factors such as dead time, overall trigger efficiency, average tracking efficiency etc.

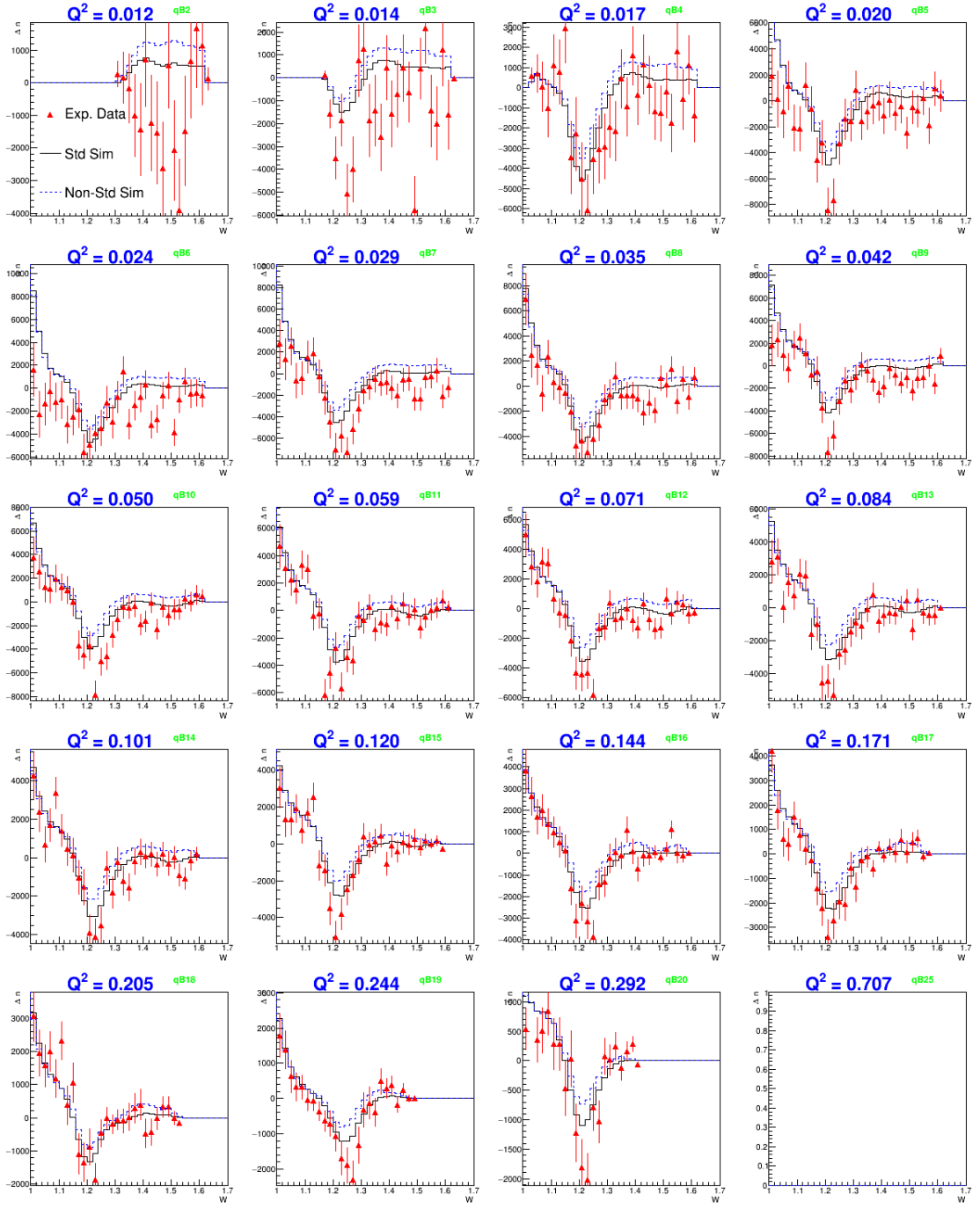


FIG. 4.4. Comparison (in different Q^2 bins) of polarized count differences from 1.3 GeV experimental (red points with error bars) and two versions of normalized simulation data. The black continuous histograms are for “standard” simulation with values of A_1 in the inelastic region as given by the model used in the simulation. The blue dotted histograms are for “non-standard” simulated data with A_1 changed to $A_1 + 0.1$.).

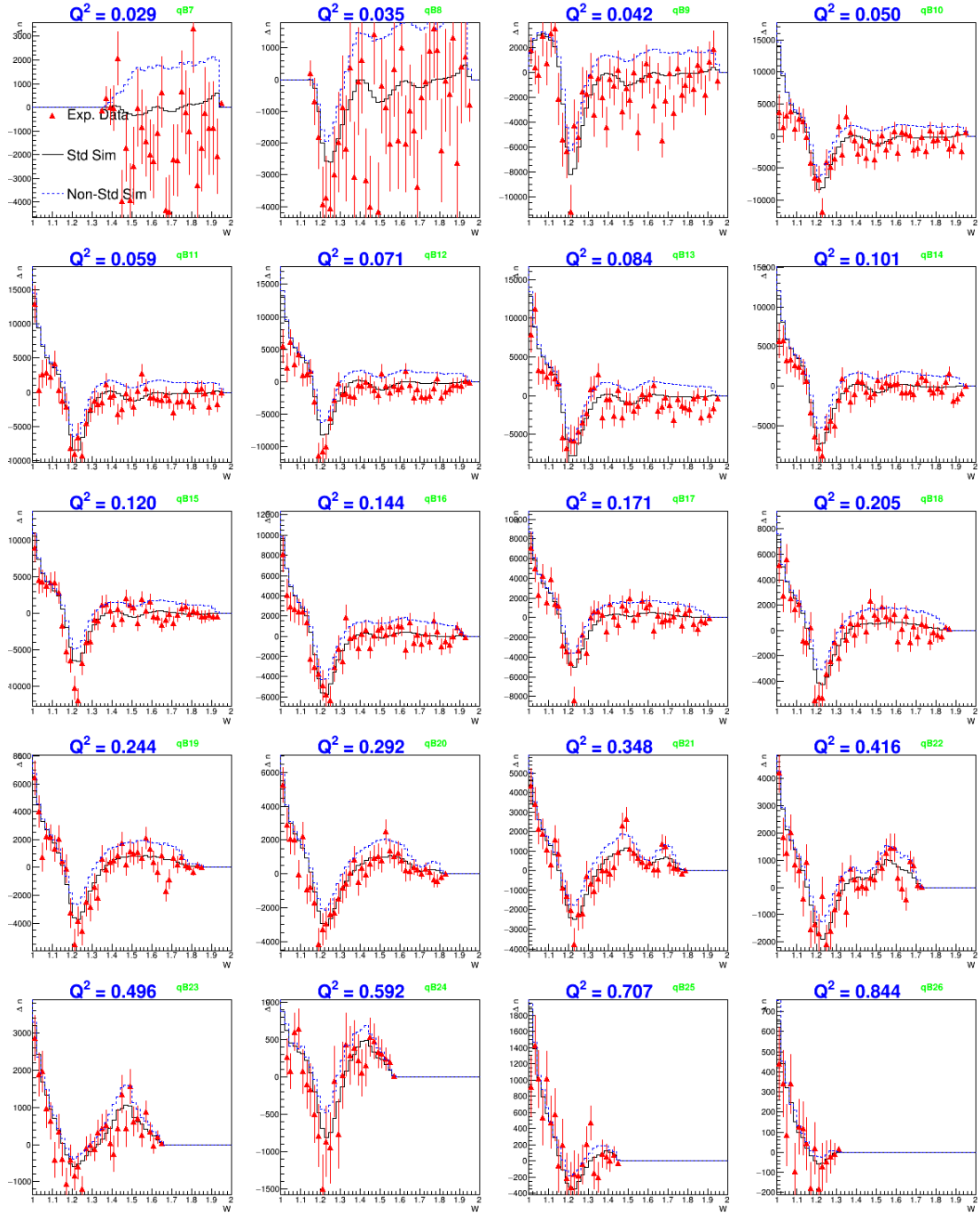


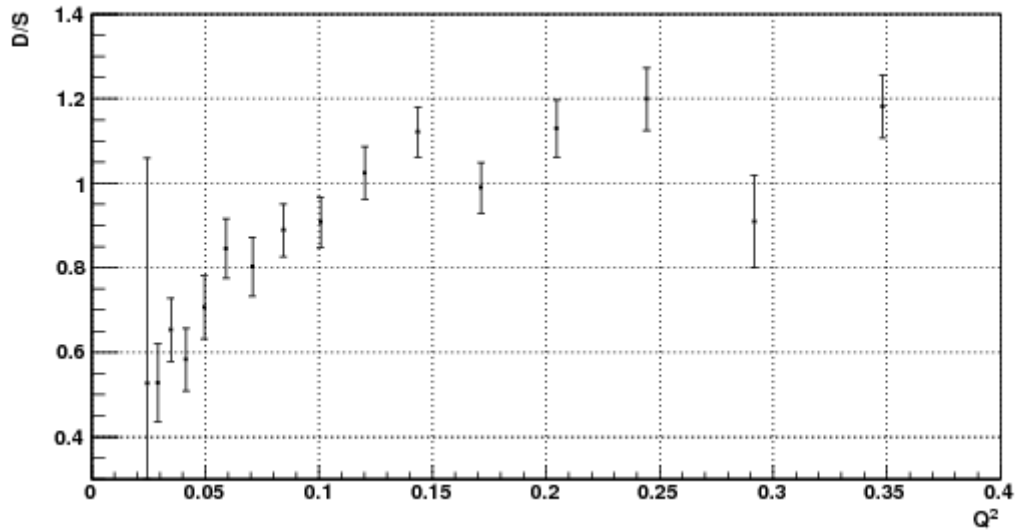
FIG. 4.5. Comparison (in different Q^2 bins) of polarized count differences from 2.0 GeV experimental (red points with error bars) and two versions of normalized simulation data. The black continuous histograms are for “standard” simulation with values of A_1 set as given by the used model. The blue dotted histograms are for “non-standard” simulated data with A_1 changed to $A_1 + 0.1$.

¹⁴⁴³ After this normalization, the ratios $(n^+ - n^-)/\Delta n(simul)$ in the quasi-elastic re-
¹⁴⁴⁴ gion for all Q^2 bins were calculated and plotted versus Q^2 as well as θ (see Figs. 4.6(a) -
¹⁴⁴⁵ 4.9(a)) along with the corresponding statistical errors as given by $\sqrt{(n^+ + n^-)/\Delta n(simul)}$.
¹⁴⁴⁶ As the figures show, the ratio in the quasi-elastic region drops off rapidly at small Q^2 .
¹⁴⁴⁷ The fall-off is likely due to CC inefficiencies for very high momenta and very forward
¹⁴⁴⁸ angles. Also, our simple cross section model for the deuteron is less accurate at low
¹⁴⁴⁹ Q^2 . Figures 4.6(b) - 4.9(b) show that the Δ -resonance region does not suffer from
¹⁴⁵⁰ similar problems as the Delta model is quite reliable too (just like QE model).

¹⁴⁵¹ The final normalization was obtained by calculating the error weighted average
¹⁴⁵² $SF_{average}$ of above ratios in the quasi-elastic region. The average was calculated
¹⁴⁵³ using only those Q^2 bins which had ratios reasonably stable and closer to each other.
¹⁴⁵⁴ Because, the ratios are reasonably stable only above $Q^2 \approx 0.045$ GeV 2 and $Q^2 \approx 0.09$
¹⁴⁵⁵ GeV 2 in the 1.337 and 2.0 GeV data sets respectively (as can be seen from Figs.
¹⁴⁵⁶ 4.6(a) and 4.8(a)), only those Q^2 bins above these two limits were used in calculating
¹⁴⁵⁷ the weighted average of these ratios. In addition, even above those two limits, some
¹⁴⁵⁸ of those which had too large ratios - greater than 2.0 (or 2.5) for 1.337 (or 2.0) GeV
¹⁴⁵⁹ data set- were not used in the weighted average. However, it should be noted that the
¹⁴⁶⁰ bins not used in the average ratio calculations were not entirely discarded from the
¹⁴⁶¹ final analysis. Only those below $Q^2 = 0.02$ GeV 2 were completely thrown out from
¹⁴⁶² the final analysis because they did not cover the resonance (particularly the Δ) region
¹⁴⁶³ very well. The resulting simulated data in the form of count differences Δn in various
¹⁴⁶⁴ Q^2 bins are shown in Figs. 4.4 and 4.5 along with the corresponding experimental
¹⁴⁶⁵ data.

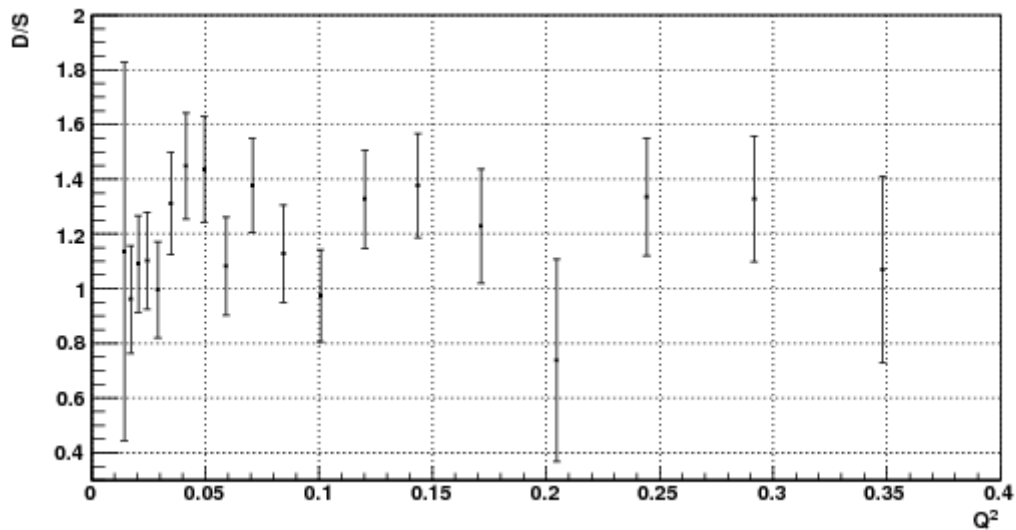
¹⁴⁶⁶ A complete systematic error analysis was done to study the effect of the overall
¹⁴⁶⁷ scaling factor SF on the extracted g_1 (see below) and to estimate its statistical (due to
¹⁴⁶⁸ the number of counts) and systematic (due to model uncertainties and backgrounds)
¹⁴⁶⁹ error.

Data/Sim for W(0.9,1.05)



(a) Data/Sim ratio vs Q^2 in 1.3 GeV quasi-elastic data.

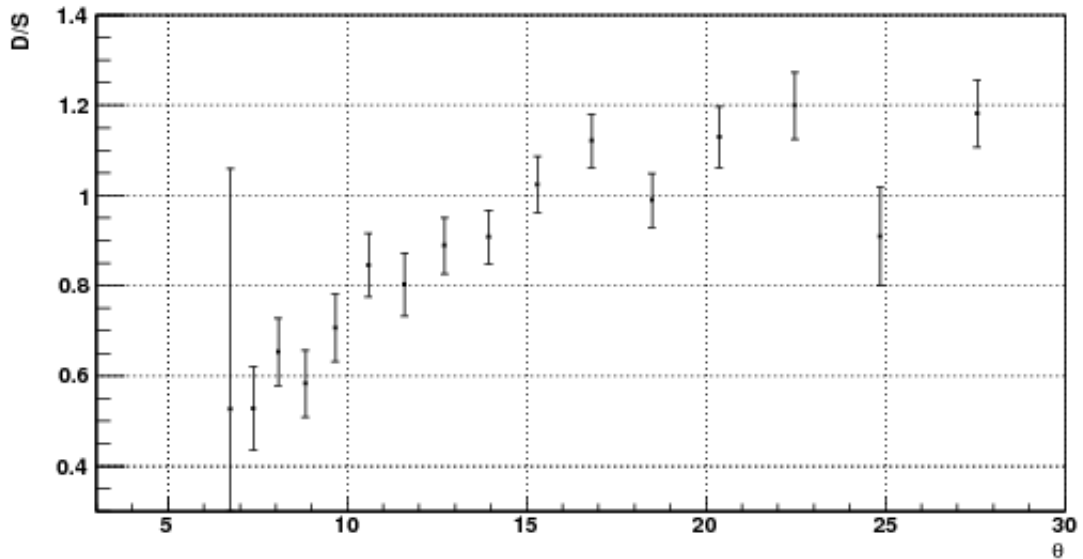
Data/Sim for W(1.15,1.3)



(b) Data/Sim ratio vs Q^2 in Δ -resonance region of 1.3 GeV data.

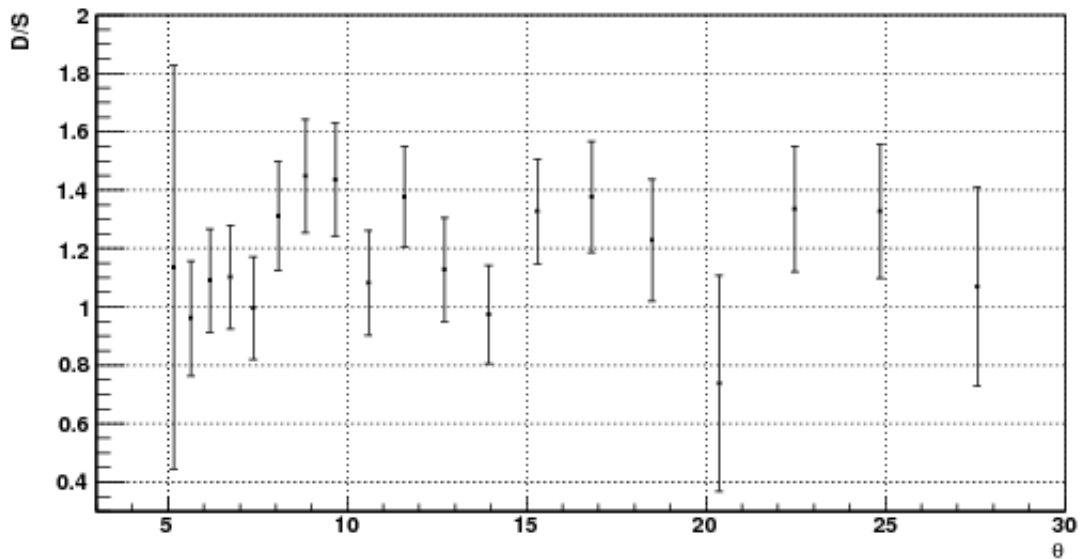
FIG. 4.6. Q^2 dependence of ratios of 1.3 GeV data and simulation in the quasi-elastic and Δ -resonance regions.

Data/Sim for $W(0.9, 1.05)$



(a) Data/Sim ratio vs θ in 1.3 GeV quasi-elastic data.

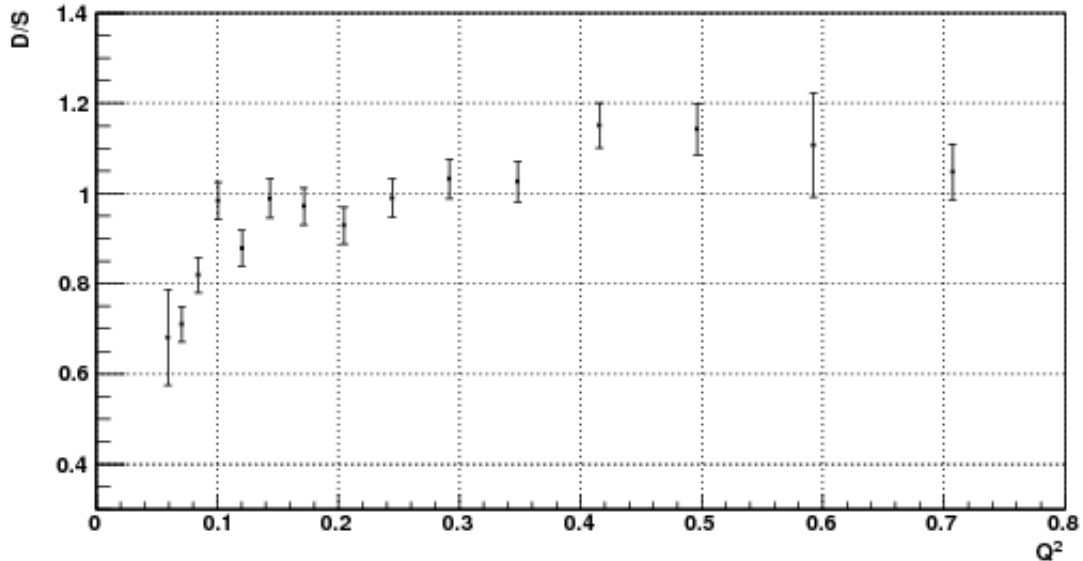
Data/Sim for $W(1.15, 1.3)$



(b) Data/Sim ratio vs θ in Δ -resonance region of 1.3 GeV data.

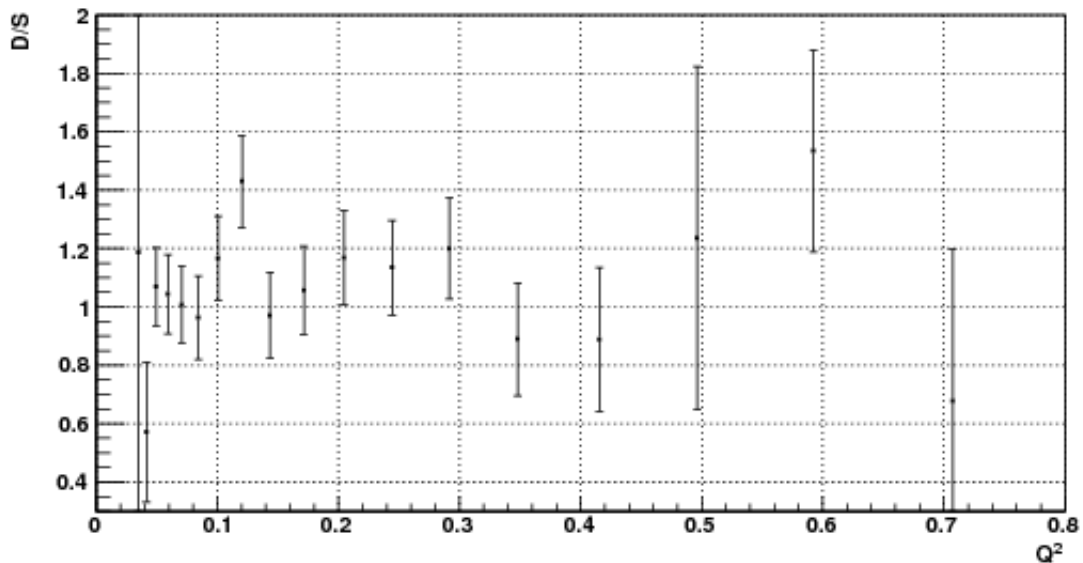
FIG. 4.7. The same data as in Fig. 4.6, but plotted versus average scattering angle (θ). Here we can see that the data for $\theta > 10^{\circ}$ are reasonably stable with $\pm 10\%$ fluctuation (which will be taken into account while calculating the systematic uncertainty later).

Data/Sim for W(0.9,1.05)



(a) Data/Sim ratio vs Q^2 in 2.0 GeV quasi-elastic data.

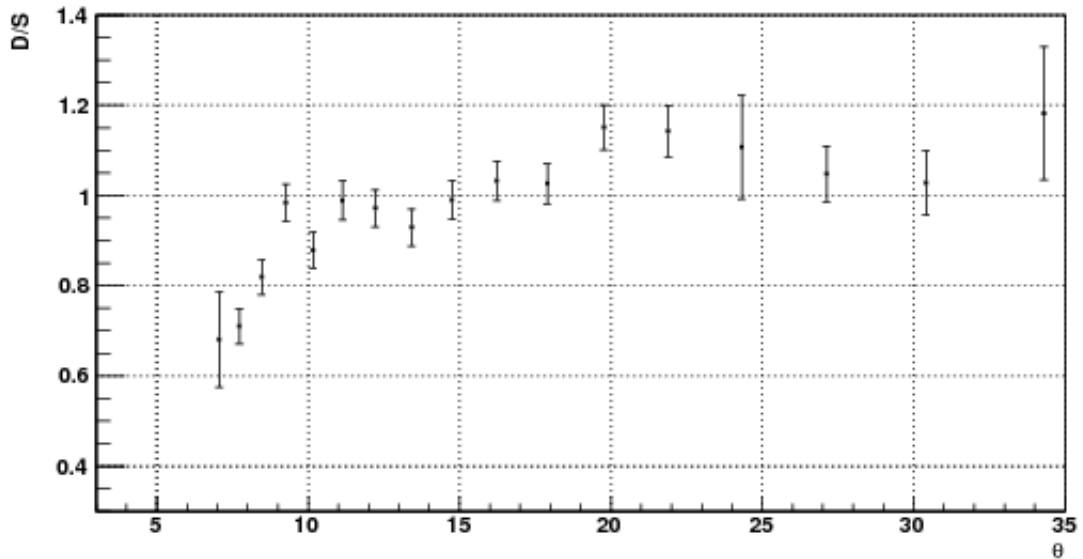
Data/Sim for W(1.15,1.3)



(b) Data/Sim ratio vs Q^2 in Δ -resonance region of 2.0 GeV data.

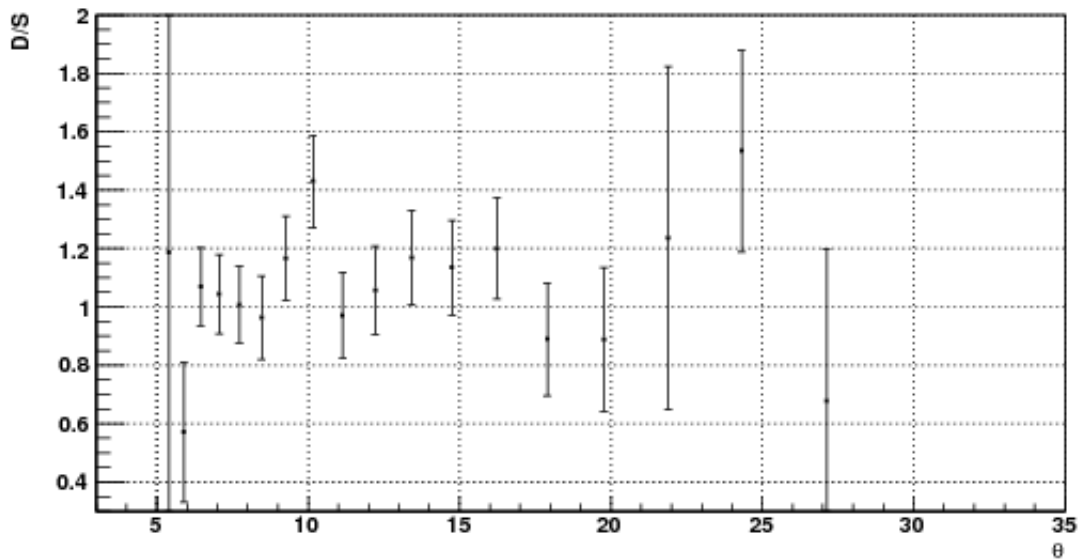
FIG. 4.8. Q^2 dependence of ratios of 2.0 GeV data and simulation in the quasi-elastic and Δ -resonance regions.

Data/Sim for W(0.9,1.05)



(a) Data/Sim ratio vs θ in 2.0 GeV quasi-elastic data.

Data/Sim for W(1.15,1.3)



(b) Data/Sim ratio vs θ in Δ -resonance region of 2.0 GeV data.

FIG. 4.9. The same data as in Fig. 4.8, but plotted versus average scattering angle (θ). Here we can see that the data for $\theta > 10^\circ$ are reasonably stable with $\pm 10\%$ fluctuation (which will be taken into account while calculating the systematic uncertainty later).

1471 4.5 Method to Extract g_1 and $A_1 F_1$

1472 4.5.1 ‘Variation’ of the standard simulation

The whole chain of steps outlined in the previous sections for the standard simulation is repeated with just one major difference: the model input for the asymmetries A_1 for both the proton and the neutron are increased by a constant value⁸ of 0.1. With all other model ingredients being kept constant, this change leads to a change of the spin structure function g_1 that can be straightforwardly calculated for each kinematic bin within the model:

$$\delta g_1(W, Q^2) = \delta A_1 \times F_1 \frac{\nu^2}{\nu^2 + Q^2} \quad (4.5)$$

1473 Correspondingly, the simulated count difference $\Delta n(W, Q^2)$ will change to a new
 1474 value $\Delta n'$. This ‘non-standard’ simulation with $A_1 = A_1(\text{standard}) + 0.1$ is per-
 1475 formed generating an about equal number of Monte-Carlo events. The final recon-
 1476 structed data is then multiplied with the same overall scaling factor SF as for the
 1477 standard simulation and then further (cross-)normalized by one additional factor
 1478 $SF_{ext} = (\sigma_1^p / \sigma_2^p) / (N_1 / N_2)$ to account for the change in cross section map and the
 1479 (slight) difference in the number of the generated events between the standard and
 1480 non-standard simulations. Here, σ_1^p and σ_2^p are the total cross sections for the positive
 1481 $\Delta\sigma$ maps used for the standard and non-standard simulations and, N_1 and N_2 are the
 1482 corresponding numbers of generated events. See Fig. (4.10) to see how the polarized
 1483 count differences look (in one particular Q^2 bin) in experimental and simulated data
 1484 after such normalizations (for all other Q^2 bins, see Figs. 4.4 and 4.5).

This change of the simulated $\Delta n(W, Q^2)$ to a new value $\Delta n'$ can be correlated to the increase in g_1 by solving for the two parameters A and B of the linear equation,

$$\Delta n(\text{simul}) = A + B \cdot \delta g_1, \quad (4.6)$$

where $A(W, Q^2)$ is the result for the simulated Δn for the standard set of model inputs i.e., $A(W, Q^2) = \Delta n^{\text{standard}}(W, Q^2)$, and $B(W, Q^2)$ is the proportionality factor representing the change in $\Delta n(\text{sim})$ per unit change in g_1 , as given by:

$$B(W, Q^2) = \frac{\Delta n' - \Delta n}{\delta g_1}. \quad (4.7)$$

⁸We arbitrarily chose 0.1 in the inelastic region, but could also have used any other value (not too big, however).

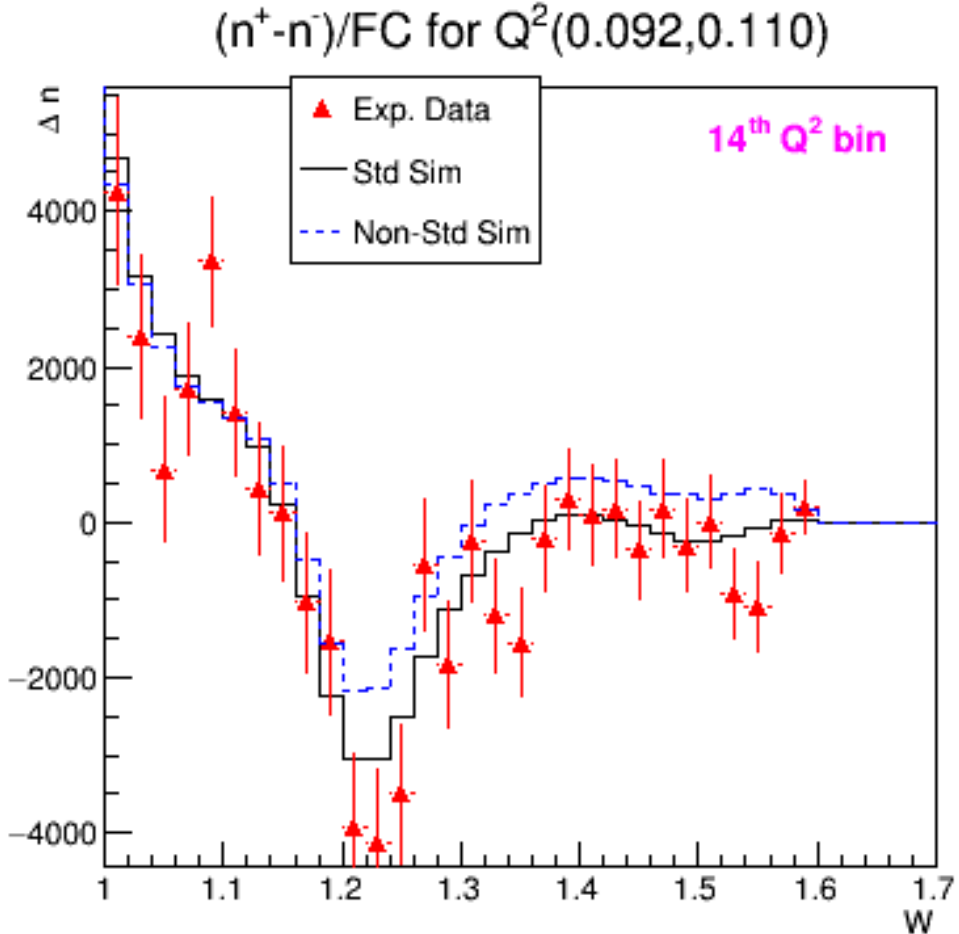
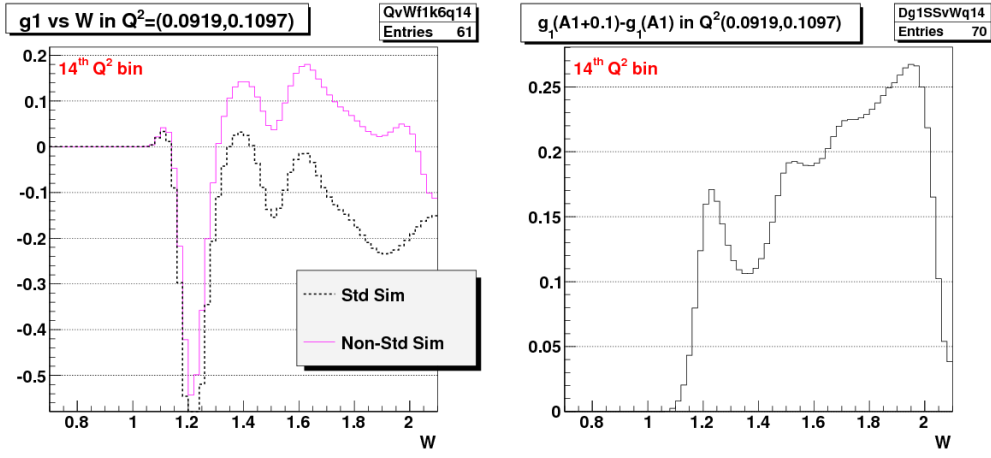


FIG. 4.10. Δn of experimental data and two versions of simulations in one particular Q^2 bin for 1.3 GeV case (for data on more Q^2 bins, see Fig. 4.4).

Similarly, in case of $A_1 F_1$ evaluation, the factor is given by:

$$B(W, Q^2) = \frac{\Delta n' - \Delta n}{\delta A_1 F_1}. \quad (4.8)$$

The proportionality factor $B(W, Q^2)$ is then determined for each of the kinematic bins (in (W, Q^2)) in which the experimental data has been histogrammed. For this purpose, using the RCSLACPOL program, we produce two values of structure function g_1 in each kinematic bin - one is $g_1^{Standard}$ corresponding to the standard simulation and the other is $g_1^{non-standard}$ corresponding to the non-standard simulation. By dividing the above change in the count difference with the difference Δg_1 of these two



(a) g_1 for standard and non-standard simulation

(b) Difference of the two g_1

FIG. 4.11. Plots showing the change in model g_1 due to the change of A_1 to $A_1 + 0.1$.

1491 structure functions, we get the factor $B(W, Q^2)$ for the bin. The similar procedure is
 1492 followed to get the corresponding values of $B(W, Q^2)$ in the case of $A_1 F_1$ evaluation.

In principle (and ignoring the other enumerated possible sources of disagreement between data and simulation), we can then easily find the “amount of change” δg_1 to be added to the standard model g_1 to get perfect agreement:

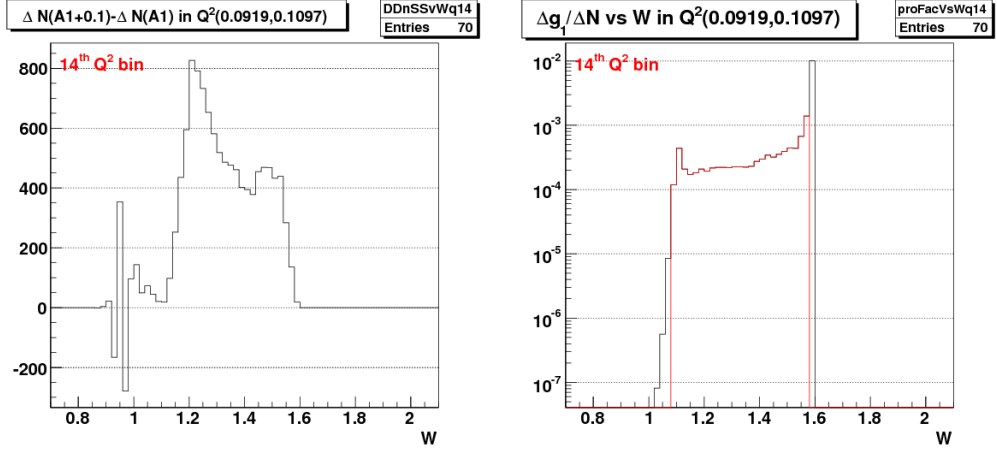
$$\delta g_1 = g_1^{extr}(W, Q^2) - g_1^{Standard} = \frac{\Delta n^{data}(W, Q^2) - \Delta n^{standard}(W, Q^2)}{B(W, Q^2)} \quad (4.9)$$

1493 where the values of Δn^{data} and $\Delta n^{standard}$ come from the polarized count differences
 1494 Δn in the experimental data and the standard simulation respectively (as shown, for
 1495 example, by the red points and black histograms in Fig. 4.10 for one particular Q^2
 1496 bin).

It is also straightforward to propagate the statistical uncertainty to the extracted g_1 . The statistical uncertainty in this extracted quantity totally comes from the uncertainty in the experimental counts Δn^{data} (assuming there is no uncertainty in the model quantities involved and also in the simulation counts because we did our simulation with large enough statistics to warrant ignoring the uncertainties) as follows:

$$\sigma(g_1^{extr}(W, Q^2)) = \frac{\sigma(\Delta n^{data}(W, Q^2))}{B(W, Q^2)}. \quad (4.10)$$

1497 The values of g_1 and its uncertainties thus extracted from 1.3 GeV data for one
 1498 Q^2 bin is shown in Fig. (4.13(b)). Similar results for all the bins from two beam
 1499 energy data sets in different kinematic bins can be seen in Fig. 6.1.



(a) Change in $\Delta n(sim)$ simulated count difference i.e. $\Delta N = \Delta n'(A_1 + 0.1) - \Delta n(A_1)$ due to the change of A_1 to $A_1 + 0.1$ (for 1.3 GeV case). (b) Proportionality factor ($1/B(W, Q^2)$) for 1.3 GeV case. Black is the original values. Red is the ones kept after discarding the first or last few (low statistics bins) that had unreasonably high (suddenly changing) ratios. This ensures we only show final data with “good” proportionality factor.

FIG. 4.12. Plots for $\Delta n(sim)$ and the corresponding proportionality factors.

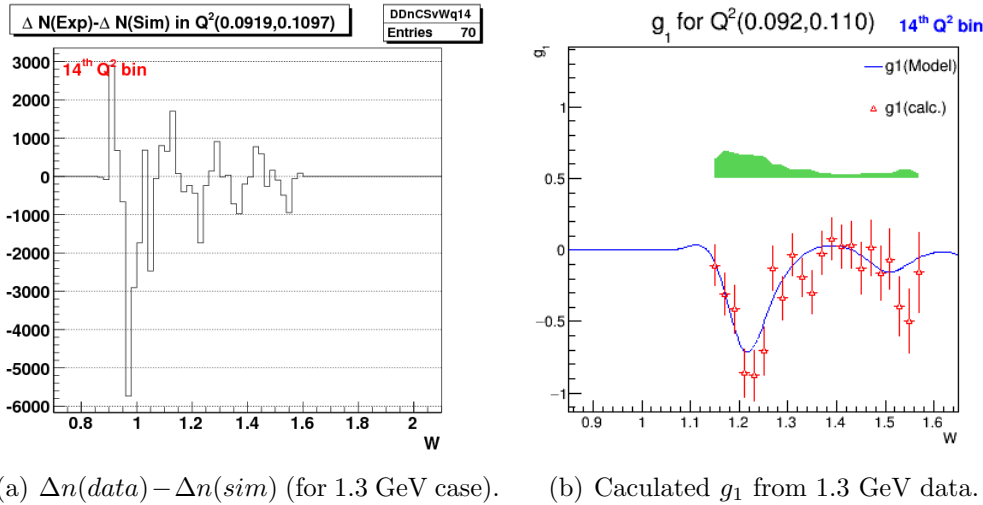
Because we are also interested in measuring the forward spin polarizability and the extended GDH integral, we also extract the product $A_1 F_1$ which enters these integrals. We followed the exact same procedure for g_1 as outlined above. We determined new proportionality factors in each kinematic bin, again using Eq. 4.12 as before but with the denominator replaced, this time, with the corresponding change in $A_1 F_1$ (instead of the change in g_1). Then we can use the following expression (similar to equation 4.9) to extract $A_1 F_1(W, Q^2)$:

$$\delta A_1 F_1 = A_1 F_1^{extr}(W, Q^2) - A_1 F_1^{Standard} = \frac{\Delta n^{data}(W, Q^2) - \Delta n^{standard}(W, Q^2)}{B_{A_1 F_1}(W, Q^2)} \quad (4.11)$$

where

$$B_{A_1 F_1}(W, Q^2) = \frac{\Delta n' - \Delta n}{\delta A_1 F_1}. \quad (4.12)$$

And, the uncertainties on $A_1 F_1$ can also be dealt in the same way as on g_1 .



(a) $\Delta n(data) - \Delta n(sim)$ (for 1.3 GeV case). (b) Calculated g_1 from 1.3 GeV data.

FIG. 4.13. Plots for $\Delta(\Delta n)$ and the corresponding extracted g_1 . On the left, $\Delta(\Delta n)$ are the difference of the normalized count differences from the experimental and simulated (using 'standard' model) data. In other words, this gives the common numerator for Eqs. 4.12 , 4.8. On the right, the blue line is that of the model g_1 that was used in the simulation when the quasi-elastic part was turned off. We used $g_1^{extracted} = g_1^{q.e.Off} + \delta g_1$ to get the measured g_1 , where δg_1 is the calculated deviation (using Eq. 4.9) of the experimental g_1 from the model value which is derived from the deviation of the experimental polarized counts from the corresponding simulated counts.

1508 **Chapter 5**

1509 **Systematic Uncertainties**

1510 There is always a possibility that the final result(s) produced from any data analysis
1511 will be shifted from the true or ideally expected value(s) because the final result(s) are
1512 derived using the measured, modeled or estimated values of one or more other input
1513 parameters, whose values themselves usually have some systematic measurement or
1514 estimation uncertainties.

1515 The systematic effects due to a particular variable are studied by making a small
1516 change in the variable while holding the others constant, and measuring by how much
1517 the end result(s) changed.

1518 In this analysis, ten sources of systematic uncertainties are studied as listed below:

- 1519 1. Possible Uncertainty in the overall scaling factor
- 1520 2. Effect due to the contaminations from polarized H in the target and from
1521 misidentified π^- in the scattered electrons sample.
- 1522 3. Potential deviations in the reconstructed kinematics
- 1523 4. Possible uncertainty in the CC-inefficiency estimation
- 1524 5. Effect due to the e^+e^- pair symmetric contamination
- 1525 6. Possible uncertainty in the estimation of radiation lengths
- 1526 7. Model variation using preliminary version (v1) of A_1 model by Guler/Kuhn
1527 (2008-9)
- 1528 8. Model variation using old version of A_2 resonance model
- 1529 9. Model variation of F_2 (and proportionally of F_1) while keeping R constant

1530 10. Model variation of R or F_1 (with F_2 unchanged)

1531 For the ease of description later on, these ten components will be referred to by the
1532 index "k" with its value indicating the position in the list. So, the uncertainty due
1533 to scaling factor will be identified with k=1 and so on.

1534 5.1 Evaluation of Experimental Systematics

Possible Uncertainty due to the overall scaling factor This uncertainty is due to the uncertainties in the overall scaling factor (SF), which is a convolution of various unmeasured constants such as $P_b P_t$, packing fraction etc (see Sec. 4.1.1). This contribution is estimated by assuming that the uncertainties in SF is not more than 10%. Thus considering the worst case scenario of 10% uncertainty in SF, we estimate the corresponding uncertainty in g_1 as follows:

$$\Delta g_1^{SF}(W, Q^2) = g_1^{std}(W, Q^2) + \frac{\Delta n^{data}(W, Q^2) - 1.1 \cdot \Delta n^{std}(W, Q^2)}{1.1 \cdot B(W, Q^2)} - g_1^{data}(W, Q^2) \quad (5.1)$$

1535 with "std" shorthand used for "standard" model or the corresponding simulation
1536 i.e. the ones provided by RCSLACPOL when the asymmetry A_1 was not artificially
1537 increased to $A_1 + 0.1$. Here, Δn^{data} and Δn^{std} represent the polarized count dif-
1538 ferences for the experimental and simulated (without artificially changing A_1) data
1539 respectively.

Uncertainty from Polarized H in target and π^- contaminations This contribution from polarized H in target and π^- contamination is evaluated as follows,

$$\Delta g_1^{cont}(W, Q^2) = g_1^{std}(W, Q^2) + \frac{\Delta n^{data}(W, Q^2) \cdot 1.025 - \Delta n^{std}(W, Q^2)}{B(W, Q^2)} - g_1^{data}(W, Q^2) \quad (5.2)$$

1540 where we assume that the contamination is not more than 2.5%, which is consistent
1541 with what was found from our own study of the contamination.

Possible uncertainty in the beam energy measurement This contribution is evaluated assuming the uncertainty in beam energy measurement is not more than 10 MeV, so either the experimental data or the standard-simulation data can be analyzed assuming the beam energy was different by 10 MeV. In this analysis, the simulated data was analyzed assuming that the beam energy was 10 MeV more than that used during the event generation or simulation which was the same as that used

for analyzing the experimental data. For example, for the lower beam energy data set, 1339 MeV was used to analyze the experimental data as well as to simulate the corresponding data, but during the analysis of the simulated data, the energy value used was 1349 MeV. Here, the change in energy results in changes in both Q^2 and W .

$$\Delta g_1^{Eb}(W, Q^2) = g_1^{std}(W, Q^2) + \frac{\Delta n_{data}^{std}(W, Q^2) - \Delta n_{Eb+}^{std}(W, Q^2)}{B(W, Q^2)} - g_1^{data}(W, Q^2) \quad (5.3)$$

where Δn_{Eb+}^{std} is now the simulated Δn^{std} obtained by analyzing the data from the standard simulation as usual but with a beam energy that was 10 MeV more than the standard value.

Possible uncertainty in the CC-inefficiency estimation This contribution is estimated by assuming a maximum of 50% uncertainty in the estimated inefficiency as follows: The the 50% error is justified because the uncertainty in inefficiency is no more than 50% for $nphe > 2.5$ (see Fig. 3.31).

$$\Delta g_1^{Eb}(W, Q^2) = g_1^{std}(W, Q^2) + \frac{\Delta n_{data}^{std}(W, Q^2) - \Delta n_{0.5CCi}^{std}(W, Q^2)}{B(W, Q^2)} - g_1^{data}(W, Q^2) \quad (5.4)$$

where $\Delta n_{0.5CCi}^{std}$ is now the simulated Δn^{std} obtained after applying 50% more inefficiency instead of the actually estimated value. This considers the worst case scenario of 50% inefficiency and evaluates the corresponding systematic uncertainty to be the deviation of the extracted quantity from the one that would be obtained when there were to be a 100% efficiency.

Possible uncertainty due to e^+e^- pair symmetric contamination The contribution due to e^+e^- pair symmetric contamination is calculated as follows:

$$\Delta g_1^{Eb}(W, Q^2) = g_1^{std} + \frac{\Delta n_{data}^{std} \cdot \frac{1}{1+f(e^+e^-)} - \Delta n^{std}}{B(W, Q^2)} - g_1^{data}(W, Q^2) \quad (5.5)$$

where $f(e^+e^-)$ is the fraction of electrons in a given bin that come from pair-symmetric e^+e^- produced as estimated with EG1b fit by N. Guler [22] (used the closest available energies).

Radiative correction uncertainty Here, we need to change the parameter that most influences radiative corrections i.e., the number of radiation lengths before (RADB) and after (RADA) the scattering. By increasing both numbers by 10%, we should have a safe upper limit on practically all uncertainties coming from the

radiative procedure itself. But, to simplify the situation, we increased the RADA parameter in RCSLACPOL by 20% and repeated the full-statistic simulation. As a result, this particular contribution to the systematic uncertainty in a given kinematic bin is calculated as:

$$\Delta g_1^{rad}(W, Q^2) = g_1^{std} + \frac{\Delta n^{data}(W, Q^2) - \Delta n^{rad}(W, Q^2)}{B(W, Q^2)} - g_1^{data}(W, Q^2) \quad (5.6)$$

where the proportionality factor $B(W, Q^2)$ for the bin is exactly the same as that used to calculate g_1 earlier.

5.2 Model uncertainties

The remaining four components in the total systematic uncertainty (the last four in the list 5) account for the model uncertainty contributions. For this purpose, we changed the values of two of the model parameters “AsymChoice” and “SFchoice” (each takes value of 11, in the standard case)

We repeated the full statistics simulation four more times by changing the values of two RCSLACPOL parameters “AsymChoice” and “SFchoice” (which controls the values of model asymmetries and the structure functions, with each taking a value of 11 in the standard case) one by one corresponding to the following four model variations:

1. Variation-1: AsymChoice=12, SFchoic=11
2. Variation-2: AsymChoice=15, SFchoic=11
3. Variation-3: AsymChoice=11, SFchoic=12
4. Variation-4: AsymChoice=11, SFchoic=13

where, the different values of the two RCSLACPOL parameters correspond to the following model choices:

1. **AsymChoice** values are used to determine specific A_1/A_2 models used in the RCSLACPOL program
 - (a) 11: Standard Resonance Model 2008-9 Guler/Kuhn (**Used for standard simulation**)
 - (b) 12: Variation of A_1 model (earlier fit)
 - (c) 15: Variation of A_2 resonance model: Vary the virtual photon asymmetry A_2 in the resonance region within its fit uncertainties.

1578 2. **SFchoice** values are used to determine specific F_1/F_2 models.

- 1579 (a) 11: 2009 version of $F_1^n/F_1^p/F_1^d$ by Peter Bosted/Eric Christie 2009, HER-
- 1580 MES (**Used for standard simulation**) (with d in F_1^d denoting a deuteron).
- 1581 (b) 12: Same version as 11, but with fit uncertainties added to F_2 (and pro-
- 1582 portionally F_1)
- 1583 (c) 13: Same version as 11, but with fit uncertainties subtracted from R (F_2
- 1584 unchanged)

After the simulation data for the above four cases (see 5.2) were available, four more data tables (TM1,TM2,TM3 and TM4) were produced for the corresponding model values of g_1 , A_1 , F_1 etc. Then, the contributions to the systematic uncertainty from each of these four cases of model variation were given as follows:

$$\Delta g_1^i(W, Q^2) = g_1^{std}(W, Q^2) + \frac{\Delta n^i(W, Q^2) - \Delta n^{std}(W, Q^2)}{B(W, Q^2)} - g_1^i(W, Q^2) \quad (5.7)$$

1585 with “i” indicating any of the four cases of model variation, g_1^i being the model
 1586 prediction for the i^{th} case as obtained from the corresponding data table “TMi” and
 1587 the proportionality factor $B(W, Q^2)$ again being exactly the same as used to calculate
 1588 g_1 as earlier.

1589 5.3 Combining uncertainties

1590 Contributions from the 10 individual components are estimated and then a total
 1591 contribution is estimated by first combining the corresponding individual components
 1592 for each of the two beam energies and finally combining them all by calculating the
 1593 RMS of the ten combined contributions.

1594 In principle, each of the individual contributions to the systematic uncertainty can
 1595 also be combined using the same equations as for combining g_1 and $A_1 F_1$ (see above).
 1596 However, we must be careful to distinguish between correlated and uncorrelated un-
 1597 certainties. If for a given (W, Q^2) bin, data is available only from one beam energy,
 1598 then combined uncertainty for the k^{th} component is simply the uncertainty from that
 1599 beam energy. If there are measurements from both beam energies, we combine them
 1600 with statistical weights as follows:

- 1601 1. The variations due to scale factor (k=1), beam energy (k=3) and CC-efficiency
 1602 (k=4) are all un-correlated and, therefore, added in quadrature as follows:

$$\delta g_1(k=8,10,11, \text{combined}) = \sqrt{\left(\sum_i \frac{(\delta g_1)^2(i)}{(\Delta g_1)^2(i)} \right) / \text{Sum2}} \quad (5.8)$$

1603 where, δ represents the k^{th} component of the systematic uncertainty, whereas,
 1604 'Sum2', 'i' and Δ have the same meanings as before, with 'Sum2' given by

$$Sum2 = \sum_i \frac{1}{(\Delta g_1)^2(i)} \quad (5.9)$$

1605 which provides the statistical weight, where the index 'i' represents two beam
 1606 energy (1.3 and 2.0 GeV) data sets, and Δg_1 indicates the statistical uncertainty
 1607 in g_1 in the corresponding kinematic bin.

- 1608 2. All other variations are correlated between the two beam energies and should
 1609 be averaged linearly (WITH sign):

$$\delta g_1(\text{other } k, \text{ combined}) = \left(\sum_i \frac{(\delta g_1)(i)}{(\Delta g_1)^2(i)} \right) / Sum2 \quad (5.10)$$

1610 Once each of the k^{th} component of the systematic uncertainties are combined
 1611 between the two beam energies, we then proceed to combine them all to get a grand
 1612 total. This is done by simply adding the ten E_b -combined systematic uncertainties in
 1613 quadrature and taking the square-root of the sum as follows:

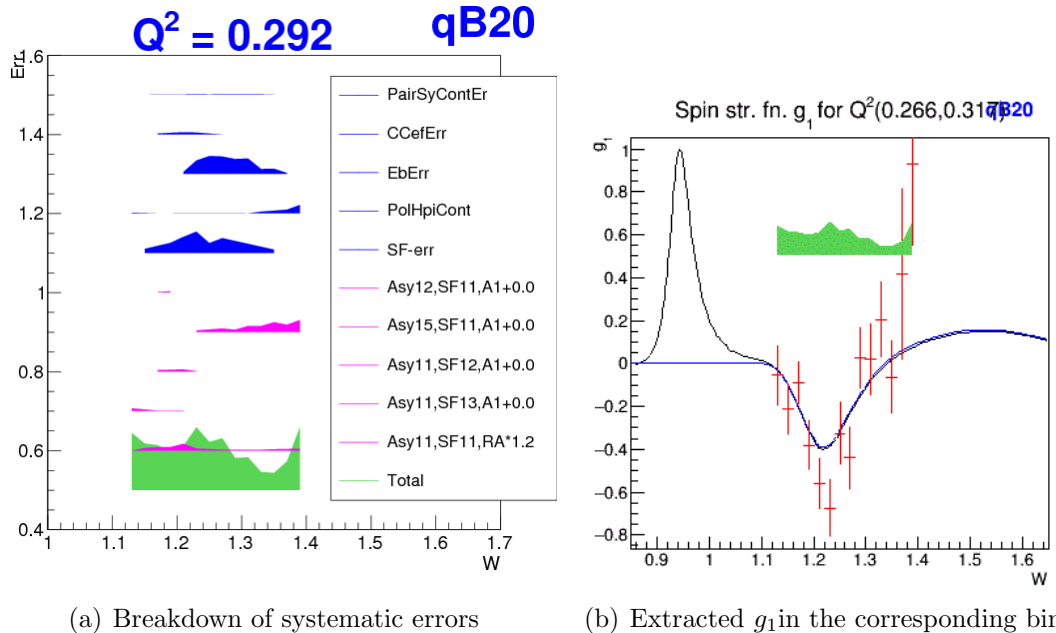
$$TotalSystematicUncertainty = \sqrt{\sum_{k=1}^{10} (\Delta g_1)_k^2} \quad (5.11)$$

1614 Figs. (5.2 and 5.3) show, for example, the different components of the systematic
 1615 uncertainties along with the grand total on g_1 (from 1.3 GeV data) evaluated in the
 1616 manner just outlined. Likewise, Figs. (5.4 and 5.5) show similar plots for the 2.0
 1617 GeV data.

1618 These ten different components of systematic uncertainties on g_1 and similarly on
 1619 $A_1 F_1$ thus calculated separately for both beam energies are later combined as described
 1620 below.

1621 5.3.1 Combining data from the two beam energies

1622 Once the data g_1 and $A_1 F_1$ and their corresponding uncertainties are evaluated from
 1623 each beam energy data set, they are combined as follows [26] (to make the descrip-
 1624 tion simple, the procedure is described only for g_1 , but, in the end, the exact same
 1625 procedure is followed for $A_1 F_1$ as well):



(a) Breakdown of systematic errors

(b) Extracted g_1 in the corresponding bin

FIG. 5.1. On the left: various components of systematic uncertainty (see Sec. 5 on g_1 vs W in a Q^2 bin (1.3 GeV data). The band width represents the size of the uncertainties. The vertical position of each band has no physical meaning (arbitrarily chosen for the convenience of display). The first five (blue) bands are the contributions due to e^+e^- -contamination , CC-inefficiency , uncertainties in beam energy measurement , polarized background (H, π^- etc) and scaling factor uncertainties respectively. The first (top) magenta band is the contribution due to the uncertainties in the radiative corrections , next four (magenta) are due to model uncertainties and the last (green) one is the total uncertainty after properly combining all components. For similar plots in other Q^2 bins see Figs. 5.2 and 5.3. On the right: extracted g_1 vs W shown along with the total systematic uncertainty.

- 1626 1. First a table is made, separately for each beam energy, of all (Q^2, W) bins
1627 with calculated values of g_1 , their statistical uncertainties and each of the ten
1628 components of the systematic uncertainties (making sure to keep the correct
1629 signs of the systematic changes).
- 1630 2. Then another table is made for the combined values of g_1 , which are evaluated
1631 as follows:
 - 1632 (a) If for a given (W, Q^2) bin, g_1 comes only from one beam energy, then all
1633 the entries from that energy go into the "combined" table
 - 1634 (b) If g_1 has measurements from both beam energies, we combine them with

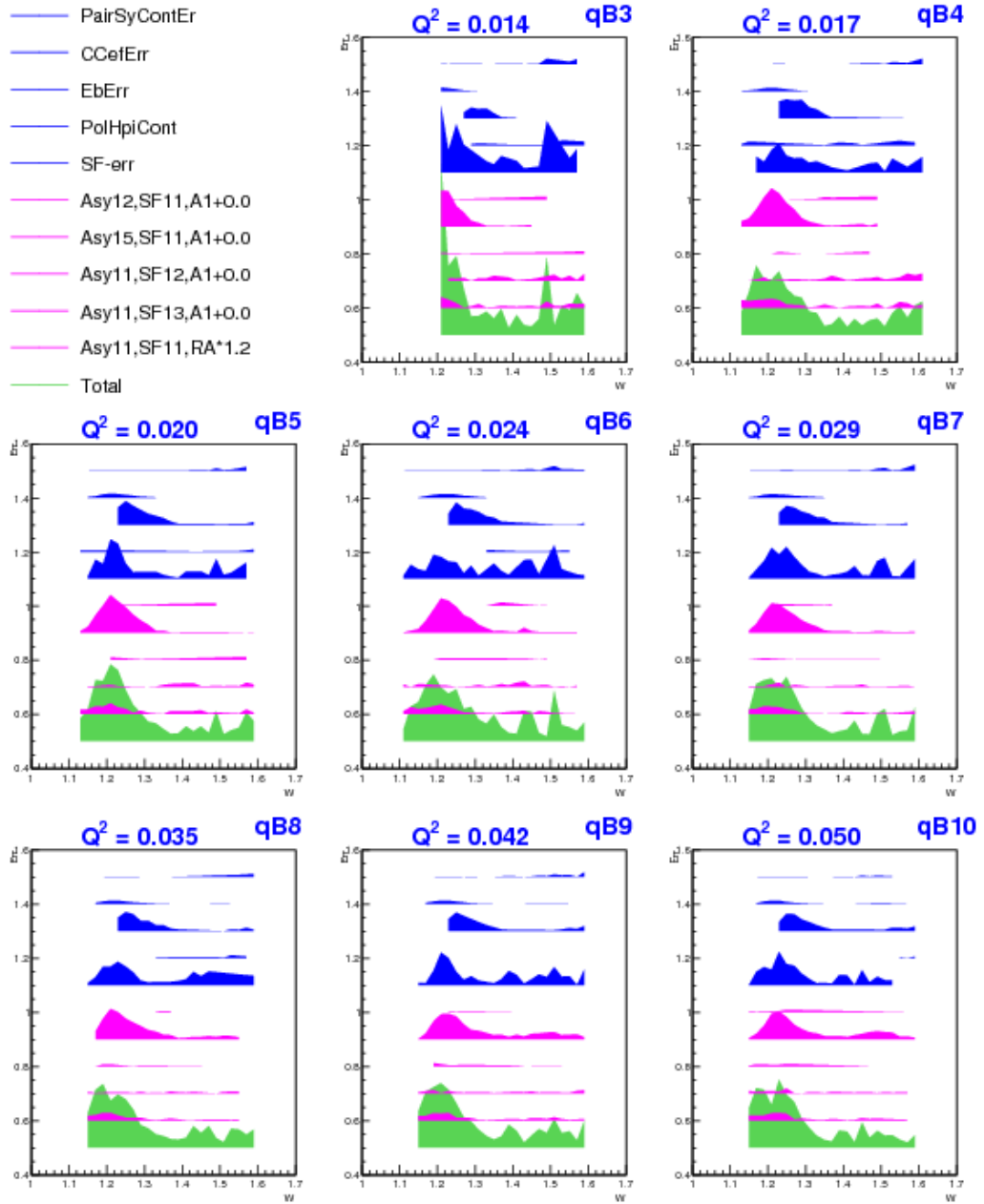


FIG. 5.2. Plots like that shown in Fig. 5.1 showing various components of systematic uncertainty on g_1 vs W in different Q^2 bins for 1.3 GeV data.

$$Sum1 = \sum_i \frac{g_1(i)}{(\Delta g_1)^2(i)} \quad (5.12)$$

$$g_1(combined) = Sum1/Sum2 \quad (5.13)$$

$$\sigma g_1(combined) = \sqrt{1/Sum2} \quad (5.14)$$

1636 where the index 'i' represents two beam energy (1.3 and 2.0 GeV) data sets,
 1637 Δg_1 indicates the statistical uncertainty in g_1 and $Sum2$ is again given by
 1638 Eq. 5.12 above.

1639 Figures 5.6 and 5.8 show the breakdown of the total contribution to the systematic
 1640 uncertainty from different sources. We can see that the dominant contribution comes
 1641 from the uncertainties in the overall scale factor (the cyan band indicated with SF-err
 1642 in the legend) which is used to normalize the simulated data to make them comparable
 1643 with data. One of the big part of this uncertainty comes from those in $P_b P_t$ and target
 1644 size measurements. Next big contributions seem to come from the model (in particular
 1645 the model for the unmeasured A_2) and radiative corrections. Near the Δ -resonance
 1646 region, the effect of beam energy uncertainty also seems to be very pronounced. The
 1647 breakdown of the different components (but combined between the two beam energies)
 1648 of the total systematic uncertainties are also shown separately in the Figs. 5.6 and
 1649 5.8.

1650 It should be noted here that the same methods were used to calculate the system-
 1651 atic uncertainties on $A_1 F_1$ and on all integrals directly (i.e., they are not calculated
 1652 from propagated systematic uncertainties on g_1 or $A_1 F_1$ but directly from variations
 1653 of the integrals.

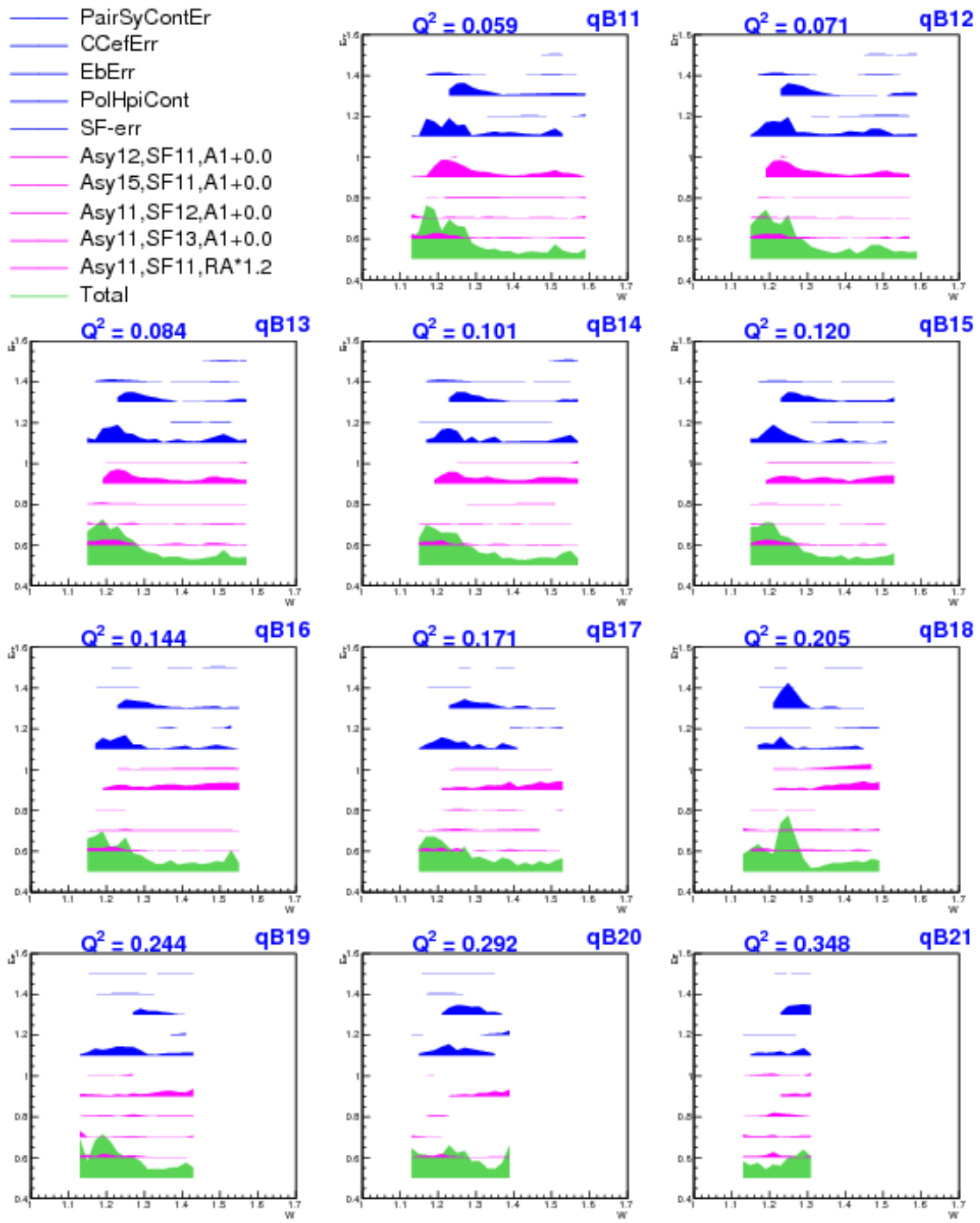


FIG. 5.3. Systematic uncertainty components in remaining Q^2 bins (continuation of Fig. 5.2).

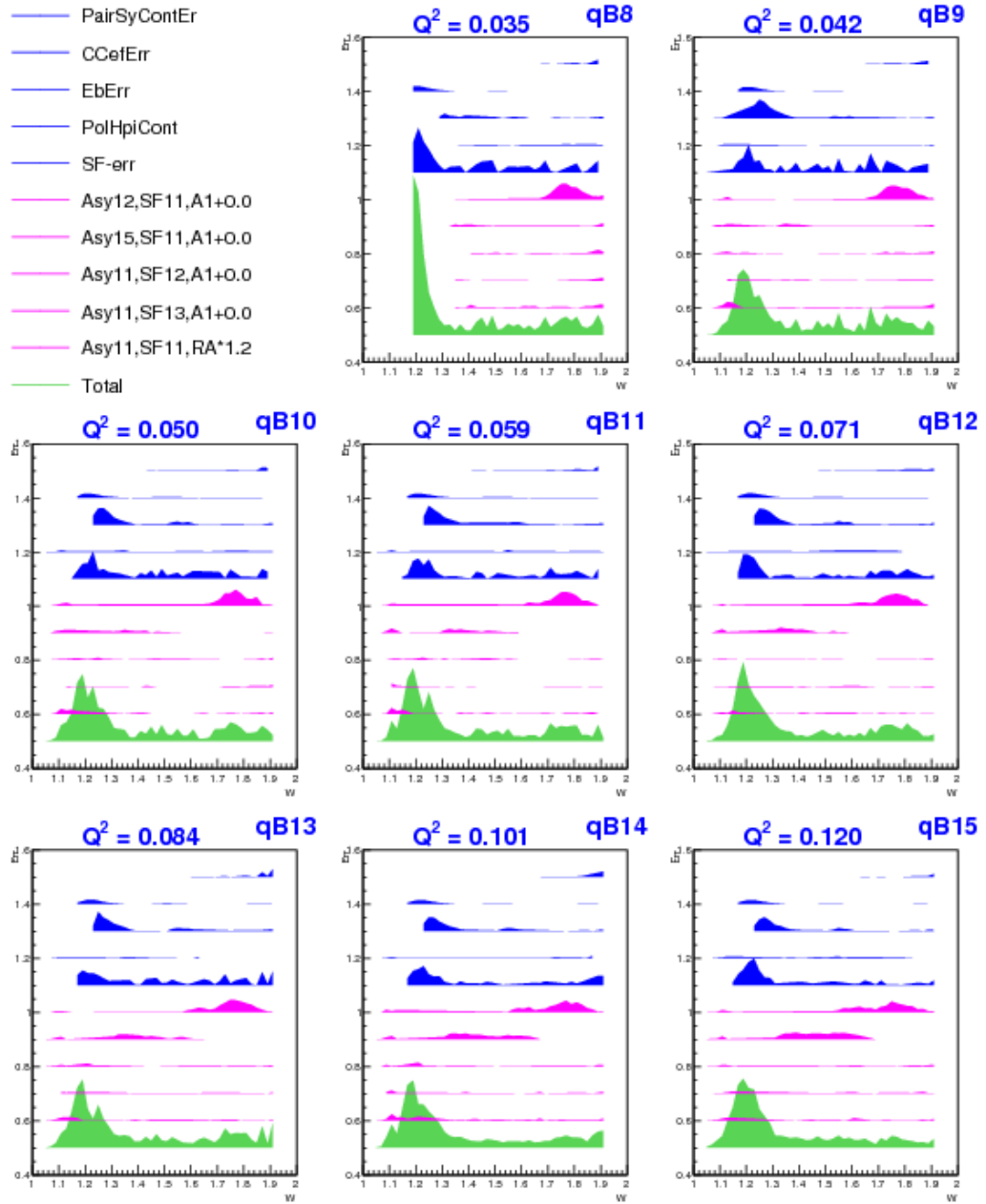


FIG. 5.4. Plots similar to those shown in Fig. 5.2 but for 2.0 GeV, showing various components of systematic uncertainty on g_1 vs W in different Q^2 bins.

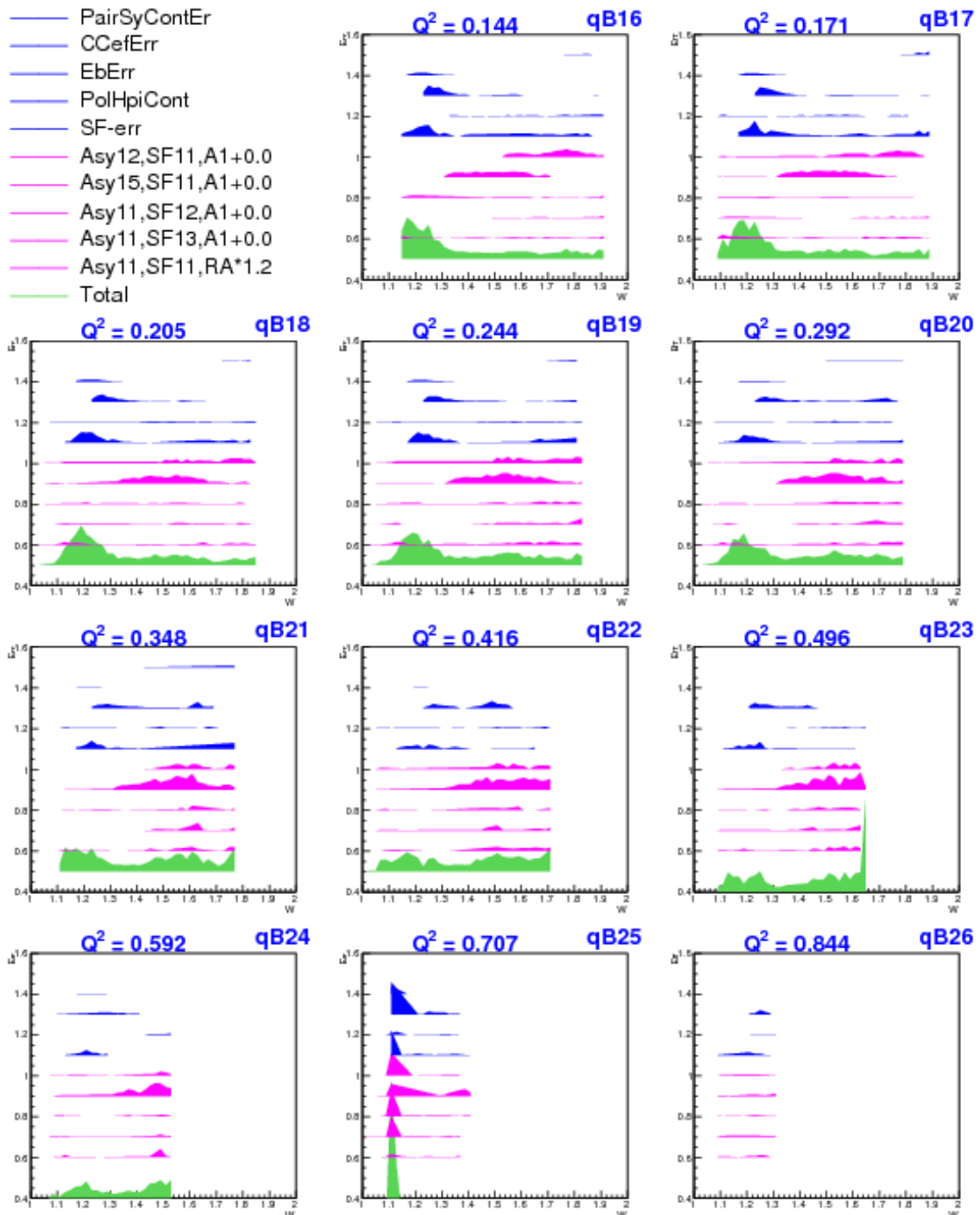


FIG. 5.5. Systematic uncertainty components in remaining Q^2 bins (continuation of Fig. 5.4).

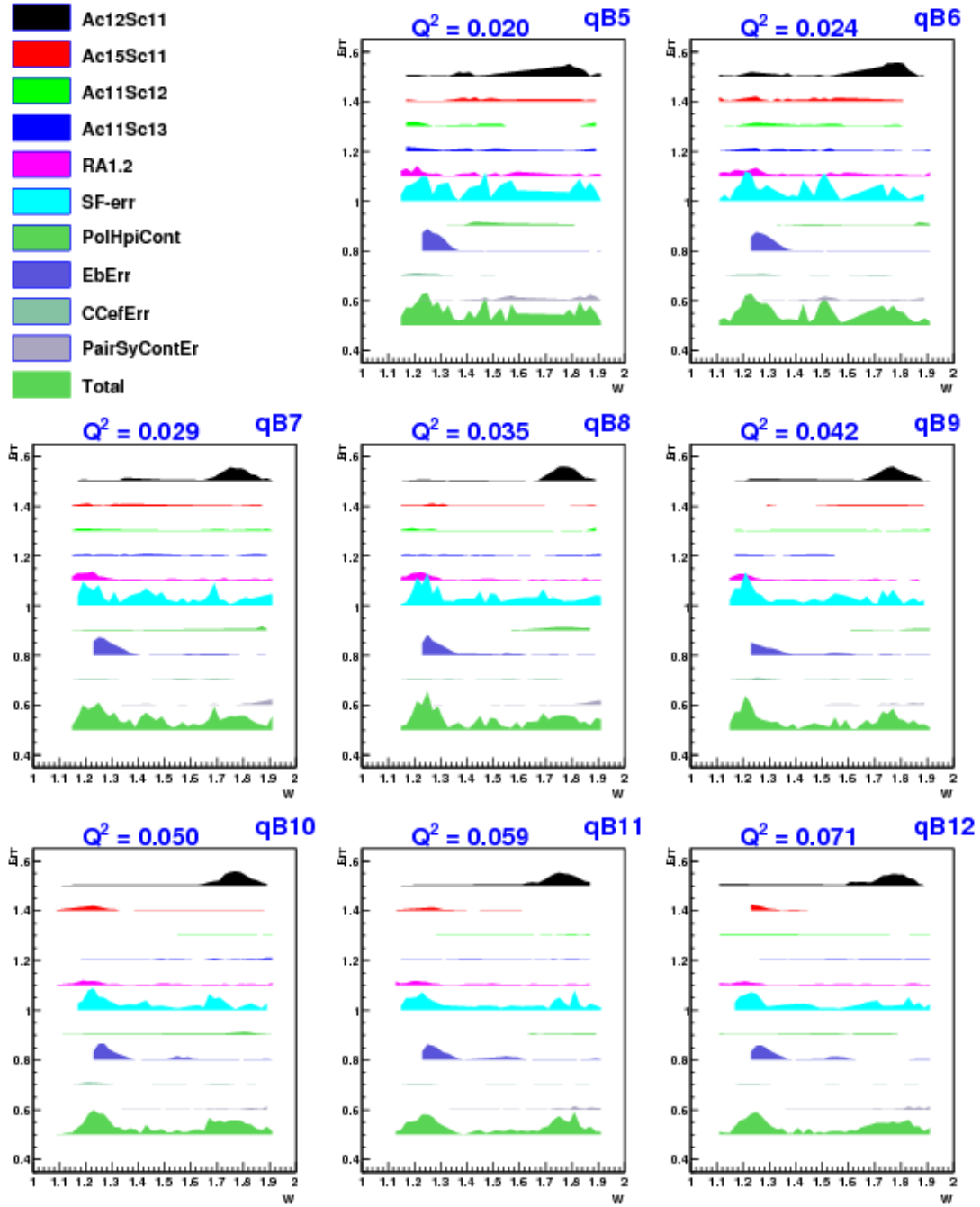


FIG. 5.6. Breakdown of systematic uncertainties in g_1 (after combining data from the two energy data sets) in the first few Q^2 bins. See Fig. 5.1 for the description of the different systematic uncertainty components.

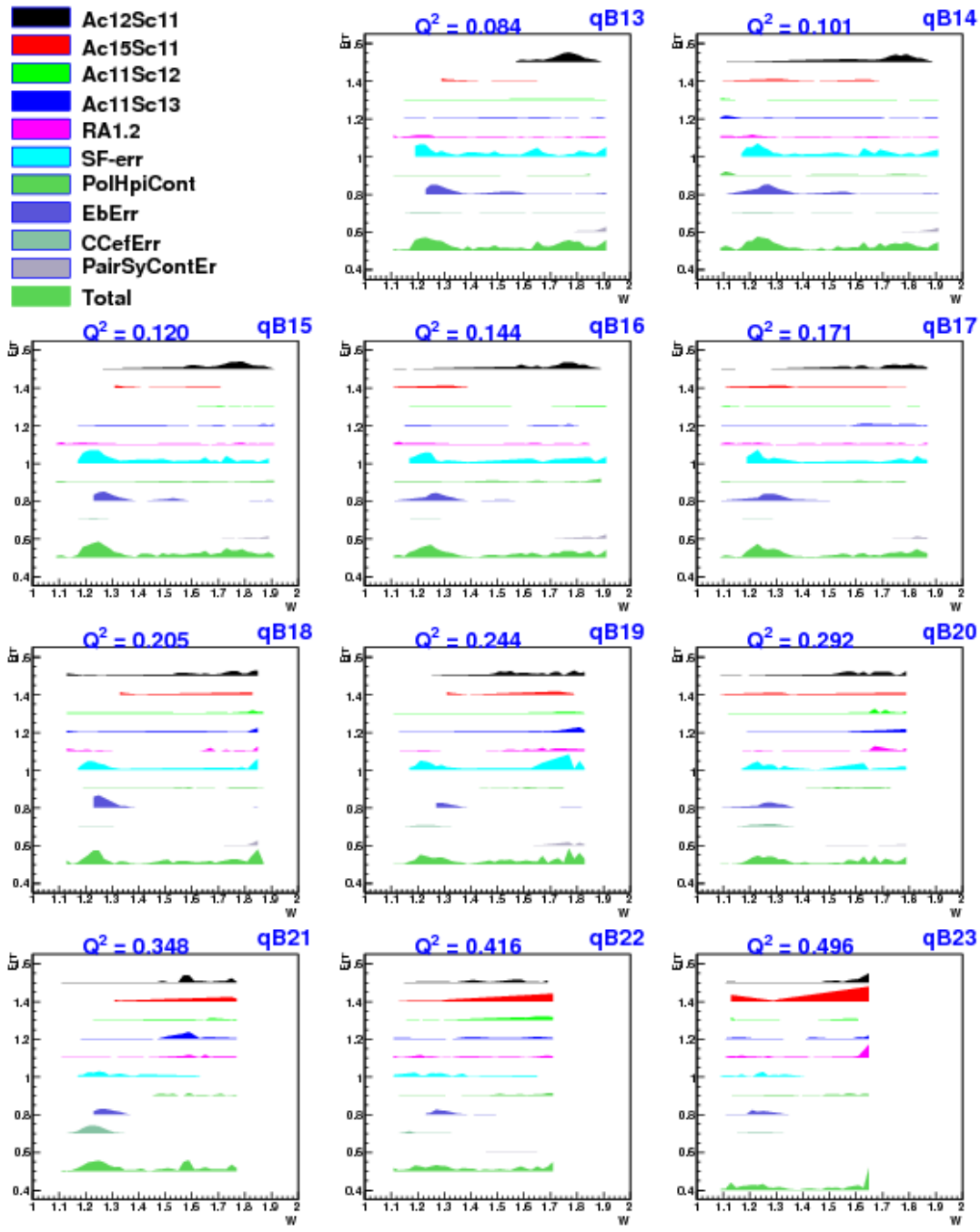


FIG. 5.7. Plots as in Fig. 5.6 but in the remaining higher Q^2 bins.

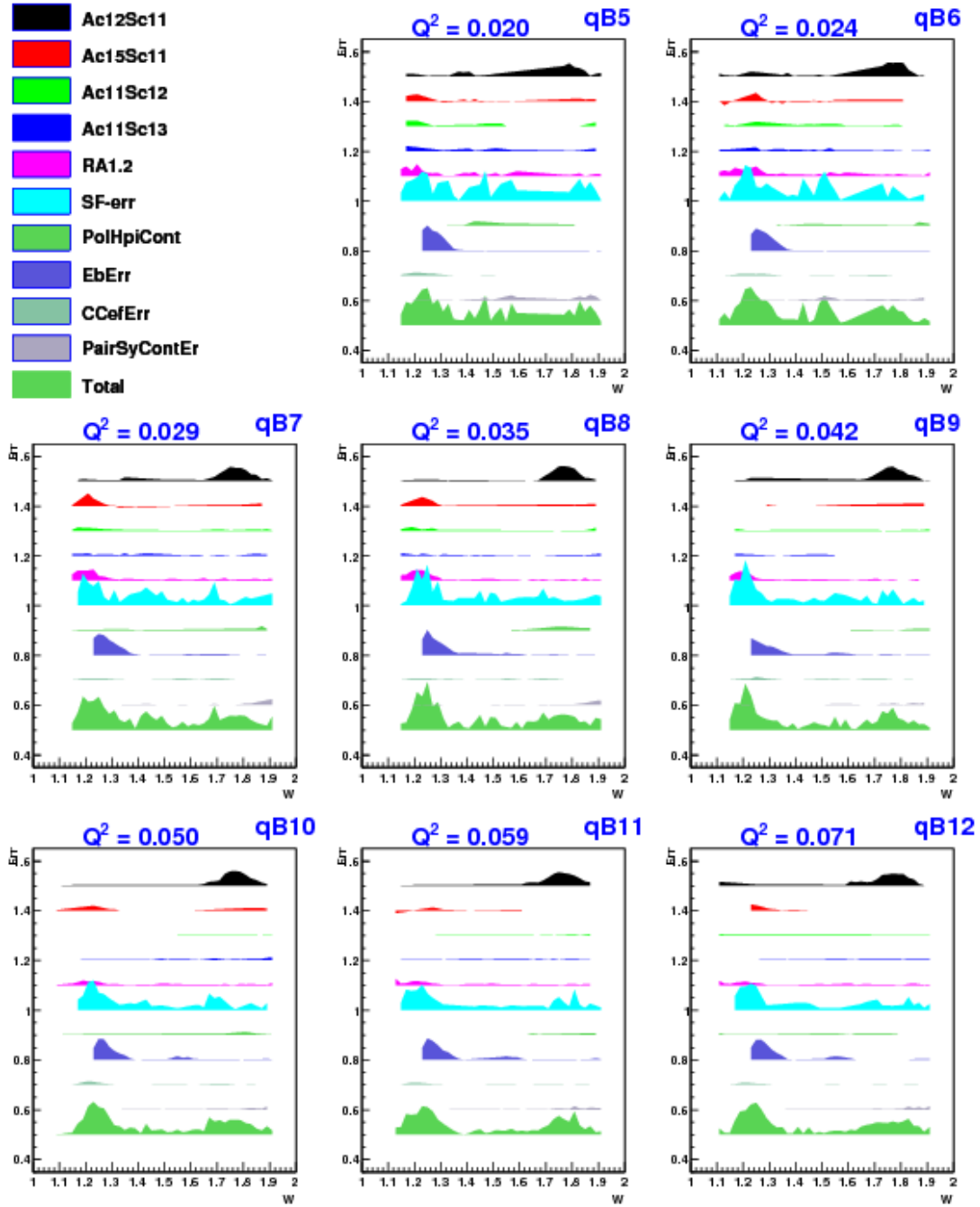


FIG. 5.8. Breakdown of systematic uncertainties in $A_1 F_1$ (after combining data from the two energy data sets) in the first few Q^2 bins. See Fig. 5.1 for the description of the different systematic uncertainty components.

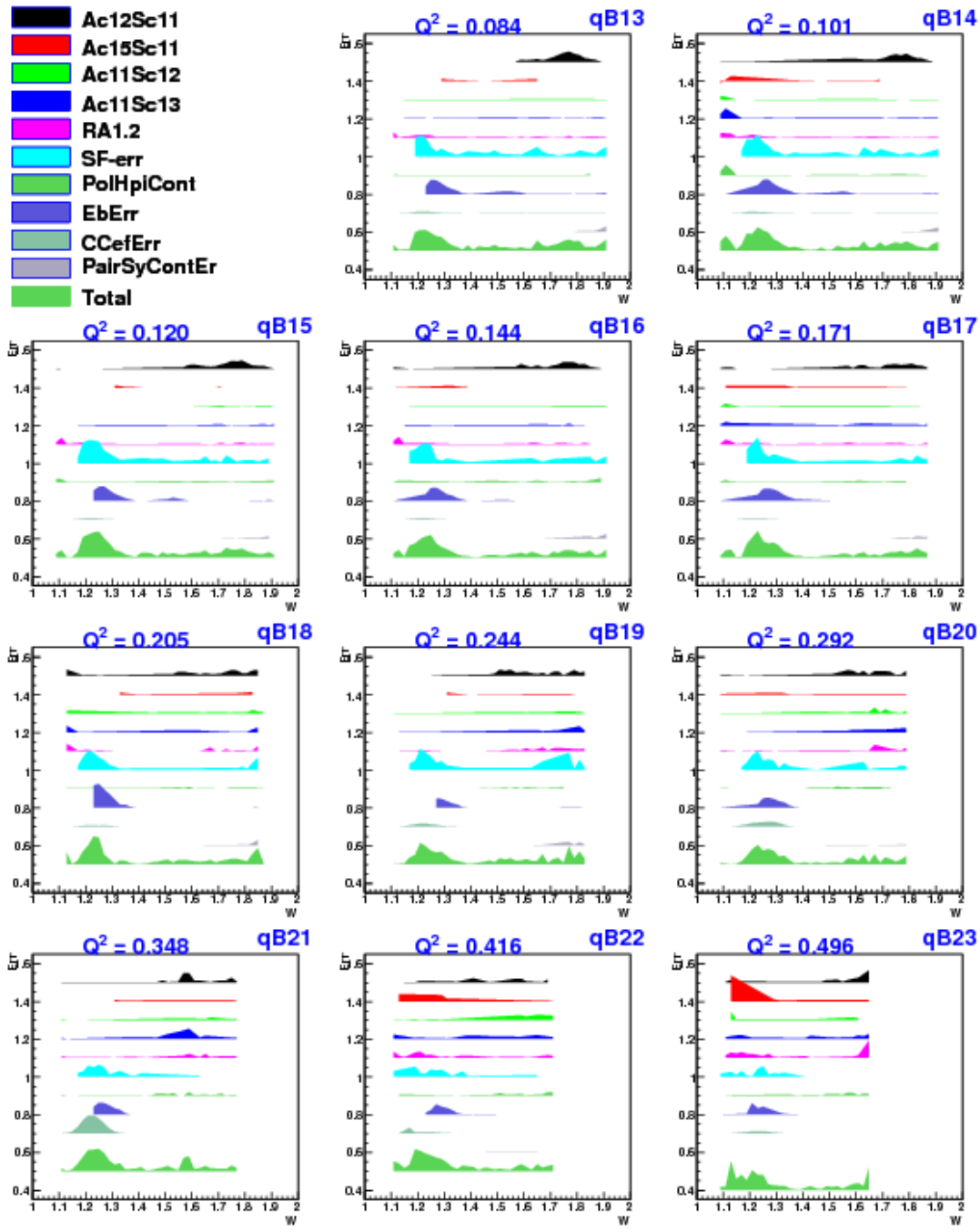


FIG. 5.9. Plots as in Fig. 5.8 but in the remaining higher Q^2 bins.

¹⁶⁵⁴ Chapter 6

¹⁶⁵⁵ Results

¹⁶⁵⁶ Two quantities - g_1 and $A_1 F_1$ and their uncertainties were extracted from the EG4
¹⁶⁵⁷ deuteron target data using the methods outlined in the previous chapter. This was
¹⁶⁵⁸ done in each of 21 Q^2 bins (between about 0.02 and 0.7 GeV 2 in Q^2) and several W
¹⁶⁵⁹ bins of size 20 MeV each. In the overlapping kinematic bins where both beam energy
¹⁶⁶⁰ data sets contributed, the results were further combined individually to arrive at a
¹⁶⁶¹ single set of energy independent data points. Finally, within each Q^2 bin, the newly
¹⁶⁶² extracted g_1 and $A_1 F_1$ values were used to evaluate three different integrals - Γ_1^d , \bar{I}_{TT} ,
¹⁶⁶³ and γ_0^d . All of these results are presented in the sections below.

¹⁶⁶⁴ 6.1 Extracted g_1 and $A_1 F_1$

¹⁶⁶⁵ Figures 6.1 and 6.2 show the extracted values of g_1 and their errors from two different
¹⁶⁶⁶ beam energies (1.337 GeV and 1.989 GeV). It can be seen that the two energies give
¹⁶⁶⁷ results that are in good agreement in the overlapping kinematic regions.

¹⁶⁶⁸ These results from low Q^2 measurements clearly show the resonant structure in
¹⁶⁶⁹ the region $W \leq 2.0$. Especially, the Δ -resonance stands out through its strongly
¹⁶⁷⁰ negative signal. In addition, in the second resonance region around $W=1.5$ GeV
¹⁶⁷¹ where $N^*(1520)$ and $N^*(1535)$ (also denoted by D_{11} and S_{13} respectively) overlap,
¹⁶⁷² we see a drastic transition of g_1 (or cross section) from strongly negative values
¹⁶⁷³ (not well described by the model because it is unconstrained there due to the lack
¹⁶⁷⁴ of experimental data) at low Q^2 to clearly positive values at high Q^2 indicating
¹⁶⁷⁵ that the dominance of the spin-flip helicity amplitude $A_{\frac{3}{2}}^T$ on cross section drastically
¹⁶⁷⁶ diminishes with Q^2 and the non-flip amplitude $A_{\frac{1}{2}}^T$ becomes stronger¹. We have
¹⁶⁷⁷ pushed the lower limit on Q^2 in the resonance region with reduced systematic and

¹The four virtual photoabsorption cross sections σ_T , σ_L , σ_{LT} , and σ_{TT} , are related to the four structure functions F_1 , F_2 , g_1 and g_2 of the target and as a result, g_1 can be expressed as $g_1 =$

₁₆₇₈ statistical errors that will contribute greatly to the world data set. Our data will
₁₆₇₉ help MAID and other phenomenological models to better constrain their parameters
₁₆₈₀ enabling them to make better predictions in the future.

$$\frac{MK}{8\pi^2\alpha(1+\gamma^2)}(\sigma_{\frac{1}{2}}^T - \sigma_{\frac{3}{2}}^T + 2\gamma\sigma_{LT})$$

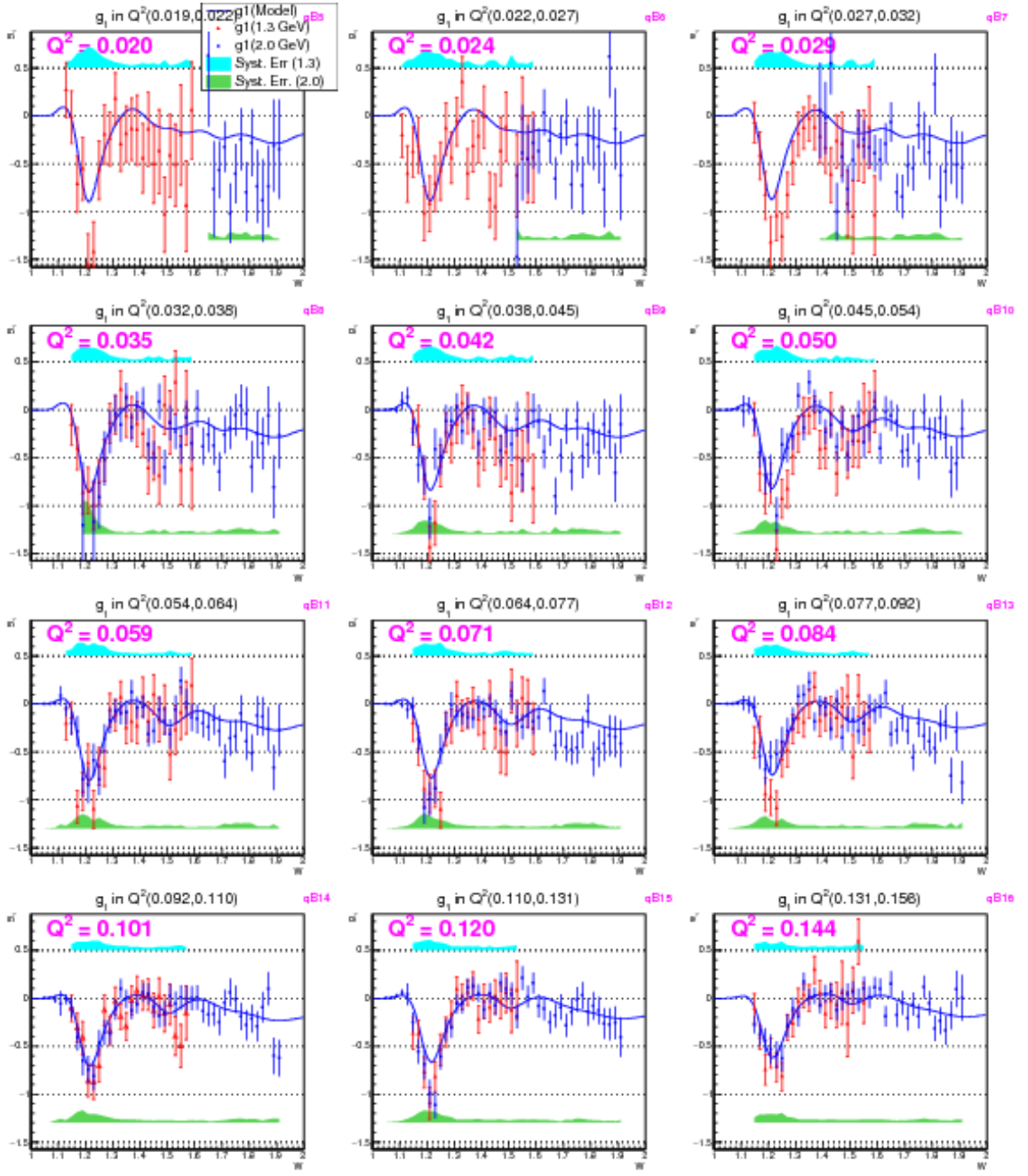


FIG. 6.1. Extracted g_1 for deuteron (in the first 12 Q^2 bins) from the two different beam energy data sets. The statistical errors are indicated by error bars, while the systematic uncertainties are given by the bands (cyan, top: 1.3 GeV and green, bottom: 2 GeV).

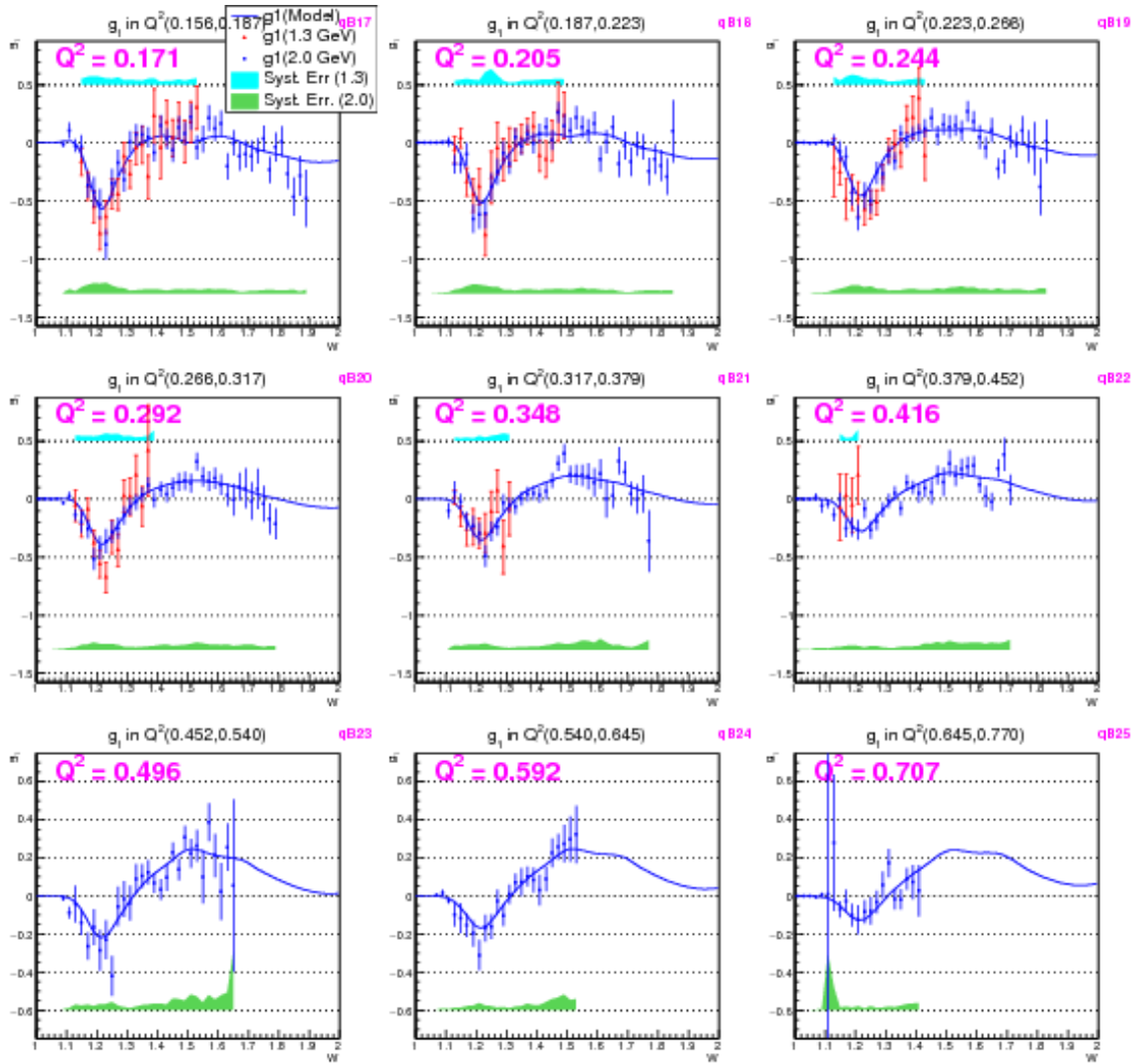


FIG. 6.2. Extracted g_1 for deuteron (in the last 9 Q^2 bins (see Fig. 6.1 for the first 12 bins)) from the two different beam energy data sets.

Likewise, Figs. 6.3 and 6.4 shows the extracted values of $A_1 F_1$ and their errors from two different beam energies (1.3 GeV and 2.0 GeV). These values also show similar behavior as g_1 .

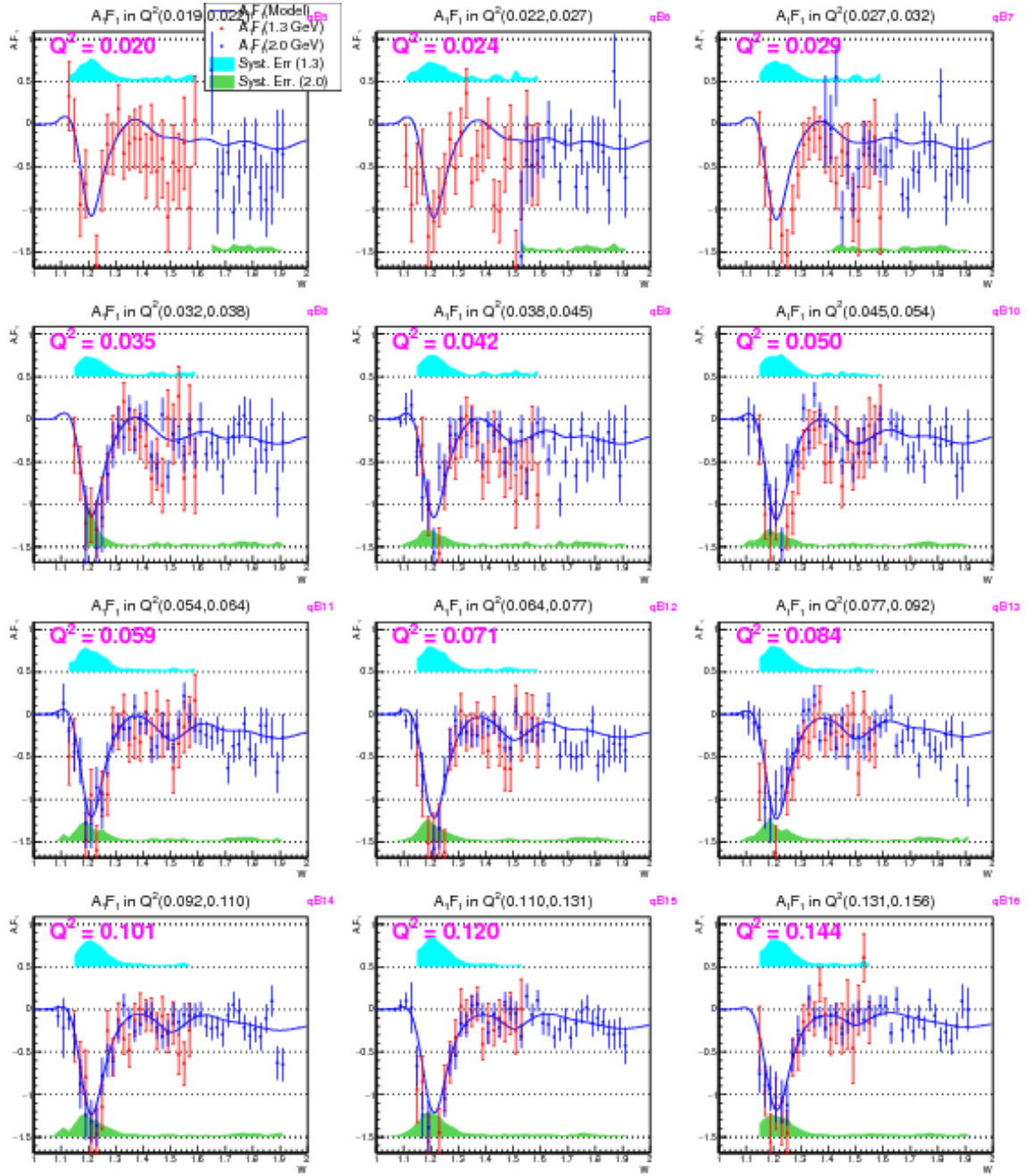


FIG. 6.3. Extracted $A_1 F_1$ for deuteron (in the first 12 Q^2 bins) from the two different beam energy data sets. The statistical errors are indicated by error bars, while the systematic uncertainties are given by the bands (cyan, top: 1.3 GeV and green, bottom: 2 GeV).

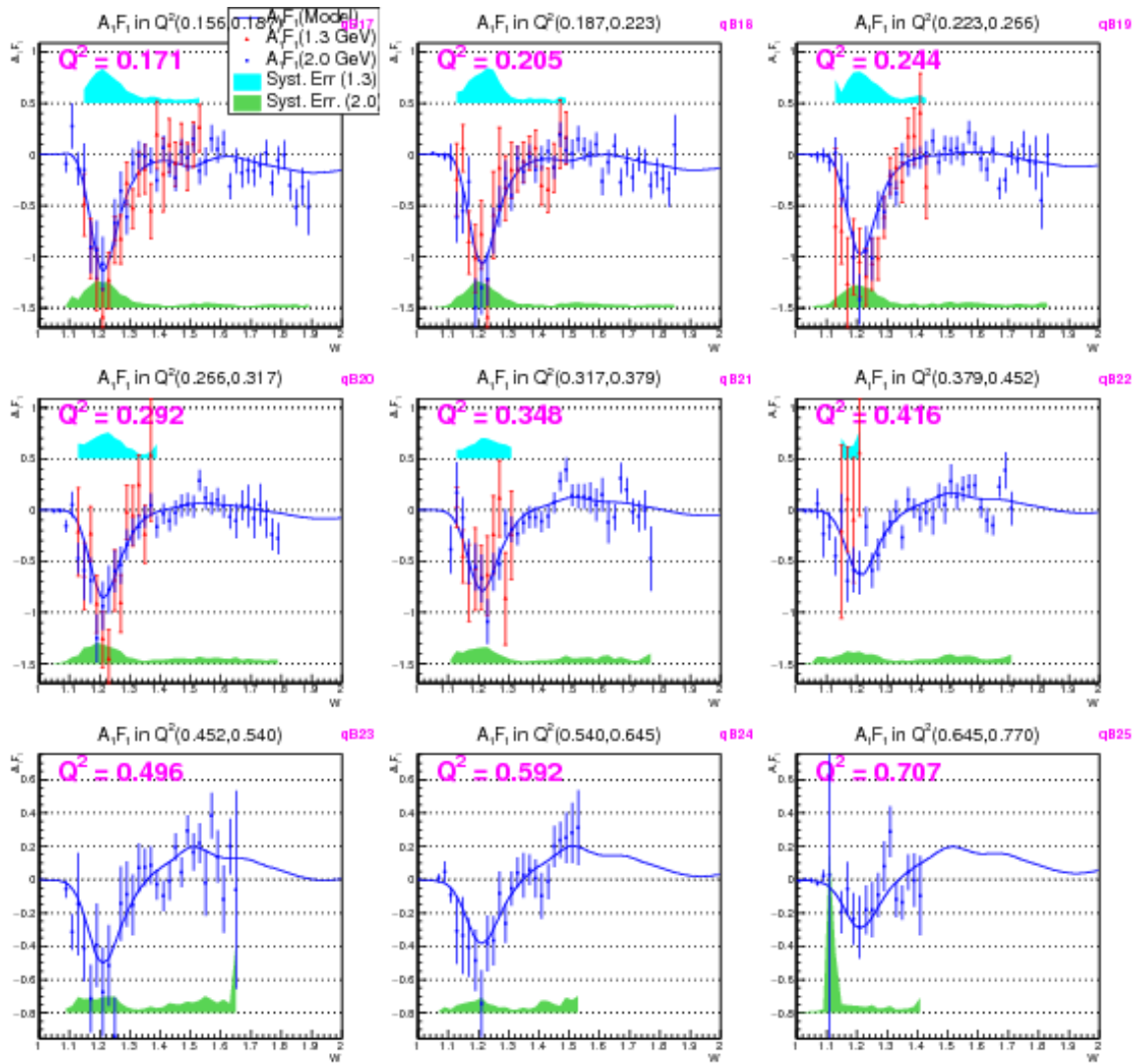


FIG. 6.4. Extracted $A_1 F_1$ for deuteron (in the last 9 Q^2 bins (see Fig. 6.3 for the first 12 bins)) from the two different beam energy data sets..

1684 Figures 6.5, 6.6, 6.7 and 6.8 show the values of g_1 and $A_1 F_1$ and their errors after
 1685 combining the corresponding results from the two different beam energies as described
 1686 in the previous chapter.

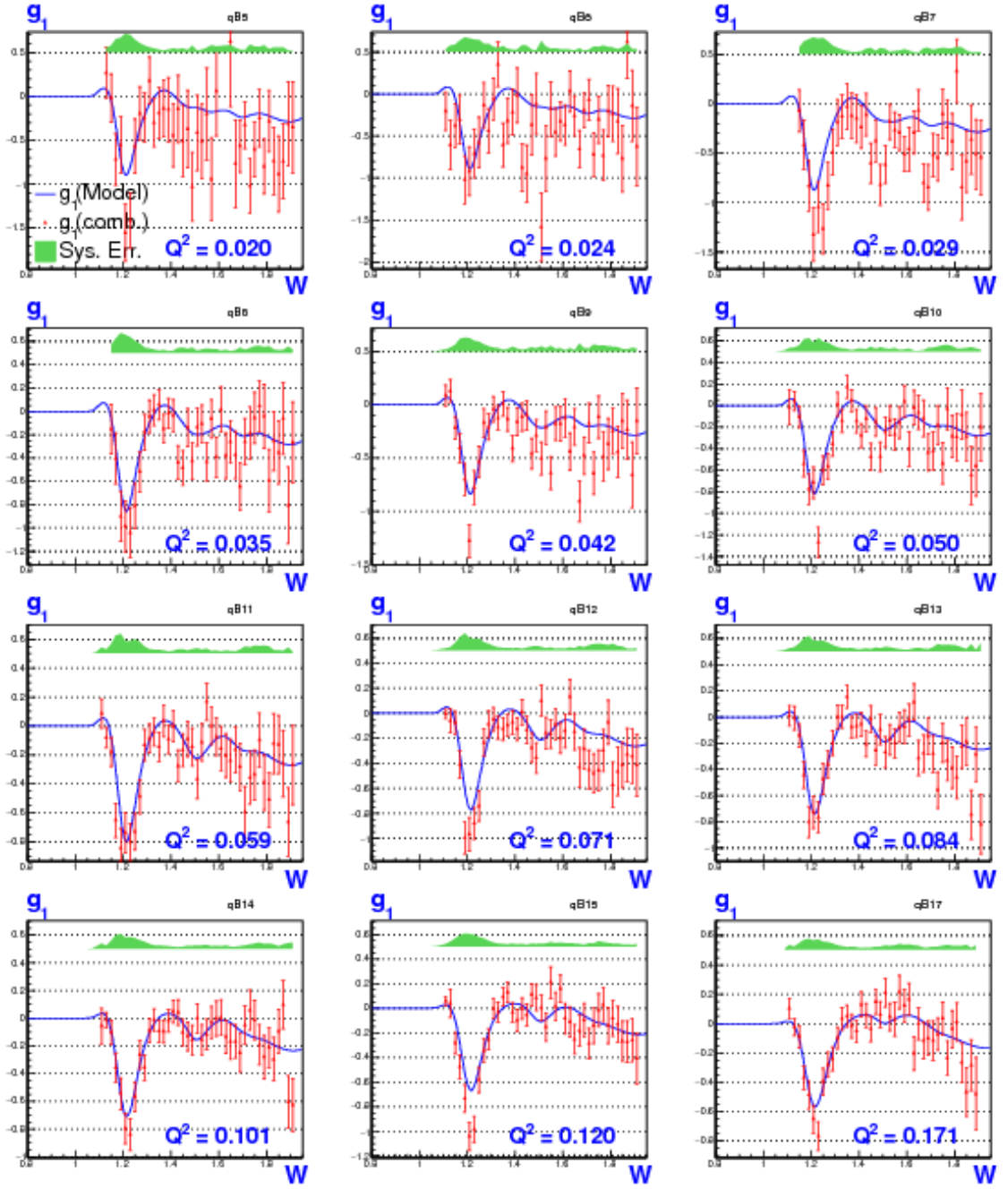


FIG. 6.5. Extracted g_1 for deuteron after combining the results from the two beam energies (in the first 12 Q^2 bins). The red data points with error bars in each of the panels are the combined extracted results, the blue continuous line is the used model of g_1 and the green band represents the corresponding total systematic errors.

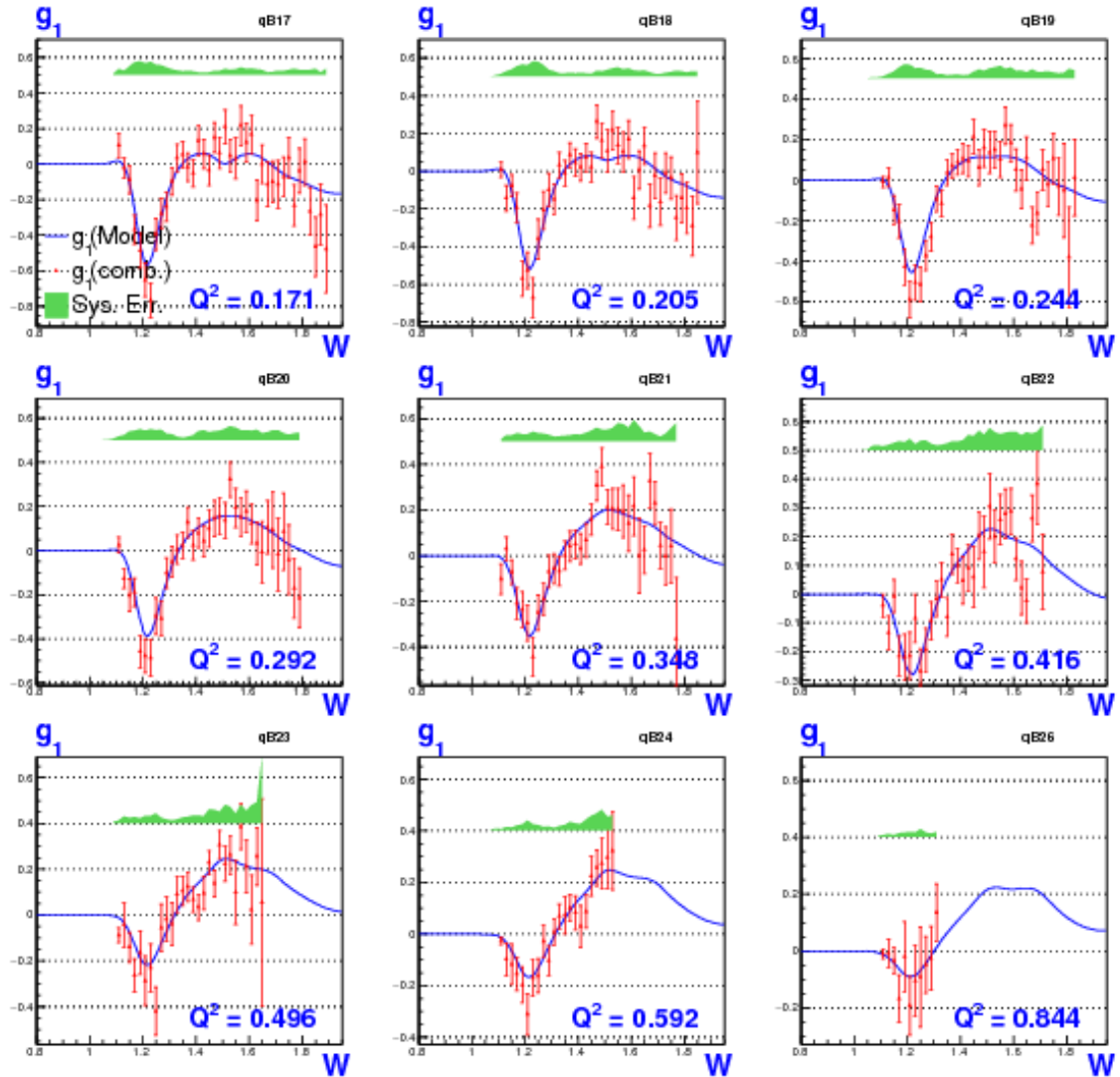


FIG. 6.6. Similar plots as in Fig. 6.5 showing the combined results on g_1 in the next 9 Q^2 bins.

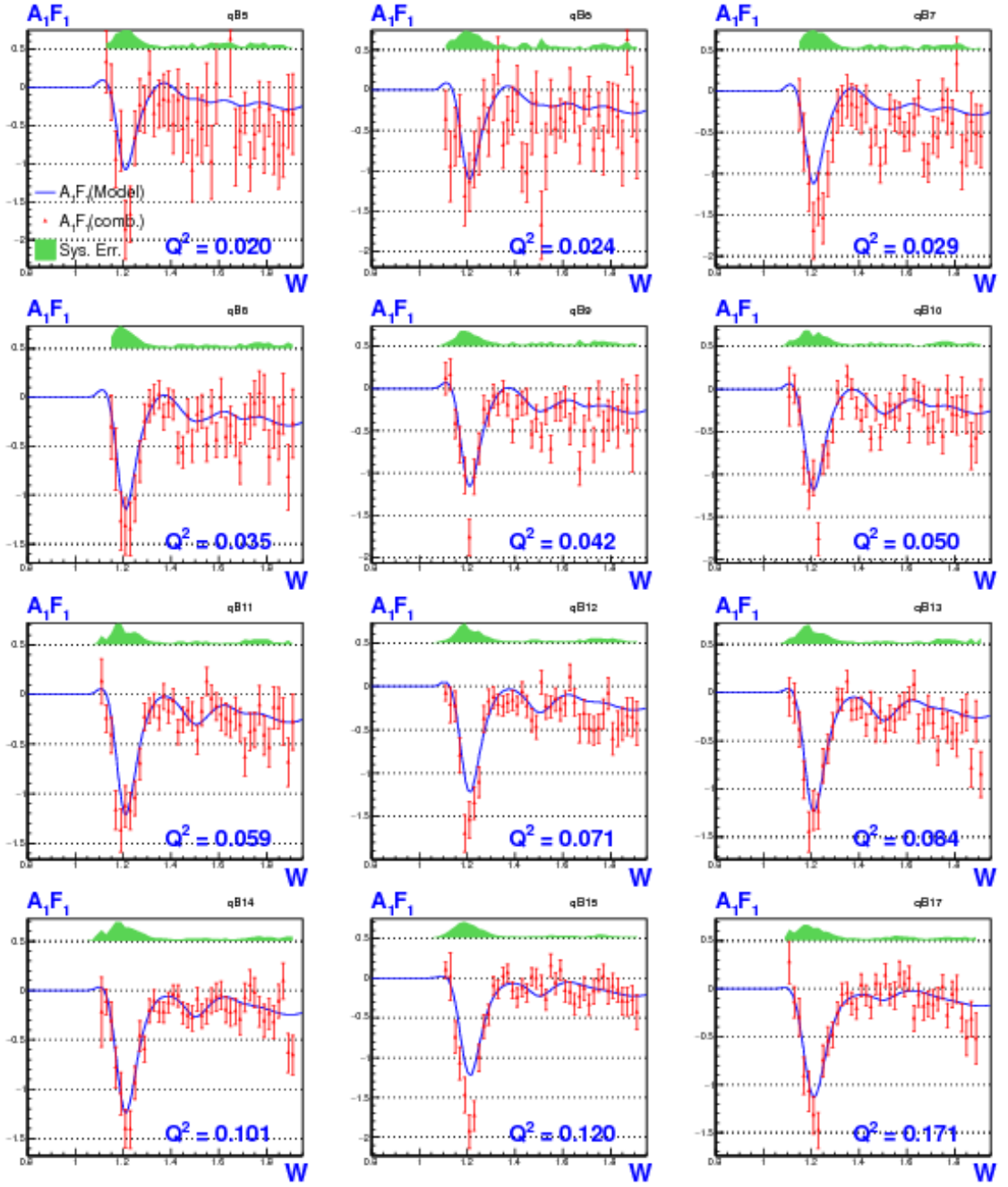


FIG. 6.7. $A_1 F_1$ after combining the results from the two beam energies (in the first 12 Q^2 bins). The red data points with error bars in each of the panels are the combined extracted results, the blue continuous line is the used model of g_1 and the green band represents the corresponding total systematic errors.

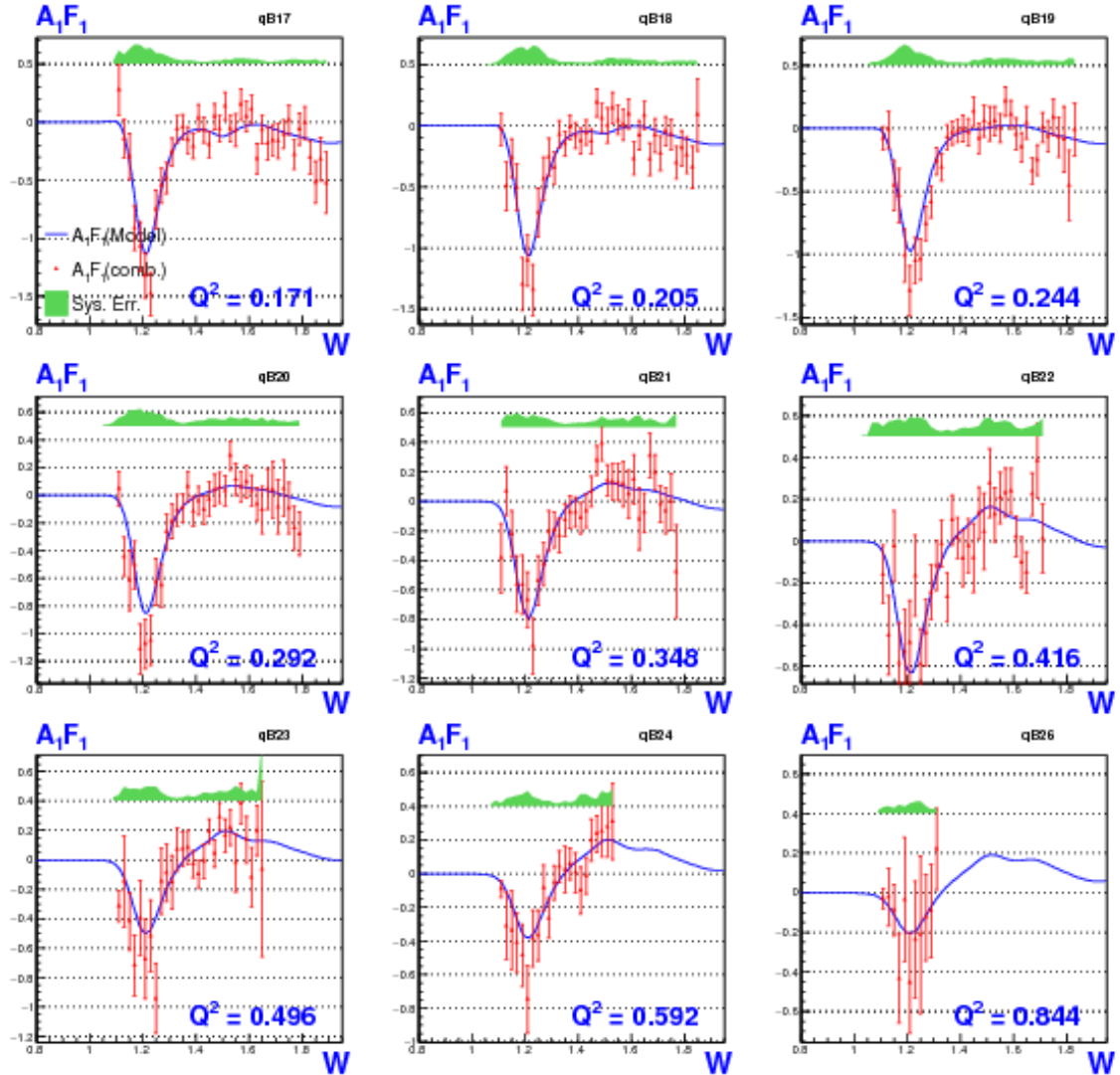


FIG. 6.8. Similar plots as in Fig. 6.7 showing the combined results on g_1 in the next 9 Q^2 bins.

1687 6.2 Moments of Deuteron Spin Structure functions

1688 Using the measured values of g_1 and A_1F_1 , three integrals were evaluated for each of
 1689 the Q^2 bins in which these data were measured. These integrals have been calculated
 1690 in two ways - using only the new EG4 measurements, and adding model contributions
 1691 to the data for regions not covered by our measurements. The integrals with the model
 1692 contributions were calculated from $x = 0.001$ to the onset of the resonance region (i.e.

1693 to the pion production threshold of $W \approx 1.08$ GeV), dividing the sum into three parts
 1694 for each Q^2 bin. For example, Γ_1 was evaluated by adding up the product $g_1\Delta x$ over
 1695 the following three kinematic regions:

$$\Gamma_1(Q^2) = \int_{x=0.001}^{x(W_{data})} g_1(x, Q^2) dx \quad \text{model} \quad (6.1)$$

$$+ \int_{x(W_{data})}^{W=1.15} g_1(x, Q^2) dx \quad \text{data (or model for gaps)} \quad (6.2)$$

$$+ \int_{W=1.15}^{W=1.08} g_1(x, Q^2) dx \quad \text{model} \quad (6.3)$$

1696 where W_{data} indicates the upper edge of the last W bin in which the EG4 data is
 1697 available in a given Q^2 bin (the W variable was divided into 70 bins of size 20 MeV
 1698 in the range $W=(0.7,2.1)$ GeV). The first part of the integral as given by Eq. 6.1 is
 1699 evaluated by using the model values of g_1 and using Δx corresponding to a W bin
 1700 of size 10.0 MeV. The ΔW is converted to Δx by using $x = Q^2/(Q^2 + W^2 - M^2)$ to
 1701 evaluate x at the two edges of each W bin and taking the difference as follows:

$$\Delta x = x_{High} - x_{Low} = \frac{Q^2}{Q^2 + W_{High}^2 - M^2} - \frac{Q^2}{Q^2 + W_{Low}^2 - M^2} \quad (6.4)$$

1702 The second part given by Eq. 6.2 is evaluated similarly but using the EG4 results for
 1703 g_1 if there is no measurement gap in between. If there is any gap, the same method
 1704 as in the first part is used to get a model contribution for the gap and added to the
 1705 data contribution. Lastly, the the third contribution given by Eq. 6.2 again were
 1706 evaluated from from model values (quasi-elastic part turned off from the model in all
 1707 of these cases) but with finer W bins (1 MeV) because the integrals are very sensitive
 1708 to the region near the Δ resonance due to the fact that the structure functions show
 1709 rapid changes in this region. The reason to calculate the third integral using model
 1710 values rather than data values is to avoid having contributions in the integrals from
 1711 the quasi-elastic contamination.

1712 The statistical errors are evaluated by adding the statistical error contribution
 1713 in each W or x bin in quadrature. For example, if the integral is evaluated in a
 1714 Q^2 bin by calculating the sum $\left(\sum_{W \text{ bins}} g_1 \cdot \Delta x \right)$, then the corresponding statistical
 1715 error is evaluated by calculating $\sqrt{\sum_{W \text{ bins}} (\sigma g_1)^2 \cdot \Delta x}$. Because the model contribution
 1716 is assumed to have no statistical uncertainties, the statistical errors in the integrals
 1717 come solely from the propagation of the statistical error of the measured g_1 or $A_1 F_1$.

1718 The other two integrals and their errors are evaluated in the same manner, with
 1719 g_1 replaced by their corresponding integrands and again calculating the three parts
 1720 of the integrals separately.

1721 These integrals are then compared with the latest available predictions from dif-
1722 ferent theories (mainly χ PT) and phenomenological calculations along with EG1b or
1723 DIS data whenever applicable.

1724 **6.2.1 First moment of g_1 (Γ_1)**

1725 The first integral of interest is the first moment of g_1 i.e., Γ_1 (see Eq. 1.10) , which
1726 was calculated for all Q^2 bins for which the new data are available. Figures 6.9 and
1727 6.10 show the two calculations (with and without model input) along with EG1b
1728 data and several χ PT and model predictions. One important observation here is that
1729 our measurements provide the only data points in the very low Q^2 region (i.e for
1730 $Q^2 < 0.05 \text{ GeV}^2$) where χ PT is thought to be able to make rigorous calculations.
1731 Therefore, our data will provide important benchmarks for the future calculations in
1732 this kinematics. Particularly, the latest χ PT prediction by Bernard *et al.* [50] seems
1733 to agree remarkably well with data in the very low Q^2 region.

1734 While all other higher Q^2 predictions, except that of Ji *et al.*, seem to be within
1735 the uncertainties of our measurements, it can be seen that the phenomenological
1736 predictions of Soffer *et al.* compare slightly better with data than others (excluding,
1737 of course, the Bernard *et al.* prediction).

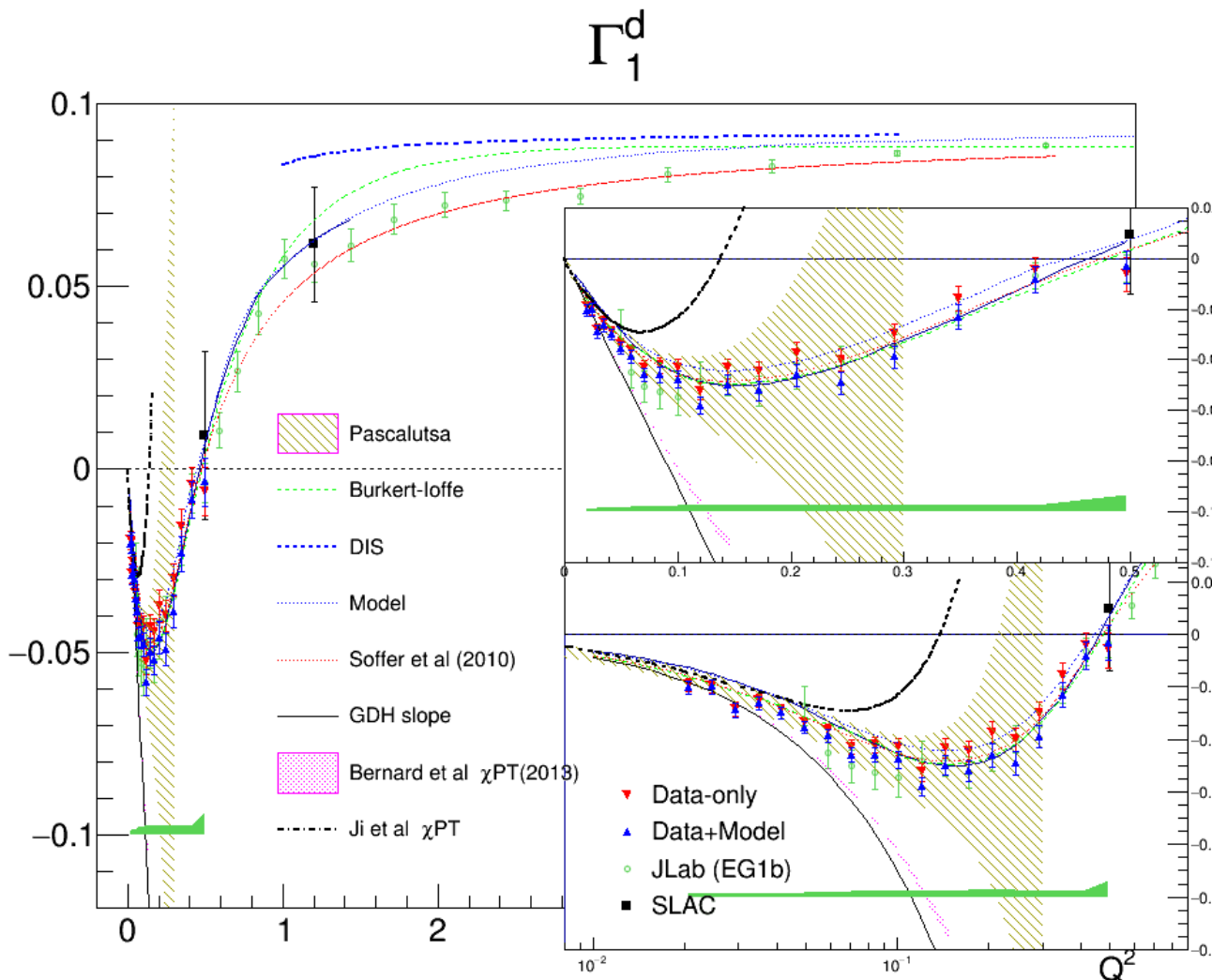


FIG. 6.9. Extracted Γ_1^d for deuteron compared with some of the past measurements and various theoretical predictions with a linear scale used for Q^2 .

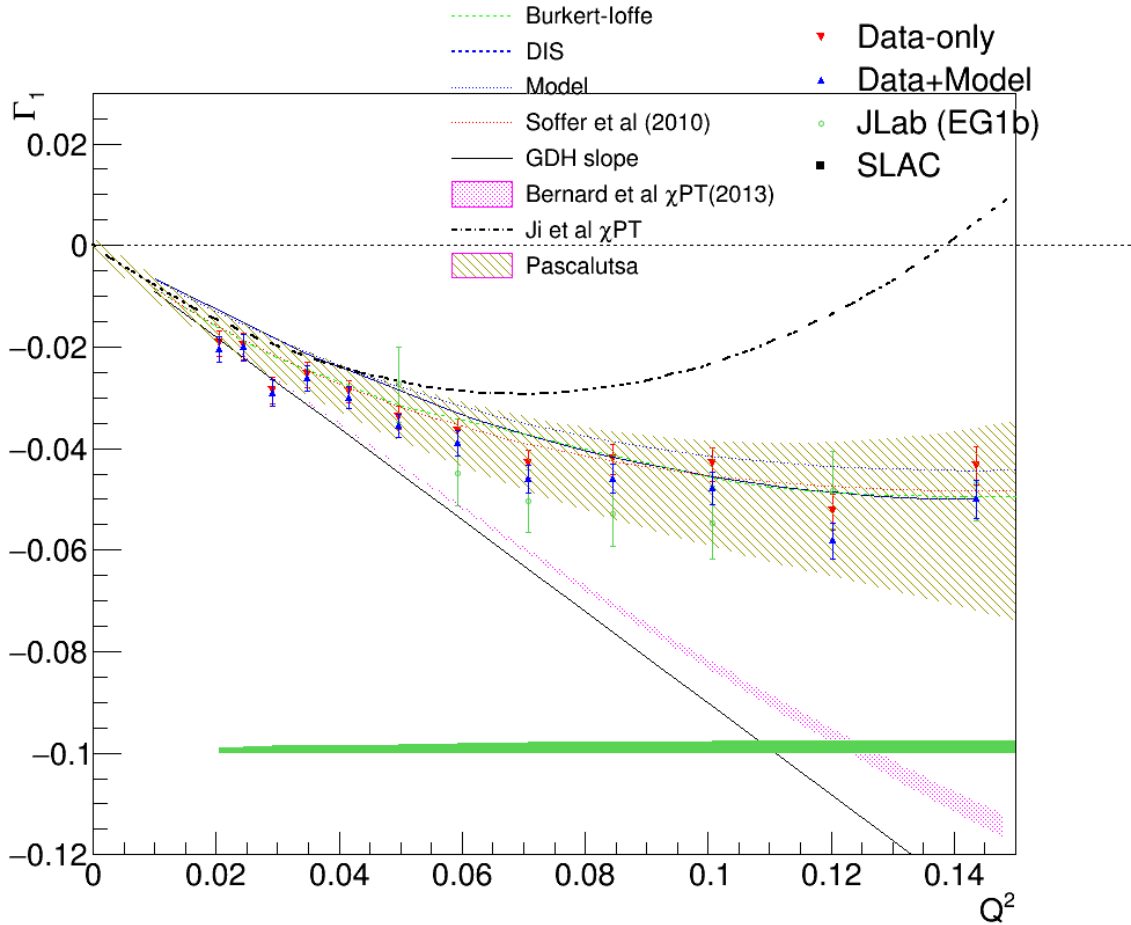


FIG. 6.10. Extracted Γ_1 for deuteron compared with some of the past measurements and various theoretical predictions zooming in on the very low Q^2 region.

1738 6.2.2 The extended GDH integral \bar{I}_{TT}

1739 Using the measured values of $A_1 F_1$, the generalized GDH integral $\bar{I}_{TT} = 2M^2/Q^2 \int A_1 F_1(x, Q^2) dx$
 1740 was also calculated and compared (see Figs. 6.11 and 6.12) with the latest χ PT cal-
 1741 culation from Bernard *et al.* [50]. We can see that at the very low Q^2 , the χ PT
 1742 prediction and the measurement get very close. The χ PT methods determine the
 1743 higher powers of Q^2 in the Taylor expansion of the integral around the photon point
 1744 $Q^2 = 0$, beyond the prediction of the GDH sum rule which determines the lowest or-
 1745 der term. Our data seem indeed to converge towards the GDH sum rule at our lowest
 1746 Q^2 . However, only one or two higher order terms can be calculated confidently, since
 1747 higher orders require additional (unknown) constants. Therefore, χ PT predictions

₁₇₄₈ do reasonably well at ultra-low Q^2 but cannot be expected to work at the higher Q^2 ,
₁₇₄₉ where the data show a turn-around and a transition towards positive values.

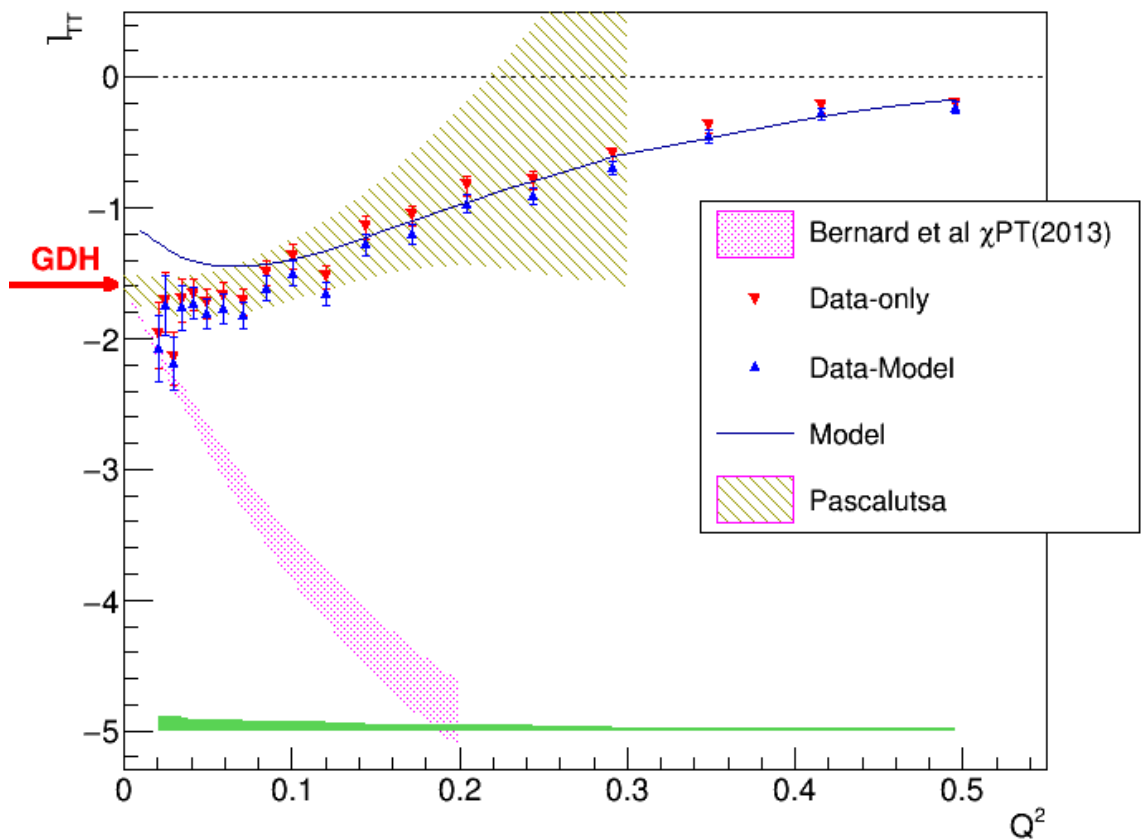


FIG. 6.11. Extracted \bar{I}_{tt} for deuteron compared with the used model and a χ PT prediction with a linear scale used for Q^2 .

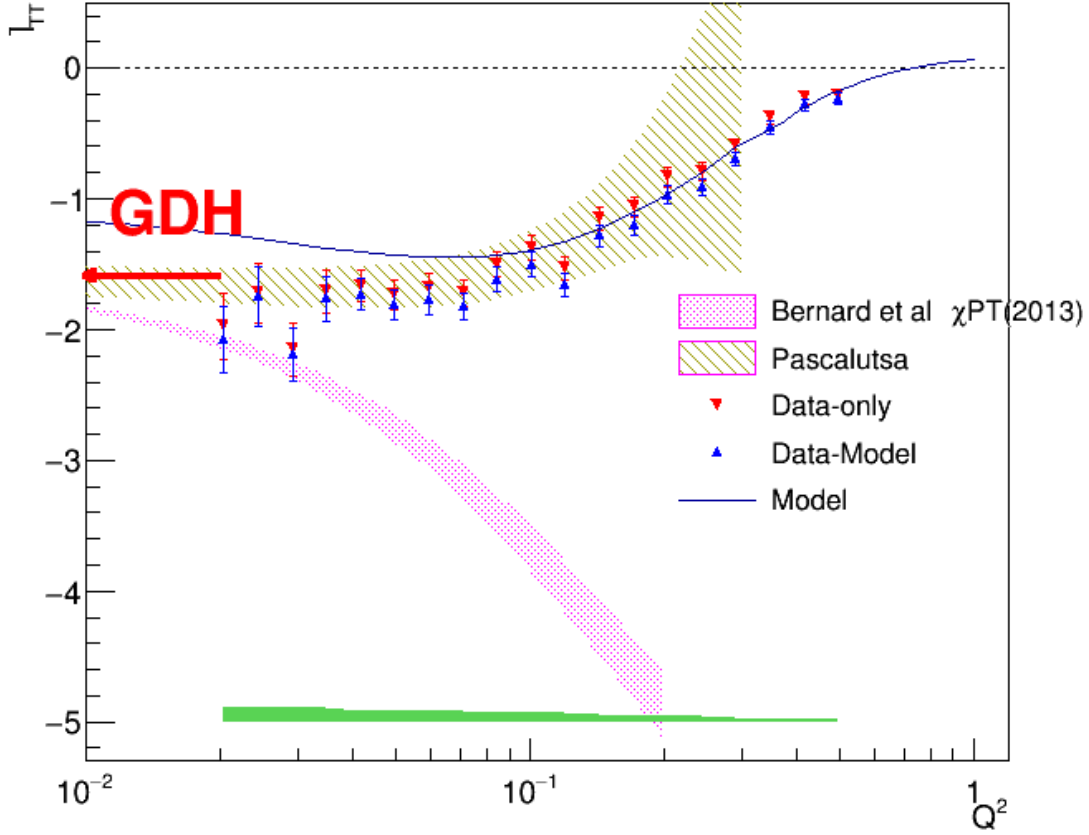


FIG. 6.12. Extracted I_{tt} for deuteron compared with the model used in the simulation and two χ PT predictions with a logarithmic scale used for Q^2 .

1750 6.2.3 The Generalized Forward Spin Polarizability γ_0

1751 Finally, the generalized forward polarizability (as given by Eq. 1.16) for the deuteron
 1752 was also calculated using the measured values of $A_1 F_1$ and then compared with various
 1753 predictions as shown in Figs. 6.13 and 6.14. The comparison shows that both χ PT
 1754 calculations by Bernard *et al.* and Kao *et al.* converge with data at the lowest Q^2
 1755 bins. However, the χ PT calculations by Pascalutsa *et al.* seem to deviate greatly from
 1756 both the current measurement as well as the other χ PT calculations (particularly at
 1757 the very low Q^2 region, indicating that some ingredients might be missing from the
 1758 calculation model. Likewise, the MAID prediction also seems to be somewhat off the
 1759 current results.

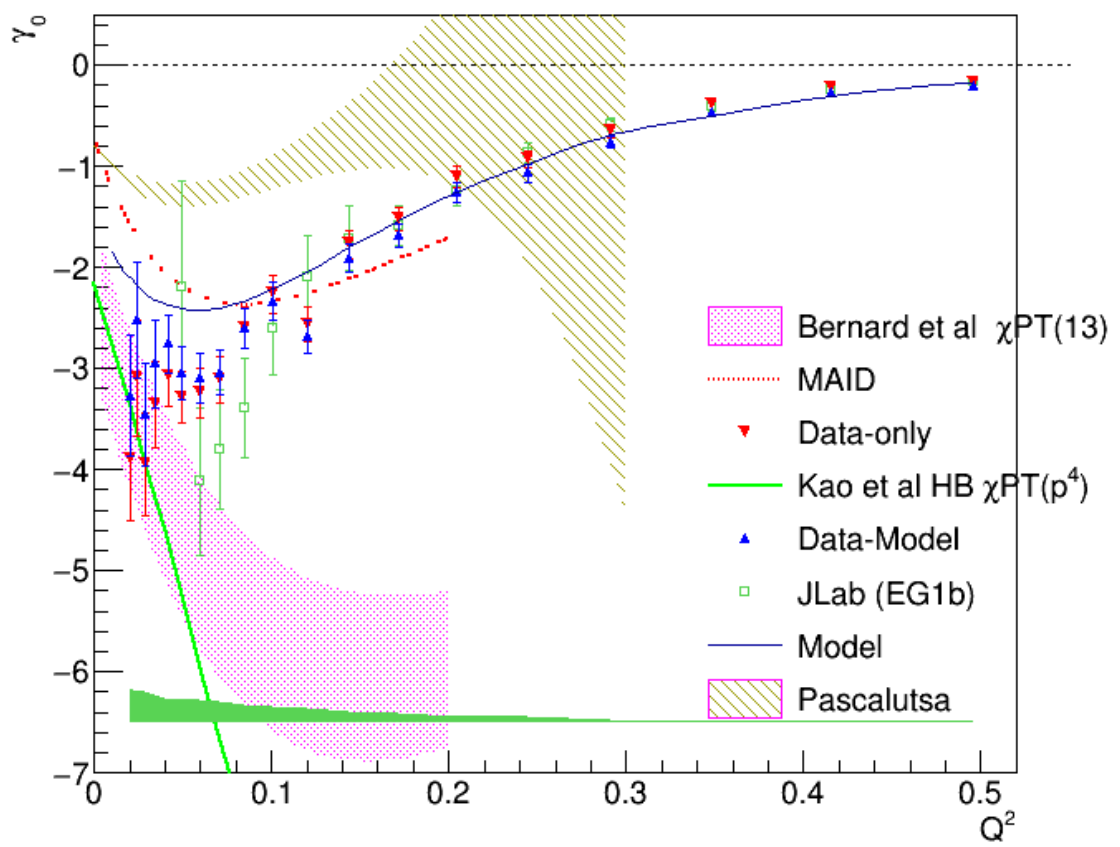


FIG. 6.13. Extracted γ_0 for deuteron compared with some of the past measurements and various theoretical predictions with a linear scale used for Q^2 .

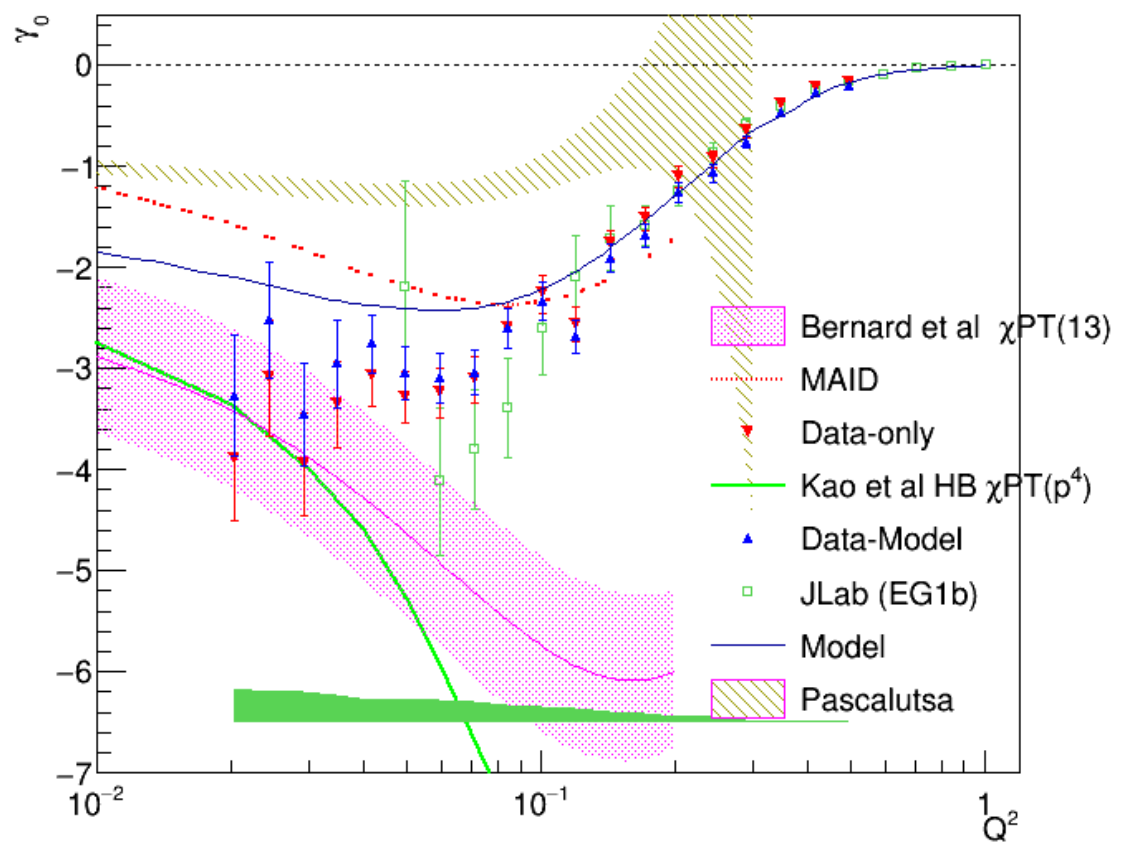


FIG. 6.14. Extracted γ_0 for deuteron compared with some of the past measurements and various theoretical predictions with a logarithmic scale used for Q^2 .

¹⁷⁶⁰ **Chapter 7**

¹⁷⁶¹ **Conclusions**

¹⁷⁶²

¹⁷⁶³ The very low momentum transfer (Q^2) data from the EG4 experiment have been
¹⁷⁶⁴ analyzed for the helicity dependent inclusive cross section (difference) for the scattering
¹⁷⁶⁵ of longitudinally polarized electrons off longitudinally polarized deuterons (from
¹⁷⁶⁶ DNP polarized ND₃ target, using two beam energies 1.3 and 2.0 GeV). The ana-
¹⁷⁶⁷ lyzed data has the kinematic coverage of ($0.02 \text{ GeV}^2 < Q^2 < 0.7 \text{ GeV}^2$) and (1.08
¹⁷⁶⁸ $\text{GeV} < W < 2.0 \text{ GeV}$). Although past measurements from EG1b go as low as 0.05
¹⁷⁶⁹ GeV^2 in Q^2 , the new measurements have higher precision (due to higher statistics
¹⁷⁷⁰ and better detection efficiency) in the overlapping region (particularly evident below
¹⁷⁷¹ $Q^2 = 0.2 \text{ GeV}^2$) in addition to new high precision data in the previously unmeasured
¹⁷⁷² region below $Q^2 = 0.5 \text{ GeV}^2$.

¹⁷⁷³ The new deuteron data were used to extract the deuteron's spin structure function
¹⁷⁷⁴ g_1 by comparing the experimental data with simulated data produced by using a
¹⁷⁷⁵ realistic cross section model for the deuteron under similar kinematic conditions.
¹⁷⁷⁶ The newly extracted data pushes the lower limit on Q^2 in the resonance region with
¹⁷⁷⁷ reduced systematic and statistical uncertainties that will contribute greatly to the
¹⁷⁷⁸ world data set. It is observed that the data from two beam energies give results
¹⁷⁷⁹ that are in good agreement wherever they overlap. The low Q^2 results clearly show
¹⁷⁸⁰ resonance structure in the region $W \leq 2.0$ which smooths out as Q^2 becomes larger.
¹⁷⁸¹ In particular, the Δ -resonance shows a strongly and consistently negative signal at
¹⁷⁸² all Q^2 , but the second resonance region (around $W=1.5 \text{ GeV}$) shows a rather rapid
¹⁷⁸³ transition of g_1 (or polarized cross section) from strongly negative values at low Q^2
¹⁷⁸⁴ to clearly positive values at high Q^2 . This observation in the second resonance region
¹⁷⁸⁵ is not well described by the model because the model is not constrained in the region
¹⁷⁸⁶ due to the lack of experimental data up to now and indicates that the spin-flip helicity
¹⁷⁸⁷ amplitude $A_{\frac{3}{2}}^T$ dominates the cross section at low Q^2 while the non-flip amplitude $A_{\frac{1}{2}}^T$
¹⁷⁸⁸ becomes stronger at higher Q^2 .

1789 The product $A_1 F_1$ of the virtual photon asymmetry A_1 and the unpolarized struc-
1790 ture function F_1 was also extracted from the same data and method. The extracted
1791 results on g_1 and $A_1 F_1$ were then used to evaluate three important moments - the
1792 first moment Γ_1^d of g_1 , the generalized GDH integral \bar{I}_{TT}^d and the generalized forward
1793 spin polarizability γ_0^d - in each of the Q^2 bins in which the new g_1 and $A_1 F_1$ have
1794 been extracted. The new low Q^2 measurements of the moments evaluated both with
1795 and without model inputs for the unmeasured kinematic regions were then compared
1796 with various χ PT calculations, phenomenological predictions and past measurements,
1797 particularly the EG1b or DIS data whenever applicable.

1798 The EG4 results provide the only data points in the very low Q^2 region ($Q^2 < 0.05$
1799 GeV^2) where χ PT is thought to be able to make rigorous calculations. The high
1800 precision data will provide important benchmarks for the future calculations in this
1801 kinematics. In the case of the first moment Γ_1^d , the EG4 results show remarkable
1802 agreement with the latest χ PT prediction by Bernard *et al.* [50] in the very low Q^2
1803 region. The phenomenological predictions which have much larger Q^2 coverage also
1804 seem to agree within the uncertainties of our measurements, with the predictions of
1805 Soffer *et al.* showing slightly better comparison than others. Likewise, the very low Q^2
1806 results of the generalized GDH integral \bar{I}_{TT} are indeed observed to converge towards
1807 the GDH sum rule and thus getting very close to the χ PT predictions by Bernard *et al.*
1808 [50]. Finally, the generalized forward polarizability (γ_0^d) for the deuteron calculated
1809 from the EG4 data and the χ PT calculations by Bernard *et al.* and Kao *et al.* seem to
1810 converge at the lowest Q^2 bins. However, the χ PT based predictions from Pascalutsa
1811 *et al.* and the MAID prediction seems to be well off the current results for all three
1812 moments.

1813 The deuteron data in combination with the EG4 proton data taken under sim-
1814 ilar conditions (currently being analyzed by another collaborator) will be useful in
1815 extracting neutron quantities in the near future, which is valuable because of the un-
1816 availability of free neutron targets. Moreover, due to the complexities of the nuclear
1817 medium effects, neutron data from deuteron will be very important to enhance con-
1818 fidence in similar neutron results extracted from other nuclear targets - particularly
1819 ${}^3\text{He}$.

1820 The work presented in this analysis has improved our understanding of the field
1821 of the nucleon spin structure and contributed to more solid foundation for future
1822 advancements. The new data on spin structure functions and their moments will
1823 help various χ PT calculations and phenomenological models such as MAID to better
1824 constrain their parameters enabling them to make better predictions in the future.
1825 With the availability of the high precision data in the previously (largely) unmeasured
1826 region that has the potential to help constrain the theories and models, it is hoped
1827 that a unified description of spin structure functions over all kinematic regions will
1828 be possible in the future.

₁₈₂₉ **Bibliography**

- ₁₈₃₀ [1] K.V. Dharmawardane et al. Measurement of the x- and -dependence of the
₁₈₃₁ asymmetry on the nucleon. *Physics Letters B*, 641(1):11 – 17, 2006.
- ₁₈₃₂ [2] J. Ashman and other. A measurement of the spin asymmetry and determination
₁₈₃₃ of the structure function g1 in deep inelastic muon-proton scattering. *Physics*
₁₈₃₄ *Letters B*, 206(2):364 – 370, 1988.
- ₁₈₃₅ [3] D.J. Gross and F. Wilczek. Ultraviolet behavior of non-abelian gauge theories.
₁₈₃₆ *Phys. Rev. Lett.*, 30(26):1343–1346, 1973.
- ₁₈₃₇ [4] Kenneth G. Wilson. Confinement of quarks. *Phys. Rev. D*, 10:2445–2459, Oct
₁₈₃₈ 1974.
- ₁₈₃₉ [5] J. P. Chen and others. The GDH Sum Rule and the Spin Structure of ^3He and
₁₈₄₀ the Neutron using Nearly-Real Photons. JLab Hall A Proposal, 1997. PR97-110.
- ₁₈₄₁ [6] S. B. Gerasimov. *Yad. Fiz.*; 2:598, 1966.
- ₁₈₄₂ [7] S. D. Drell and A. C. Hearn. Exact sum rule for nucleon magnetic moments.
₁₈₄₃ *Phys. Rev. Lett.*, 16:908–911, May 1966.
- ₁₈₄₄ [8] S.E. Kuhn, J.-P. Chen, and E. Leader. Spin Structure of the Nucleon - Status
₁₈₄₅ and Recent Results. *Prog.Part.Nucl.Phys.*, 63:1–50, 2009.
- ₁₈₄₆ [9] H. Dutz et al. First measurement of the gerasimov-drell-hearn sum rule for ^1H
₁₈₄₇ from 0.7 to 1.8 gev at elsa. *Phys. Rev. Lett.*, 91:192001, Nov 2003.
- ₁₈₄₈ [10] H. Dutz et al. Measurement of helicity-dependent photoabsorption cross sections
₁₈₄₉ on the neutron from 815 to 1825 mev. *Phys. Rev. Lett.*, 94:162001, Apr 2005.
- ₁₈₅₀ [11] Dieter Drechsel and Lothar Tiator. The Gerasimov-Drell-Hearn sum rule and
₁₈₅₁ the spin structure of the nucleon. *Ann.Rev.Nucl.Part.Sci.*, 54:69–114, 2004.
- ₁₈₅₂ [12] S. Hoblit et al. Measurements of $hd(\gamma, \pi)$ and implications for the convergence
₁₈₅₃ of the gerasimov-drell-hern integral. *Phys. Rev. Lett.*, 102:172002, Apr 2009.

- 1854 [13] M. Anselmino, B.L. Ioffe, and E. Leader. On Possible Resolutions of the Spin
1855 Crisis in the Parton Model. *Sov.J.Nucl.Phys.*, 49:136, 1989.
- 1856 [14] A. Deur et al. Measurement of the Gerasimov-Drell-Hearn Integral at low Q^2 on
1857 the Neutron and Deuteron. CLAS Proposal, December 2006. PR06-017.
- 1858 [15] Matthias Burkardt. The $g(2)$ Structure Function. *AIP Conf. Proc.*, 1155:26–34,
1859 2009.
- 1860 [16] M. Anghinolfi and others. The GDH Sum Rule with Nearly-Real Photons and
1861 the Proton g_1 Structure Function at Low Momentum Transfer. CLAS Proposal,
1862 2003. PR03-006.
- 1863 [17] D. Drechsel, B. Pasquini, and M. Vanderhaeghen. Dispersion relations in real
1864 and virtual Compton scattering. *Phys. Rept.*, 378:99–205, 2003.
- 1865 [18] N. Guler et al. Precise determination of the deuteron spin structure at low to
1866 moderate Q^2 with clas and extraction of the neutron contribution. *Phys. Rev.*
1867 *C*, 92:055201, Nov 2015.
- 1868 [19] The eg4 wiki. https://clasweb.jlab.org/rungroups/eg4/wiki/index.php/Main_Page. [Online; accessed 22-Sep-2013].
- 1870 [20] X. Zheng. CLAS EG4 Analysis Note - 'Double- and Target Spin Asymmetries
1871 in Pion Electro-production from Polarized NH₃ Targets'. 2015.
- 1872 [21] X. Zheng et al. Measurement of target and double-spin asymmetries for the
1873 $\vec{e}\vec{p} \rightarrow \vec{e}\vec{\pi}^+(n)$ reaction in the nucleon resonance region at low Q^2 . *Phys. Rev. C*,
1874 94:045206, Oct 2016.
- 1875 [22] N. Guler. *Spin Structure of the Deuteron*. PhD thesis, Old Dominion University,
1876 December 2009.
- 1877 [23] M. Osipenko, A. Vlassov and M. Taiuti. A vxibus based trigger for the clas
1878 detector at cebaf. Technical Report CLAS NOTE 2004-020, JLAB, 2004.
- 1879 [24] K.S. Egiyan. Determination of electron energy cut due to the clas ec threshold.
1880 Technical Report CLAS-NOTE-1999-007, JLAB, 1999.
- 1881 [25] The eg4 collaboration. <http://clasweb.jlab.org/shift/eg4/>. [Online; ac-
1882 cessed 22-Sep-2013].
- 1883 [26] S. E. Kuhn. Private communications, 2013.

- 1884 [27] P. Bosted. Private communications, 2010.
- 1885 [28] Beam energies during the eg4 run. http://www.jlab.org/deurpam/e03006/eg4_energy.pdf. [Online; accessed 05-Jan-2017].
- 1887 [29] P. Bosted. CLAS EG1-DVCS Technical Note 004 - 'Tracking from Drift Chambers to Target through Solenoid'. 2010.
- 1889 [30] P. Bosted and A. Kim. CLAS EG1-DVCS Technical Note 002 - 'Beam (x,y) and Target Center z from Raster ADCs'. 2014.
- 1891 [31] A. Klimenko and S. Kuhn . Momentum Corrections for E6. Technical Report CLAS-Note 2003-005, JLAB, 2003.
- 1893 [32] William R Leo. *Techniques for nuclear and particle physics experiments: a how-to approach*. Springer, 1994.
- 1895 [33] R. G. Fersch. PhD thesis, January.
- 1896 [34] P. Bosted. Pair-symmetric and pion backgrounds for eg1b. Technical Report CLAS-NOTE-2004-005, JLAB, 2004.
- 1898 [35] S. P. Phillips. http://clasweb.jlab.org/rungroups/eg4/wiki/index.php/October_14%2C_2011. [Online; accessed 22-Sep-2013].
- 1900 [36] Peter Bosted. Nh3 correction for nd3 target: Eg1-dvcs technical note 17. Technical report, November 2011.
- 1902 [37] Suman Koirala. EG1-DVCS Part-C Target Contamination. Technical report, May 2012.
- 1904 [38] S.E. Kuhn and K. Adhikari. Data Analysis for EG4 - extraction of g_1 from data. 2013.
- 1906 [39] K. Abe et al. Measurements of the proton and deuteron spin structure functions g_1 and g_2 . *Phys. Rev. D*, 58:112003, Oct 1998.
- 1908 [40] T.V. Kuchto and N.M. Shumeiko. Radiative effects in deep inelastic scattering of polarized leptons by polarized nucleons. *Nuclear Physics B*, 219(2):412–436, 1983.
- 1911 [41] L. W. Mo and Y. S. Tsai. Radiative corrections to elastic and inelastic ep and up scattering. *Rev. Mod. Phys.*, 41:205–235, Jan 1969.

- 1913 [42] P.E. Bosted and M.E. Christy. Empirical fit to inelastic electron-deuteron
1914 and electron-neutron resonance region transverse cross-sections. *Phys. Rev.*,
1915 C77:065206, 2008.
- 1916 [43] R. G. Fersch et al. Precise Determination of Proton Spin Structure Functions at
1917 Low to Moderate Q^2 with CLAS. To be published, October 2012.
- 1918 [44] N. Guler et al. Precise Determination of Deuteron and Neutron Spin Structure
1919 Functions at Low to Moderate Q^2 with CLAS. To be published, October 2013.
- 1920 [45] Yonatan Kahn, W. Melnitchouk, and Sergey A. Kulagin. New method for ex-
1921 tracting neutron structure functions from nuclear data. *Phys. Rev.*, C79:035205,
1922 2009.
- 1923 [46] M. Holtrop. GSIM: CLAS GEANT Simulation. http://nuclear.unh.edu/~maurik/gsim_info.shtml. [Online; accessed 22-Sep-2013].
- 1925 [47] Brooks, W. *CLAS - A large acceptance spectrometer for intermediate energy*
1926 *electromagnetic nuclear physics*. Jun 1999.
- 1927 [48] B. Dey. *Differential cross section and polarization extractions for $\gamma p \rightarrow K^+ \Sigma^0$*
1928 *and $\gamma p \rightarrow \phi p$ using CLAS at Jefferson Lab, towards a partial wave analysis in*
1929 *search of missing baryon resonances*. PhD thesis, Carnegie Mellon University,
1930 July 2011.
- 1931 [49] J. Zhang. *Exclusive π^- Electro-production from the Neutron in the Resonance*
1932 *Region*. PhD thesis, Old Dominion University, May 2010.
- 1933 [50] Veronique Bernard, Evgeny Epelbaum, Hermann Krebs, and Ulf-G. Meissner.
1934 New insights into the spin structure of the nucleon. *Phys. Rev.*, D87:054032,
1935 2013.

¹⁹³⁶ **Appendix A**

¹⁹³⁷ **FFREAD cards used by GSIM**

Table A.1: Some of the ffread cards & their values which are used as GSIM input parameters.

Cards	Values
MAGTYPE	2
MAGSCALE	-0.5829 0.0 (for 1.337 GeV)
MAGSCALE	-0.3886 0.0 (for 1.993 GeV)
GEOM	'ALL'
NOMC	'EC' 'SC' 'CC' 'DC'
NOGEOM	'MINI' 'ST' 'TG2' 'TG' 'SOL'
NOGEOM	'PTG' 'FOIL'
NOMATE	'PTG' 'FOIL'
PTGIFIELD	1
TMGIFIELD	1
TMGIFIELDM	1
TMGFIELDM	51.0
TMGSCALE	0.979
PTGMAXRAD	300.0
MGPOS	0.0 0.0 -100.93
BAFF	3. 9. 165.3 9. 180.5 9. 195.8
RUNG	50556
AUTO	1
KINE	1